OPTICAL FREQUENCY COMB GENERATION IN COUPLED NONLINEAR MICROCAVITIES

CHENG ZIHAO

PhD

The Hong Kong Polytechnic University

2022

The Hong Kong Polytechnic University

Department of Electronic and Information Engineering

Optical Frequency Comb Generation in Coupled Nonlinear Microcavities

CHENG ZIHAO

A thesis submitted in partial fulfillment of the requirements for the degree of Doctor of Philosophy

August 2022

CERTIFICATE OF ORIGINALITY

I hereby declare that this thesis is my own work and that, to the best of my knowledge and belief, it reproduces no material previously published or written, nor material that has been accepted for the award of any other degree or diploma, except where due acknowledgement has been made in the text.

_____(Signed)

_____CHENG Zihao_____(Name of student)

Abstract

Microcavity based optical frequency combs with Kerr nonlinearity attract much attentions for their various applications and compact configurations for chip-scale integration. Kerr soliton combs are typically generated in nonlinear microcavities with anomalous dispersion pumped by red-detuned continuous wave lasers. Although soliton combs have been repeatedly demonstrated in the laboratories, there are several challenges limit the use of microcavity combs beyond the laboratories.

The first challenge is that current soliton Kerr comb generation scheme requires tunable lasers for the access of the soliton states. Tunable lasers are usually large scale and high-power consumption making them unsuitable for chip-scale integration. The second challenge is that soliton Kerr combs can only be generated in ultralow loss microcavities. The low loss requirement limits the choice of cavity materials and size. The cost of fabricating low loss cavities also limits commercial applications of microcavity combs.

In this thesis, we propose optical frequency comb generation by utilizing coupled nonlinear microcavities to overcome these challenges. By theoretical analysis, we find that the coupled microcavities support modulation instability generation in the blue-detuned side of the nonlinear cavity's resonance, whereas there is no blue-detuned modulation instability generation in a single nonlinear microcavity. The size and location of the blue-detuned modulation instability region can be varied by tuning the

coupling coefficient between the two cavities, the loss of the auxiliary cavity or detuning between the two cavities. By using the blue-detuned modulation instability, we propose a soliton comb generation scheme by tuning the coupling coefficient in a coupled microcavity system instead of tuning the wavelength of the pump laser. We find that the soliton generation region (bistability region) depends on the coupling coefficient between the coupled cavities. We showed that the auxiliary microcavity introduces a new optical path which makes “blue-detuned” soliton comb generation possible. We numerically demonstrate soliton comb generation by tuning the coupling coefficient and design a Sagnac loop like structure to show that the same phenomenon is applicable for the coupling between the clockwise and counterclockwise propagation modes in a single microcavity. We further show that if the auxiliary cavity provides gain, then it is possible to generate soliton combs in the main cavity with higher loss, which will reduce the difficulties in fabricating low loss microcavities and expand the choices of cavity materials.

Our study in this thesis provides a theoretical understanding and experimental guidance for optical frequency comb generation in coupled nonlinear microcavities. The results will benefit the development of chip-scale comb sources.

Acknowledgement

I would like to express my gratitude to many people during my Ph.D. studies. First of all, I want to give my sincere appreciation to my supervisor, Prof. P. K. A. Wai. His patient guidance and intuition pointed the way for my research. Despite his busy schedule, he was always eager to discuss with me about my research and the latest results.

I thank Dr. Li Feng and Dr. Huang Dongmei for their generous help and support. The fruitful discussion with Dr. Li Feng gave me a deep understanding of many theoretical issues. I was fortunate to benefit from Dr. Huang Dongmei's expertise and experimental skills. My experimental skills in optics started with her.

I would like to thank Prof. Lu Chao for his kind and continued help. I am also thankful to members in Prof. Wai's research group, Dr. Kang Zhe, Dr. Zhang Xianting, Dr. Xu Yin, Dr. Li Yujia, and Mr. Chen Hongjie. We had many valuable discussions and came up with many new ideas. Special thanks go to members of the Photonic Research Center and Shenzhen base. We took part in many interesting activities and spent good times together.

Last but not the least, I want to thank my parents and my wife. Their love and supports always keep me moving forward.

June, 2022, Cheng Zihao

Statement of Originality

The following contributions reported in this thesis are claimed to be original.

1. I used coupled mode equations to analyze the modulation instability generation condition in coupled microcavities and discovered a blue-detuned modulation instability region.
2. Based on modified Ikeda map, I determined the bistability region in coupled nonlinear microcavities. The bistability region influenced by the coupling coefficient between two identical cavities is discussed.
3. I showed that the blue-detuned modulation instability is due to the new optical path introduced by the auxiliary microcavity.
4. I presented that the blue-detuned modulation instability region can be analytically determined with the assumption of the auxiliary cavity in steady state first.
5. I demonstrated a new soliton frequency comb generation scheme by tuning the coupling coefficient in a coupled nonlinear microcavity system.
6. I designed a Sagnac loop structure to achieve soliton frequency comb generation by tuning the coupling coefficient between clockwise and counterclockwise propagation modes.
7. I proposed a novel method of soliton frequency comb generation in low Q microcavities by coupling an auxiliary cavity with gain.

Publications Arising from the Thesis

Journals:

1. **Cheng, Z.**, Huang, D., Li, F., Lu, C., & Wai, P. K. A., “Modulation instability generation with blue-detuned pump laser in coupled microcavities,” JOSA B, 39(6), 1655-1665 (2022).
2. **Cheng, Z.**, Huang, D., Li, F., Lu, C., & Wai, P. K. A., “Kerr soliton frequency comb generation by tuning the coupling coefficient in coupled nonlinear microcavities,” in preparation.

Conference papers:

1. **Cheng, Z.**, Huang, D., Li, F., Lu, C., & Wai, P. K. A, “Dual-comb generation in coupled nonlinear microcavities by tuning the coupling,” In CLEO: QELS_Fundamental Science (pp. FW1B-7) (2022, May).
2. **Cheng, Z.**, Huang, D., Li, F., Lu, C., & Wai, P. K. A, “Optical Frequency Comb Generation in Normal Dispersion Microresonators with Coupled-ring Structure,” In Optoelectronics and Communications Conference (pp. T4E-3) (2021, July).

Content

1 Background

1.1 Optical frequency combs

1.1.1 Concept and principle of optical frequency combs

Optical frequency combs (OFCs) are initially developed to count the cycles of optical atomic clocks [1]. Before the OFCs, it takes up to 10 scientists, 20 different oscillators and 50 feedback loops to carry out a single optical measurement [2]. The generation of OFCs in a phase-stabilized mode locked laser (MLL) in 2000 replaced such a complex system [1]. MLLs have a broadband spectrum over 100 nm and consist of hundreds of thousands to millions of coherent resonant longitudinal optical cavity modes. The pulse spectrum has two unique properties for high precision frequency metrology: all the optical cavity modes are perfectly equidistant in the frequency domain and all the optical modes are phase coherent. The properties lead to deterministic evolution of frequency and phase of every cavity mode in the OFC spectrum. As a result, the absolute frequencies of every mode in the OFC spectrum are determined once the absolute frequency of any one cavity mode is known.

The equal frequency spacing of the modes in the spectrum is analogous to a comb. The optical fields of OFCs can be described by comb like periodic longitudinal cavity modes in the frequency domain. The frequencies of the cavity modes are equally separated by an identical mode spacing f_r, which is equal to the repetition rate of the

temporal pulse train. However, the frequencies of the cavity modes are not necessarily exact multiples of f_r. The exact frequencies of the N-th mode ν_N can be described by the summation of N times f_r and a common offset frequency f_0 ($f_0 < f_r$) as

$$\nu_N = N \times f_r + f_0 . \tag{1.1}$$

Figure 1.1 depicts a frequency comb. From Eq. (1.1), even if there are millions of modes in an OFC spectrum, there are only two degrees of freedom: the repetition rate f_r and offset frequency f_0.

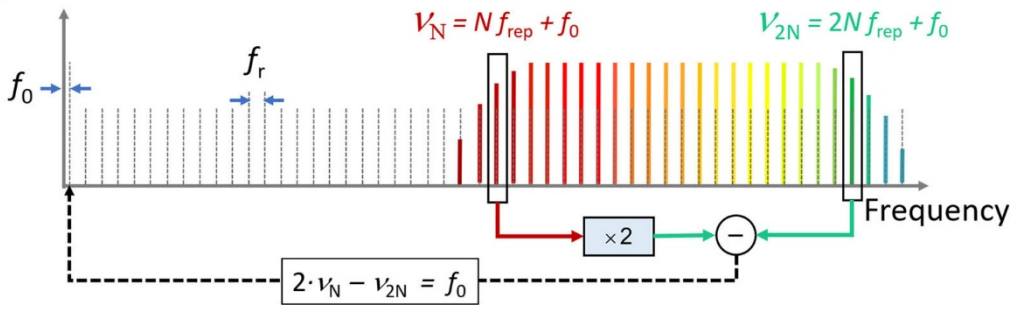

Fig. 1.1 Visualization of the comb equation and offset frequency detection with self-referencing [1]. (f_0: offset frequency; f_r: repetition rate; ν_N: frequency of the N-th mode).

The laser repetition rate f_r is the inverse of the period T_R of the pulse train with $T_R = L/v_g$, where L is the cavity length, v_g is the group velocity of the light propagating in the cavity. Change of the cavity length would change f_r and realize accordion-like expansion and contraction of the cavity modes. Since the absolute frequencies of the cavity modes are usually much larger than the offset frequency f_0, the tuning of f_r provides a coarse frequency control method of the OFC spectrum. Detection of f_r is quite straightforward with the coherent and phase-locked properties of the cavity modes as the beating signal of two neighboring modes provides the information of f_r. If f_r is in

the conventional microwave domain, it is accessible with direct detection of the optical pulses with a signal analyzer.

Steady periodic optical pulses require a fixed phase relationship between the cavity modes, which means that different modes should evolve with the same phase velocity. This strict condition is not possible in dispersion materials. The deleterious effect of dispersion can be countered by the Kerr nonlinearity with an avoidable offset frequency f_0. The value of f_0 depends on the dispersion induced phase of the carrier-envelope. It is found that the measurement and stabilization of f_0 are crucial in the generation of OFCs. Fig. 1.1 shows a method proposed in 1999 to measure f_0 with nonlinear self-referencing [3]. A cavity mode with frequency ν_N at the lower end of the spectrum is frequency-doubled to $2\nu_N$. The frequency-doubled light will interfere with the mode at ν_{2N}, which is the closest mode to the light at frequency $2\nu_N$. The beating signal has a frequency of f_0 since

$$2\nu_N - \nu_{2N} = 2\times(N\times f_r + f_0) - (2N\times f_r + f_0) = f_0 . \quad (1.2)$$

Eq. (1.2) is mathematically simple, but it requires an octave spanning optical spectrum, which is challenging to realize. Supercontinuum generation is a key technique to generate octave-spanning spectrum [4].

1.1.2 The applications of optical frequency combs

Because of the highly coherent cavity modes and ultrabroad spectrum, OFC sources are widely used in different areas that require high precision frequency measurement and

synthesis, especially for accurate optical frequency measurement and distance measurement.

The most important application of OFCs is the measurement of the absolute frequency of an optical signal. Before OFCs, cesium atomic clocks are used as a frequency reference to increase the measurement precision. This method requires a series of phase-locked oscillators to connect the microwave domain to the optical domain [5]. The system is bulky, complex and very large scale [2]. It is not practical to use the system to perform a high-precision optical frequency measurement in most cases. A compact comb source can be applied instead of multiple oscillators to simplify the system for practical applications. The measurement of the optical frequency can be accomplished by interference between OFC and the optical signal.

Distance measurement is another important application of OFCs. Fig. 1.2 illustrates two OFC based ranging techniques, direct time of flight (TOF) method with coarse resolution and dual-comb linear optical sampling (LOS) method with fine resolution [6,7]. In Fig. 1.2, single comb TOF method involves only comb 1 and the distance is determined by measuring the delay between the known reference (green pulse) and the target (red pulse). The resolution of this method is theoretically limited by the pulse train period of the comb source but in most cases, the practical limitation is the long response time of photodetectors. For a photodetector with a response time of 0.02 ns (very short for commercially available photodetectors), the TOF method resolution is about 6 mm. The dual comb LOS method increases the resolution from millimeter to

nanometer when compared with the TOF method. The major drawback of distance measurement by OFC is the high cost and high system complexity which could be overcome with the development of microcavity based OFCs.

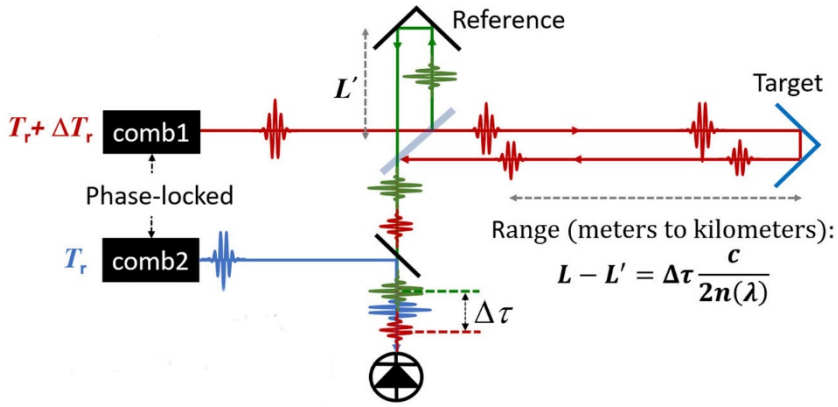

Fig. 1.2 Single comb time of flight method and dual-comb LOS method [1].

Besides the applications mentioned above, other applications including molecular fingerprinting, attosecond control of electronic processes, and methane detection have been demonstrated [8-11]. However, MLLs are complex, have large sizes and high-power consumption. Microcavity based OFCs, which are also called microcombs, are attractive candidates with compact configuration when compared with MLLs. Besides, microcombs have the potential for miniaturization with high repetition rates > 10 GHz. Compatibility with on-chip integration can simplify large-scale manufacturing and eventually lead to widespread application of frequency comb technology.

1.2 Microcavity based optical frequency combs

1.2.1 Development of microcombs

Microcombs have been demonstrated in different micro- and nano-cavities that exhibit high Q factors, including microring [12], microdisk [13], and microtoroid [14] resonators. Fig. 1.3 shows the three kinds of microcavities. The first microcomb was demonstrated by Del'Haye et. al. in 2007 with a silicon microtoroid resonator [15]. The generated pulses are not mode-locked and the comb is in modulation instability (MI) state. The first mode-locked microcomb was demonstrated in a magnesium fluoride microcavity by T. Herr et. al. at 2014 [14]. A soliton state microcomb was achieved for the first time. However, crystal microcavity fabricated by mechanically polishing is not suitable for chip-scale integration. To realize chip-scale microcomb sources, different material platforms have been investigated and soliton state microcombs have been demonstrated in silicon nitride [16], lithium niobate [17], and aluminum nitride [18] microring resonators, etc.

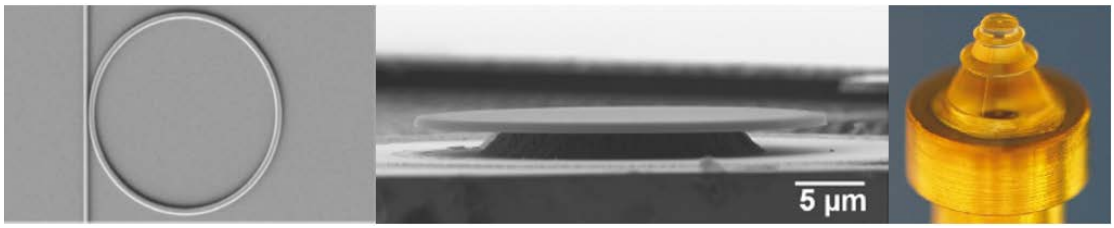

Fig. 1.3 Images of a microring [12], a microdisk [13], and a microtoroid [14] resonator.

1.2.2 Dielectric nonlinear microcavities

Microcombs are generated in dielectric nonlinear microcavities. In this Subsection, we introduce some basic concepts of dielectric nonlinear microcavities.

Free spectral range

The resonance condition of a cavity can be expressed with resonance frequencies or resonance wave vectors. The resonance frequencies ω_m of a cavity are determined by the light roundtrip time $T_R = nL/c$, where n is the refractive index of the cavity, L is the roundtrip length of the light inside the cavity and c is the speed of light

$$\omega_m = m2\pi / T_R. \tag{1.3}$$

The mode number m represents the m-th mode of the mode family. The resonance wave vectors k_m are determined by the cavity length as

$$k_m = m2\pi / L = \omega_m T_R / L. \tag{1.4}$$

Because of material and geometrical dispersion, different resonance modes have different refractive indices. The difference between adjacent resonance frequencies of a mode family is defined as the free spectral range (FSR) which equals to the inverse of cavity roundtrip time,

$$FSR = 1/T_R. \tag{1.5}$$

OFC generation in microcavities is excited by the injection of an external continuous wave (cw) laser.

Dispersion

Microcomb generation is determined by the effects of material dispersion and geometric dispersion [19]. The material dispersion is due to the frequency dependence of the refractive index. The geometric dispersion is due to the geometric mode profile of light inside the cavity. In a microcavity pumped by a cw laser, it is convenient to use relative mode number μ instead of the absolute mode number m, where $\mu = 0$ is the pumped mode. The resonance wave vectors k_μ can be written as

$$k_\mu = k_0 + D_1\mu + \frac{1}{2}D_2\mu^2 + \frac{1}{6}D_3\mu^3 ... \tag{1.6}$$

Here D_1 is the mode wave vector spacing and $2\pi/D_1$ denotes the cavity length. D_2 and D_3 are the second and third order dispersion, respectively. It should be noted that the wave vector k is expanded about the mode number μ instead of the the frequency ω. The definition of dispersion coefficients here is different from the usual dispersion coefficients defined in optical fibers (see Appendix D).

Q factor

At present, microcombs are only observed in microcavities with a high Q factor. The Q factor of a cavity is defined as 2π times the ratio of energy stored in the cavity U_{cav} to energy dissipated per oscillation cycle U_{diss}. In a weakly damped oscillator, the quality factor can be expressed as

$$Q = 2\pi\frac{U_{\text{cav}}}{U_{\text{diss}}} = \frac{\omega}{\alpha}, \tag{1.7}$$

where ω is the resonance frequency and α is the cavity loss rate [20].

Coupling

In this thesis, the coupling between microcavities and waveguides are assumed to be linear. Fig. 1.4 shows the schematic model of a typical coupling between two sections of waveguides. The coupling region is treated as a four-port device and the ports are marked with j = 1, 2, …, 4 as shown in Fig. 1.4. For simplicity, the transverse distribution of the field within the waveguides are omitted, and the field at each port is $E_j(z) = E_j e^{-ikz}$ + c.c., with complex field amplitudes E_j, j = 1, 2, …, 4. Here k is the wave vector, c.c. is short for complex conjugate. The scattering matrix for this coupling region can be written as

$$\begin{bmatrix} E_4 \\ E_2 \end{bmatrix} = \begin{bmatrix} \sqrt{1-\theta_c} & i\sqrt{\theta_c} \\ i\sqrt{\theta_c} & \sqrt{1-\theta_c} \end{bmatrix} \begin{bmatrix} E_3 \\ E_1 \end{bmatrix}, \tag{1.8}$$

where θ_c is the power transmission coefficient.

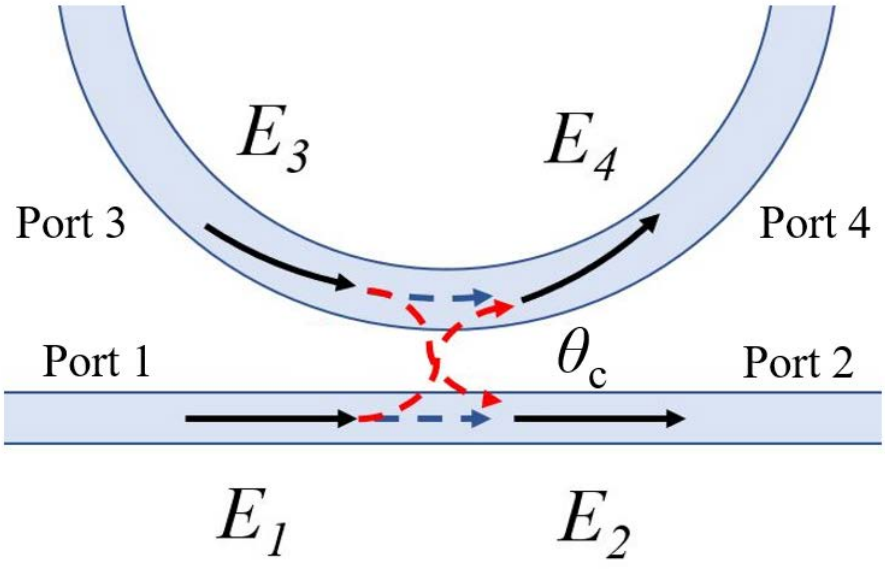

Fig. 1.4 Model of a typical coupling with a straight waveguide and a section of curve waveguide.

1.2.3 Modulation instability and Kerr frequency comb

For a nonlinear microcavity pumped by a cw laser, when the intracavity power exceeds the parametric oscillation threshold, new frequencies are generated through nonlinear processes like MI and four wave mixing (FWM). The microcombs are generated through the cascaded nonlinear processes which are mainly due to the third-order nonlinearity, such combs are usually called Kerr frequency combs.

The formation of Kerr frequency combs involves different stages with various spectral domain behaviors and complex dynamics. A typical method to generate Kerr comb is to fix the power of the pump laser and tune the pump laser frequency over the cavity resonance to achieve a strong intracavity power and initiate the nonlinear processes. The generation of new frequencies starts with the creation of a new signal and idler modes with different frequencies located symmetrically from the pump mode. The first pair of side modes are generated through MI. In Fig. 1.5, when the intracavity power of the pump mode exceeds the MI gain threshold, a pair of new sidebands are generated. The generated new fields are called primary sidebands. This three-mode model can provide insights into the initial dynamics of Kerr combs [21]. Once the primary sidebands are excited, their mixing with the pump through FWM leads to more sidebands with the same spacing. When the pump laser is tuned further into resonance, the intensities of the sidebands increase and mix with each other to produce sidebands far from the pump. The comb spaced by multiple of FSRs is called primary comb as

shown in Fig. 1.5. In the time domain, the formation of a primary comb breaks the cw state into pulses.

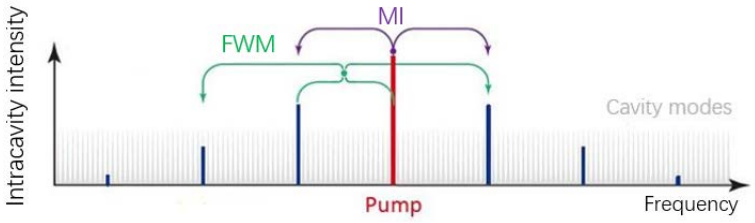

Fig. 1.5 The formation of primary sidebands through MI and primary comb through FWM.

When the intracavity light intensity increases further, the sidebands of the primary comb are strong enough to initiate MI and cascaded FWM around themselves and lead to the formation of secondary comb lines. The spacing of the secondary comb lines is much smaller than the spacing of the primary comb lines as shown in Fig. 1.6. The secondary comb lines around primary comb lines form subcombs in Fig. 1.6.

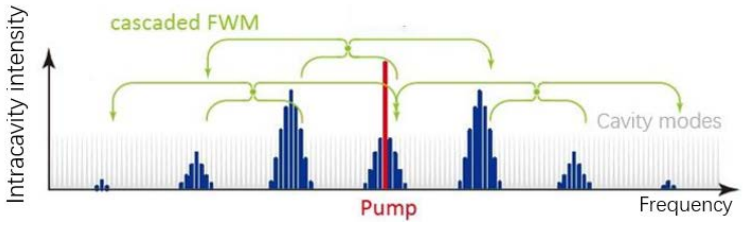

Fig. 1.6 The formation of subcombs around primary comb lines.

By further tuning the pump laser into the cavity resonance, the subcombs expand and merge with each other. All oscillating modes are filled as shown in Fig. 1.7. Because of dispersion, the spacing of the primary sidebands is in general not an integer multiple of the spacing of the the subcombs. When subcombs merge with each other, the mismatch between the spacing of the primary comb lines and subcombs leads to the

mutual incoherence of the resulting Kerr comb. In the time domain, the formation and merging of the subcombs break the stable pulse into chaotic intracavity waveform. This "noisy" comb state is usually called chaotic MI.

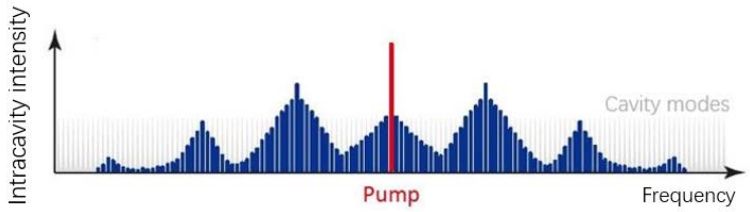

Fig. 1.7 The subcombs merge with each other and form a "noisy" Kerr comb.

1.2.4 Soliton microcombs

The low coherence of Kerr frequency combs and their chaotic intracavity waveforms limit the number of applications which microcombs could be used. A low-noise Kerr comb state can be achieved in microcavities by phase synchronization of the comb lines (also known as mode-locking). This comb state is associated with the formation of intracavity optical solitons [22]. The solitons are called dissipative Kerr solitons (DKS) because they only exist in dissipative system and the governing nonlinearity is the Kerr nonlinearity. DKSs are also referred to as "Temporal solitons" or "solitons" in the area of Kerr combs. DKSs are localized pulses that circulate in the driven cavity and maintain their shape because of the balance between nonlinearity and dispersion as well as dissipation and gain [23]. DKSs formed in the cavities can be in single-soliton state or multiple-soliton state (also known as soliton molecule state) as shown in Fig. 1.8.

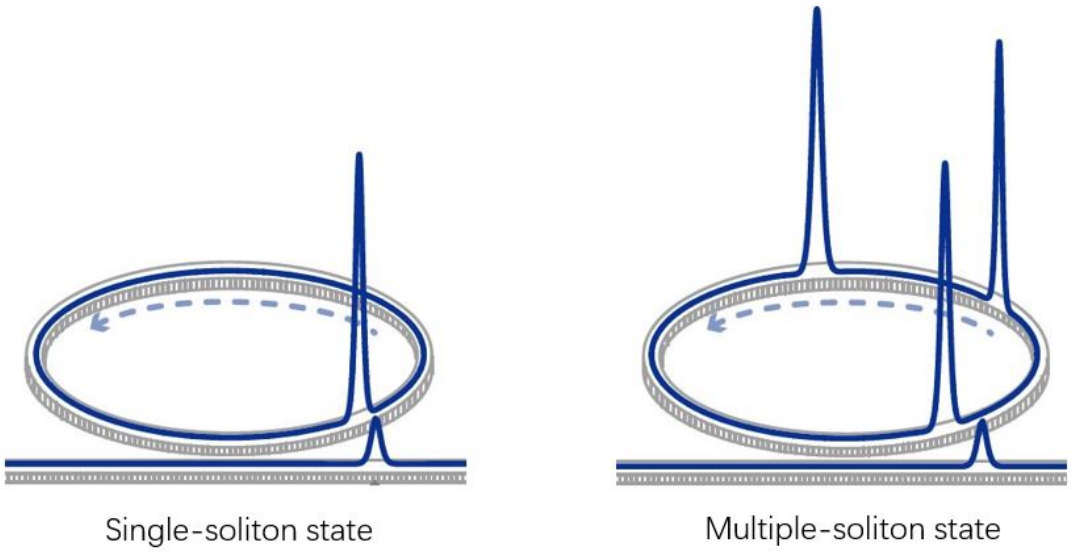

Fig. 1.8 Single-soliton and multiple-soliton states in the cavity.

A soliton microcomb does not appear spontaneously from small perturbations of the cw pump. It needs an excitation mechanism. In experiments, one of the simplest and most employed techniques is excitation via laser tuning [14]. In Fig. 1.9, a cw pump laser is scanned from the blue-detuned to the red-detuned region of a cavity resonance to excite the chaotic MI state. With further tuning of the pump, only the most intense MI pulses converge to a soliton state. This soliton formation method does not require complex elements such as a modulator or a pulsed laser. However, a narrow linewidth tunable cw laser is still a big challenge to realize integrated microcombs.

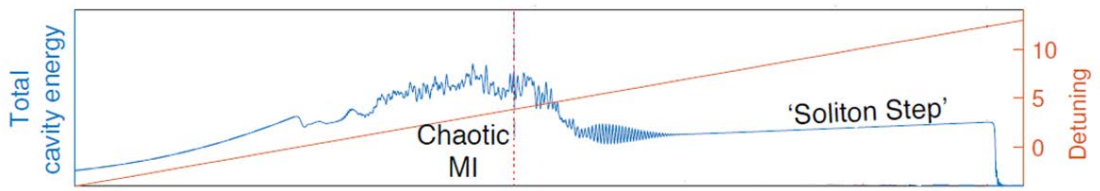

Fig. 1.9 Evolution of the total intracavity energy (blue) upon sweeping the detuning (red) of a cw pump laser from the blue-detuned to red-detuned side of a cavity resonance. The initial cw state becomes unstable with the excitation of MI (eventually chaotic MI). With further tuning of the pump laser, the chaotic MI converges into soliton states and form the "soliton step" [14].

The formation of soliton states in microcavities have revolutionized the area of Kerr combs and are the focus of the present study. Soliton microcombs have been demonstrated in chip-integrated compatible platforms with the advantages of mass-producibility, chip scale footprint as well as the possibility for heterogeneous integration with laser sources and other electro-optic components [24]. Compared with traditional MLL combs, microcombs are distinguished by their inherent wider mode-spacing. Limited by the gain medium, the FSRs of MLL combs are at most 10 GHz [25], while the repetition rates of microcombs can be up to 1 THz [26]. With the above advantages, soliton microcombs have been applied in various fields including coherent optical communication [27], LIDAR [28], astrocombs [29, 30], dual-comb spectroscopy [31], ultrafast optical ranging [32, 33], optical clock [34], microwave to optical link [35], and optical frequency synthesizer [26].

1.2.5 Challenges for soliton microcomb generation

Access to soliton state

As discussed in Section 1.2.4, the transition from cw state to soliton state requires excitation. Using a tunable laser to trigger the soliton state is the most common method used in experiments [36-38]. However, a tunable cw laser suitable for soliton comb generation should be stable against temperature, with narrow linewidth (< 100 kHz), and mode-hop-free. Such lasers are large and require high power as shown in Fig. 1.10. These features make them unsuitable for chip-scale integration.

Fig. 1.10 Two narrow linewidth tunable cw lasers for triggering soliton microcombs: Santec TSL-770 [39] and Toptica DLC pro [40].

Another way to achieve fast optical frequency sweeping is using a single sideband suppressed-carrier frequency shifter [41,42]. As shown in Fig. 1.11, it is composed of a dual-parallel Mach-Zehnder intensity modulator driven by a wideband voltage-controlled oscillator. This method enables fast frequency scanning, but the frequency sweeping range is limited to several GHz and the complex set-up is also unsuitable for integration.

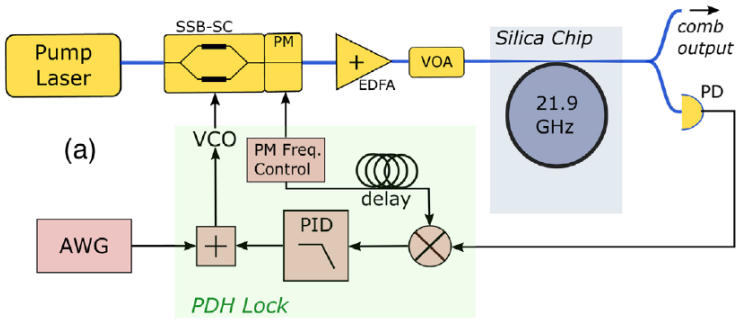

Fig. 1.11 Schematic of fast optical frequency sweeping by using a single-sideband suppressed-carrier frequency shifter [42].

The purpose of sweeping the pump laser frequency is to vary the detuning between the pump and the cavity resonance. Thus, equivalently, tuning the cavity resonances while the pump frequency stays fixed should also trigger the soliton microcombs. The sweeping of the cavity resonance can be achieved by using a microheater to thermally control the microcavity [43-45]. In Fig. 1.12, to achieve a large sweeping range, nearly the whole cavities are covered by the microheaters. The cavity resonances are tuned by the intensity of the current flowing inside the microheaters. When the size of the microcavity increase, the size of the microheater needs to increase accordingly. It is hard to keep the microheaters stable against temperature when their sizes are large. Although microheaters are available for integration, using microheaters to tune the cavity resonance and trigger soliton microcombs is only applicable to small microcavities which have large FSRs. Soliton comb generation triggered by microheaters in microcavities with FSRs below 100 GHz has not been experimentally reported. 100 GHz is beyond their detection range for commercial photodetectors. Thus, sweeping the detuning between the pump laser and the cavity resonances in an

integrated microcomb source with detectable microcavity size (FSR < 70 GHz) remains a challenge for soliton microcomb generation.

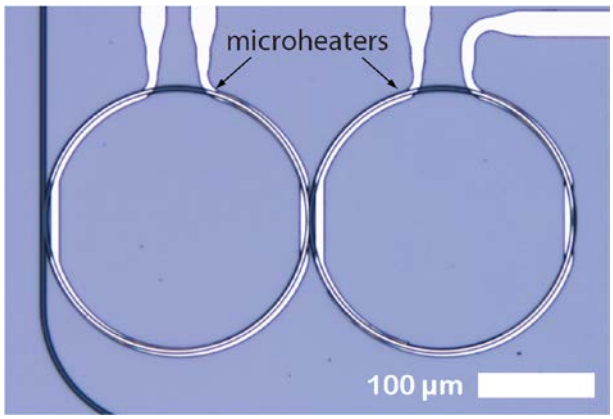

Fig. 1.12 Coupled microcavities tuned by microheaters [44].

Low loss requirement for microcavities

At present, microcombs have been experimentally demonstrated only in high Q microcavities ($Q > 10^6$) with low intrinsic loss. As discussed in Section 1.2.3, the initiation of microcombs requires the MI gain to surpass the cavity loss. In experiments, only high Q microcavities can satisfy this requirement. The total loss of a microcavity is due to the absorption of the cavity material and scattering losses induced by the rough sidewalls of the waveguides. The low loss requirement limits the microcavity fabrication in two aspects.

Firstly, the cavity size is limited because the total loss is proportional to the length of the waveguide. Recall that the cavity size determines the bandwidth of the photodetector that can detect the microcombs generated in such cavities. Larger cavity size equals to lower cost (high bandwidth detection devices are extremely expensive. The price of an 80 GHz oscilloscope is more than 150 thousand US dollars). Besides

the expense of using ultrasmall microcavities, the lack of low repetition rate combs (FSR < 10 GHz) also limits the application of microcombs.

Secondly, the low loss requirement also limits the choice of materials for microcomb generation [46]. Materials with high Kerr nonlinear coefficient and wide transparent range like silicon and chalcogenide cannot be used for soliton microcomb generation because of their relatively high propagation loss [47-50]. Even for materials with low intrinsic loss like silicon nitride and lithium niobate, they require complex and expensive processing to fabricate high Q microcavities [51-53]. The generation of soliton microcombs does not require broad spectral gain medium as in the case of MLLs. This provides opportunities for the generation of combs at new operating wavelengths not available so far. However, the limitation of materials with low intrinsic loss for soliton microcomb hinders the development of new wavelengths for comb generation.

To overcome the challenges discussed above, we propose to couple an auxiliary cavity to the main cavity. In this thesis, we present for the first time a theoretical analysis of microcomb generation in such a coupled microcavity system. Both MI comb and soliton comb generations are studied analytically and numerically.

1.3 Thesis outline

Chapter 2 gives a brief introduction of coupled microcavity systems and numerical models used in this thesis. In recent years, the coupled microcavity system draw attention in the study of PT asymmetry and microcomb generation. We review the major results of these studies to show the originality of the work in this thesis. Coupled

mode equations and Ikeda map are used in this thesis to study MI and soliton generation in coupled microcavities.

Chapter 3 discusses MI generation in coupled nonlinear microcavities. We found that a new blue-detuned MI generation region is induced by the coupling of an auxiliary cavity to the main cavity. The parameters of the auxiliary cavity that influence the new MI region are analyzed in detail. Numerical simulations of MI and MI comb generation are presented.

Chapter 4 describes the investigation of soliton microcomb generation in coupled nonlinear microcavities. We propose a new soliton microcomb excitation method by tuning the coupling between the two cavities. We explain the soliton excitation mechanism with the additional figure-8 optical path introduced by the coupling of the auxiliary cavity. The same principle can be applied to a single microcavity with clockwise (CW) and counter-clockwise (CCW) mode coupling. We then study soliton microcomb generation in low Q microcavities by coupling with auxiliary gain cavity.

Chapter 5 is a summary of the thesis and the future work plan.

2 Coupled microcavity system and theoretical models

2.1 A brief review of recent research on coupled microcavity system

2.1.1 Coupled linear microcavity

In recent years, coupled microcavity systems have attracted interest especially in the study of parity-time symmetry and exceptional points in photonics [54-56]. These researches only consider linear microcavities which do not support microcomb generation. Thus, we only focus on the experimental techniques developed from such studies.

The first important technique is the fabrication of different microcavities on the same chip. This technique makes it possible to fabricate the two microcavities in the coupled system with different sizes, losses, dispersion, nonlinearity and other parameters. A pair of gain-loss coupled micro-disk cavities are commonly used in the study of parity-time symmetry as shown in Fig. 2.1(a) and 2.1(b) [55]. The two microcavities are fabricated as one loss cavity and one gain cavity. Micro-disk cavities cannot be mass produced yet. Thus, currently they are used only in scientific research. With the development of hybrid integration technique [57], mass production of microcavities with different properties on the same chip will not be far away.

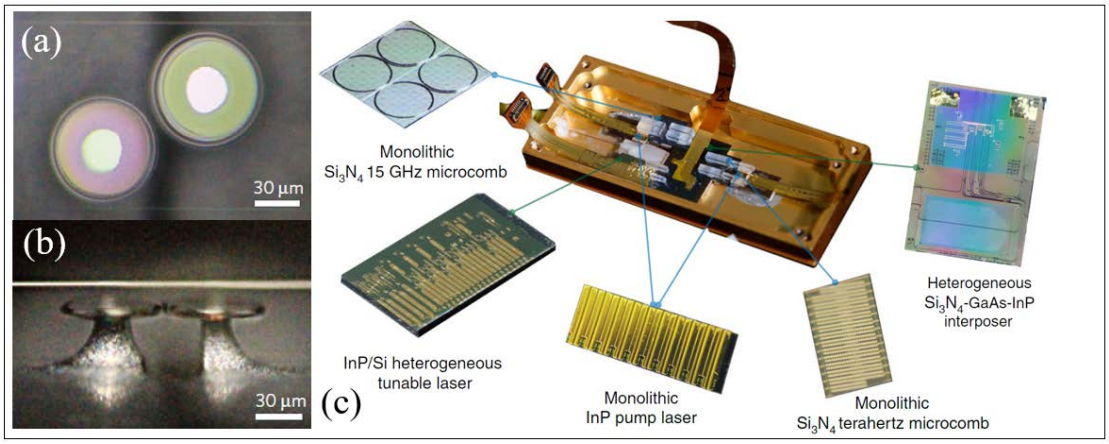

Fig. 2.1 (a) Top view and (b) side view of two coupled gain-loss micro-disk cavities [55]. (c) A chip-scale microcomb source with hybrid-integration technique [57].

Another important technique is tuning the coupling coefficient between two coupled microcavities. The coupling between two microcavities can be tuned by adjusting the gap between the microcavities. In micro-disk cavities, the gap adjustment can be achieved by mechanical movement of the microcavities [58]. This method is shown in Fig. 2.2(a) and 2.2(b). Two silica micro-disk cavities are fabricated on the edge of two silicon substrates. Thus, the gap between the two microcavities can be adjusted by moving the substrates. This method is obviously not suitable for integration. For microring cavities, the gap between the two cavities can be adjusted by integrating a microheater at the coupling region [59]. As shown in Fig. 2.2(c), the coupling coefficient at the coupling points G_1 and G_2 can be tuned by controlling the current through the microheaters.

Microheaters are widely used in various applications including gas sensors [60], microcalorimeters [61], gas flow meters [62], infrared sources [63], and thermal management [64]. Many structure designs have been proposed to optimize the

performance of microheaters. The temperature of metal oxide heating films can be up to 700 ℃ [65]. By using an innovative layout of the heating wires, the temperature variation of the heated area can be lower than 1% at 135 ℃ and the microheater is stable after a stress test at 530 ℃ for 120 hours [66]. For a microheater with a size of 1 cm × 1 cm, the heating efficiency can be up to 135 ℃/W [67]. Thus, there are well developed techniques for tuning the coupling between microcavities by microheaters with high efficiency and stability. As the fabrication of microheaters is compatible with CMOS fabrication process, the microheaters can be mass fabricated at low cost.

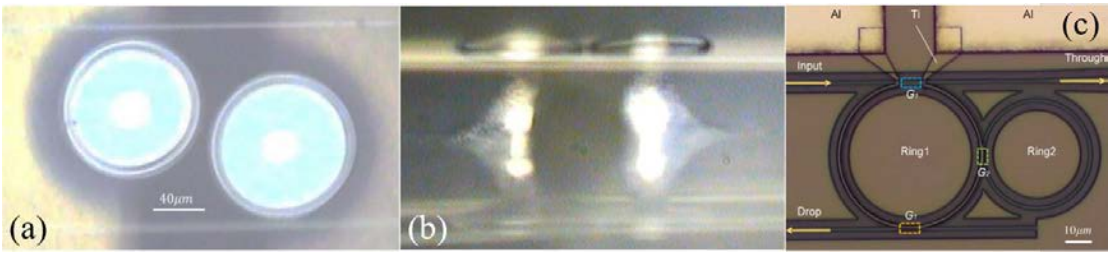

Fig. 2.2 (a) Top view and (b) side view of the coupled silica micro-disk resonators [58]. (c) Microscope image of the controllable coupled microcavities controlled by microheaters [59].

2.1.2 Coupled nonlinear microcavity for microcomb generation

Microcomb generation in coupled nonlinear microcavities has been investigated mainly in two aspects, namely microcomb generation in normal dispersion microcavities [68-73] and improvement in pump power efficiency [74].

It is well known that MI occurs in Kerr nonlinear waveguide with anomalous dispersion [75]. Microcomb generation in normal dispersion microcavities has often been thought difficult because of the lack of MI. However, normal dispersion is easy to access in most nonlinear materials at the communication band. It has been reported that

MI occurs in normal dispersion resonators through coupling between different modes [76]. A coupled microcavity system was demonstrated to achieve soliton microcombs in normal dispersion microcavities in Fig. 2.3 [68]. The mode interaction in this coupled system induces equivalent “anomalous dispersion” in normal dispersion microcavities to achieve MI generation.

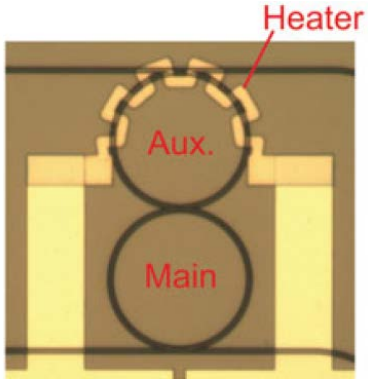

Fig. 2.3 Coupled microcavity system for microcomb generation in normal dispersion cavities [68].

Coupled microcavity systems have also been used to achieve efficient temporal soliton generation. The mutually coupled cavities provide a pump recycling scheme to improve the pump to soliton energy conversion. The concept is shown in Fig. 2.4, one nonlinear cavity for soliton generation is coupled to one linear pump cavity for pump recycling [74]. The soliton microcomb propagates in the soliton cavity, while the pump cavity recycles the pump field to maximize energy transfer from the pump to the soliton.

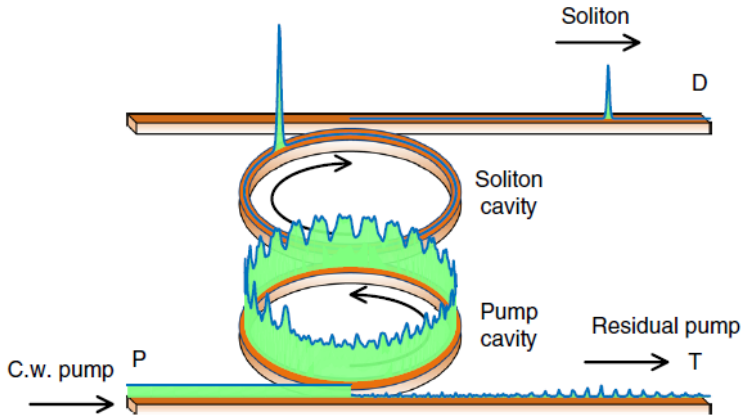

Fig. 2.4 Scheme of soliton comb generation in coupled microcavity with pump recycling [74].

As discussed in Section 1.2.4, the trigger of DKSs in microcavities requires red-detuned pump lasers. Experimentally generated soliton microcombs reported so far are with the frequencies of the cw pump lasers in the red-detuned region [14-18, 24]. The research of microcomb generation with a blue-detuned pump laser in this thesis is original.

2.2 Theoretical models

Microcomb generation involves the generation of a series of dissipative cavity modes in a microcavity with dispersion, Kerr nonlinearity and a cw pump [14]. The optical field propagation inside the microcavities can be described by models either in the temporal or the spectral domain. For models in the spectral domain, the motion of each cavity mode is described by a separate equation coupled through FWM. This set of coupled equations is referred to as the coupled mode equations (CMEs) [21]. CMEs are useful for calculating the threshold of parametric oscillation [77] and determining the primary comb lines in microcomb generation [78]. We use CMEs to study MI

generation in nonlinear microcavities. However, this model is computationally demanding for the simulation of wide band microcombs. The complexity of calculation increases exponentially with the number of modes simulated [79]. For wideband microcomb generation, a temporal model is more appropriate. In this thesis, we use the Ikeda map model [80] to investigate the soliton microcomb generation. Ikeda map treats the optical fields propagation and coupling separately. It can describe the rapid changes of the light in one roundtrip such as in a coupled microcavity system.

2.2.1 Coupled mode equations

CMEs consider a series of cavity modes in the same transverse mode family. The optical field of each mode can be described by

$$\frac{\partial A_\mu}{\partial z} = -ik_\mu A_\mu - \frac{\alpha}{2} A_\mu + i\gamma \sum_{\mu_1,\mu_2,\mu_3} A_{\mu 1} A_{\mu 2} A_{\mu 3}^{\ *} + i\delta_{\mu 0}\sqrt{\theta} F \exp\left(-ik_{\text{pump}} z\right), \tag{2.1}$$

where μ is the relative mode index, A_μ and k_μ denote the amplitude and the resonance wave vector of the μ-th mode, respectively. z is the evolution variable in one roundtrip. α is the cavity loss rate, γ is the Kerr nonlinear coefficient and θ is the power coupling coefficient between the cavity and pump waveguide. F and k_{pump} are the amplitude and wave vector of the pump laser, respectively. $\delta_{\mu 0}$ is the Kronecker delta function, it equals 1 or 0 for $\mu = 0$ and $\mu \neq 0$, respectively. Each mode is coupled with other modes through FWM as shown in the third term of the right-hand side of Eq. (2.1). We transform Eq. (2.1) to a relative wave vector frame where

$$A_\mu = a_\mu \exp\left[-i\left(k_{\text{pump}} + D_1\mu\right) z\right]. \tag{2.2}$$

Here, a_μ is the amplitude of the μ-th mode in the relative wave vector frame. Note that the pump laser is injected near the 0-th comb line, and $k_{\text{pump}}+D_1\mu$ is the wave vector of the μ-th comb line with D_1 is the mode wave vector spacing. Substitution of Eq. (2,2) into Eq. (2.1), we have

$$\frac{\partial a_\mu}{\partial z} = -i\left(k_\mu - D_1\mu - k_{\text{pump}}\right)a_\mu - \frac{\alpha}{2}a_\mu + i\gamma \sum_{\mu_1,\mu_2,\mu_3} a_{\mu 1}a_{\mu 2}a_{\mu 3}^{\ *} + i\delta_{\mu 0}\sqrt{\theta}F. \qquad (2.3)$$

We expand the wave vector k_μ by Eq. (1.6) and neglect dispersion beyond the second order, we obtain

$$\frac{\partial a_\mu}{\partial z} = -i\delta k_\mu a_\mu - \frac{\alpha}{2}a_\mu + i\gamma \sum_{\mu_1,\mu_2,\mu_3} a_{\mu 1}a_{\mu 2}a_{\mu 3}^{\ *} + i\delta_{\mu 0}\sqrt{\theta}F, \qquad (2.4)$$

where

$$\delta k_\mu = k_\mu - D_1\mu - k_{\text{pump}} = k_0 - k_{\text{pump}} + \frac{D_2}{2}\mu^2 = \delta k_0 + \frac{D_2}{2}\mu^2. \qquad (2.5)$$

For the investigation of coupled microcavity systems, we modify the CMEs by introducing the coupling between the microcavities. A coupled microcavity system is shown in Fig. 2.5. The main cavity is coupled to an auxiliary cavity and a waveguide. A cw pump laser signal is injected into the main cavity via the waveguide. In this thesis, we aim to investigate how the MI generation in the main cavity is affected by the auxiliary cavity. Thus, for simplicity we first assume that the auxiliary cavity is linear when we study MI generation in coupled microcavity systems. In Chapter 3, we will show that the MI generation condition in the main cavity can be analytically determined if the auxiliary cavity is linear.

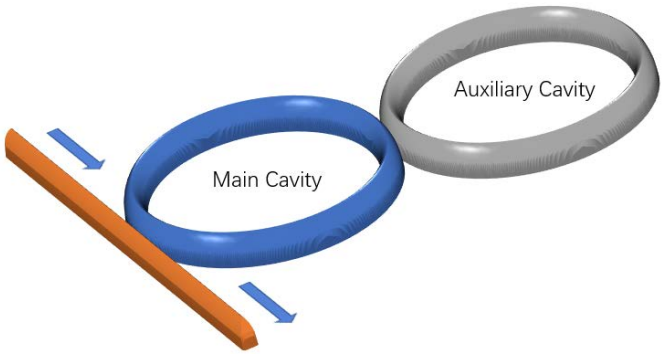

Fig. 2.5 Schematic of a coupled microcavity system for MI generation.

The evolutions of the intracavity optical fields inside the coupled cavities are then modeled by

$$\frac{\partial A_\mu}{\partial z} = -ik_\mu A_\mu - \frac{\alpha}{2}A_\mu + i\gamma \sum_{\mu_1,\mu_2,\mu_3} A_{\mu 1}A_{\mu 2}A_{\mu 3}^{\ *} + i\sqrt{\theta_c}A'_{\mu'} + i\delta_{\mu 0}\sqrt{\theta}F\exp\left(-ik_{\text{pump}}z\right), \quad (2.6)$$

$$\frac{\partial A'_{\mu'}}{\partial z} = -ik'_{\mu'}A_\mu - \frac{\alpha'}{2}A'_{\mu'} + i\sqrt{\theta_c}A_\mu. \quad (2.7)$$

Symbols of the main cavity are defined as that for single cavity in Eq. (2.1). θ_c is the power coupling coefficient between the two microcavities. μ' denotes the mode index of the auxiliary cavity which couples with the μ-th mode of the main cavity. Since the sizes of the two microcavities can be different, μ' and μ can be different. $A'_{\mu'}$ and $k'_{\mu'}$ are the amplitude and wave vector of the μ'-th mode, respectively. α' is the loss rate of the auxiliary cavity. Similar to the single microcavity, we use relative wave vector frames and transform Eq. (2.6) and Eq. (2.7) to

$$\begin{aligned}\frac{\partial a_\mu}{\partial z} = &-i\left(k_\mu - D_1\mu - k_{\text{pump}}\right)a_\mu - \frac{\alpha}{2}a_\mu + i\gamma \sum_{\mu_1,\mu_2,\mu_3} a_{\mu 1}a_{\mu 2}a_{\mu 3}^{\ *} \\ &+ i\sqrt{\theta_c}a'_{\mu'}\exp\left(-iD'_1\mu' z + iD_1\mu z\right) + i\delta_{\mu 0}\sqrt{\theta_1}F,\end{aligned} \quad (2.8)$$

$$\frac{\partial a_{\mu'}{}'}{\partial z} = -i\left(k'_{\mu'} - D'_1\mu' - k_{\text{pump}}\right)a_{\mu'}{}' - \frac{\alpha'}{2}a_{\mu'}{}' + i\sqrt{\theta_c}a_\mu\exp\left(-iD'_1\mu' z + iD_1\mu z\right), \quad (2.9)$$

where $A'_{\mu'} = a'_{\mu'} \exp\left[-i\left(D'_1\mu' + k_{\text{pump}}\right)z\right]$, and D_1' is the mode wave vector spacing of the auxiliary cavity. When the μ'-th mode of the auxiliary cavity is coupled to the μ-th mode of the main cavity, it requires $D_1'\mu' = D_1\mu$. Thus, we have

$$\frac{\partial a_\mu}{\partial z} = -i\delta k_\mu a_\mu - \frac{\alpha}{2}a_\mu + i\gamma \sum_{\mu_1,\mu_2,\mu_3} a_{\mu 1} a_{\mu 2} a_{\mu 3}^{\ *} + i\sqrt{\theta_c}\, a'_{\mu'} + i\delta_{\mu 0}\sqrt{\theta_1}F, \quad (2.10)$$

$$\frac{\partial a_{\mu'}{}'}{\partial z} = -i\delta k'_{\mu'} a_{\mu'}{}' - \frac{\alpha'}{2}a_{\mu'}{}' + i\sqrt{\theta_c}\, a_\mu. \quad (2.11)$$

Here,

$$\delta k'_{\mu'} = k'_{\mu'} - D_1'\mu' - k_{\text{pump}} = k'_0 - k_{\text{pump}} + \frac{D'_2}{2}\mu'^2 = \delta k'_0 + \frac{D'_2}{2}\mu'^2. \quad (2.12)$$

2.2.2 Ikeda map

We use Ikeda map to analyze and simulate soliton microcomb generation in microcavities. Ikeda map models the optical field propagation in a resonant cavity system [81]. Ikeda map combines the Generalized Nonlinear Schrödinger Equation (GNLSE) [82] describing the intracavity light propagation, together with the boundary conditions relevant to the fields between successive roundtrips and the input pump field [83, 84]. The field propagation of the s-th roundtrip in the microcavity is described by

$$\frac{\partial E_s(t,z)}{\partial z} = -i\delta k_0 E_s(t,z) - \frac{\alpha}{2}E_s(t,z) - i\frac{\beta_2}{2}\frac{\partial^2 E_s(t,z)}{\partial t^2} + i\gamma\left|E_s(t,z)\right|^2 E_s(t,z), \quad (2.13)$$

$$E_{s+1}(t,0) = \sqrt{1-\theta}E_s(t,L) + i\sqrt{\theta}F, \quad (2.14)$$

where t is time, δk_0 is the wave vector detuning from the cavity resonance closest to the pump frequency, β_2 is the group velocity dispersion, and L is the cavity length. The

higher-order dispersion and the frequency dependence of the nonlinear coefficient is not the dominant effects of soliton microcomb generation. Thus, in this thesis, we neglect these terms for simplicity. Eq. (2.13) can be extended to include any higher-order effects. Eq. (2.14) is the boundary condition that determines the intracavity field $E_{s+1}(t, z = 0)$ at the input of (s+1)-th roundtrip in terms of the field from the previous roundtrip $E_s(t, z = L)$ and the pump field F.

In this thesis, we use a set of modified Ikeda map to model soliton comb generation in coupled microcavities. The coupled microcavity system under investigation is shown in Fig. 2.6. In Section 2.2.1, we assume the auxiliary cavity is linear such that analytical results for MI generation in the main cavity can be obtained using CMEs. The CMEs adopt a modal expansion approach for studying microcomb generation in nonlinear microcavities in the frequency domain. The CMEs are best to describe the evolution of each discrete resonance mode of the comb spectrum. The Kerr nonlinearity couples the modes through the FWM term in Eq. (2.10). When there are a large number of modes in the comb spectrum (e. g. in soliton microcombs), numerical simulations of comb generation with CMEs are computationally demanding. Ikeda map is used to numerically study soliton microcomb generation in coupled microcavities instead. The Ikeda map provides a description of the FWM process owing to the Kerr nonlinearity in the time domain. Numerical simulation with Ikeda map can be solved efficiently by using standard numerical tools developed for the simulation of GNLSE in optical fibers based on the split-step Fourier method [82]. Compared to numerical simulations with

CMEs, numerical simulations with Ikeda map allow significant improvement in computational time which permit simulations of broadband microcombs such as soliton combs consisting of hundreds or thousands of resonant modes.

In Fig. 2.6, we consider the case where a nonlinear main cavity is coupled to a nonlinear auxiliary cavity and a bus waveguide. A cw pump is coupled to the main cavity through the waveguide. The coupling coefficient between the waveguide and the main cavity is θ and the coupling coefficient between the two cavities is θ_c.

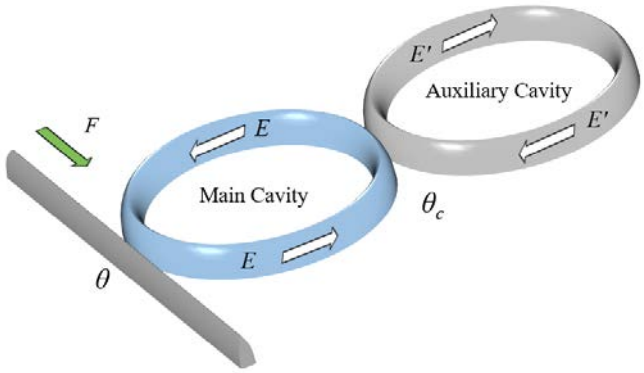

Fig. 2.6 Coupled microcavity system for soliton microcomb generation.

The modified Ikeda map modeling the system is

$$\frac{\partial E_s(t,z)}{\partial z} = -i\delta k_0 E_s(t,z) - \frac{\alpha}{2} E_s(t,z) - i\frac{\beta_2}{2}\frac{\partial^2 E_s(t,z)}{\partial t^2} + i\gamma \left|E_s(t,z)\right|^2 E_s(t,z), \tag{2.15}$$

$$\frac{\partial E_s'(t,z)}{\partial z} = -i\delta k_0' E_s'(t,z) - \frac{\alpha'}{2} E_s(t,z) - i\frac{\beta_2'}{2}\frac{\partial^2 E_s'(t,z)}{\partial t^2} + i\gamma' \left|E_s'(t,z)\right|^2 E_s'(t,z), \tag{2.16}$$

$$E_s(t, L_+/2) = \sqrt{1-\theta_c} E_s(t, L_-/2) + i\sqrt{\theta_c} E_s'(t, L'), \tag{2.17}$$

$$E_{s+1}'(t,0) = \sqrt{1-\theta_c} E_s'(t, L') + i\sqrt{\theta_c} E_s(t, L_-/2), \tag{2.18}$$

$$E_{s+1}(t,0) = \sqrt{1-\theta} E_s(t,L) + i\sqrt{\theta} F. \tag{2.19}$$

Eqs. (2.15) and (2.16) describe the intracavity fields evolution inside the main cavity and the auxiliary cavity, respectively. The symbols used for the main cavity in Eq. (2.15) are the same as the single microcavity in Eq. (2.13). E_s' denotes the optical field of s-th roundtrip inside the auxiliary cavity. In this thesis, we assume the main cavity and the auxiliary cavity are with identical size and dispersion. The number of roundtrips in the two cavities shown in Eqs. (2.15) and (2.16) are the same. $\delta k_0'$ is the wave vector detuning from the resonance of the auxiliary cavity closest to the pump frequency, α', β_2' and γ' are the loss rate, group velocity and nonlinear coefficient of the auxiliary cavity, respectively. In this thesis, we use the propagation distance of an optical field to mark a position inside the cavity. The subscript + and – denote the points immediately after and before the particular position, respectively. For example, $E_s(t, z = L_+/2)$ is the optical field inside the main cavity at the position immediately after the half point of the main cavity. The positions mentioned in this thesis are shown in Fig. 2.7. Eqs. (2.17) and (2.18) are the boundary conditions that describe the coupling between the two cavities. The intracavity field of the main cavity immediately after coupling $E_s(t, z = L_+/2)$ and the field of the auxiliary cavity at the input of (s+1)-th roundtrip $E_{s+1}'(t, z = 0)$ depend on the field of the auxiliary cavity at the end of the s-th roundtrip $E_s'(t, z = L')$ and the field of the main cavity immediately before the coupling $E_s(t, z = L_-/2)$. The boundary condition that determines the intracavity field of the main cavity at the input of (s+1)-th roundtrip $E_{s+1}(t, z = 0)$ in terms of the pump field and the previous roundtrip $E_s(t, z = L)$ is shown in Eq. (2.19).

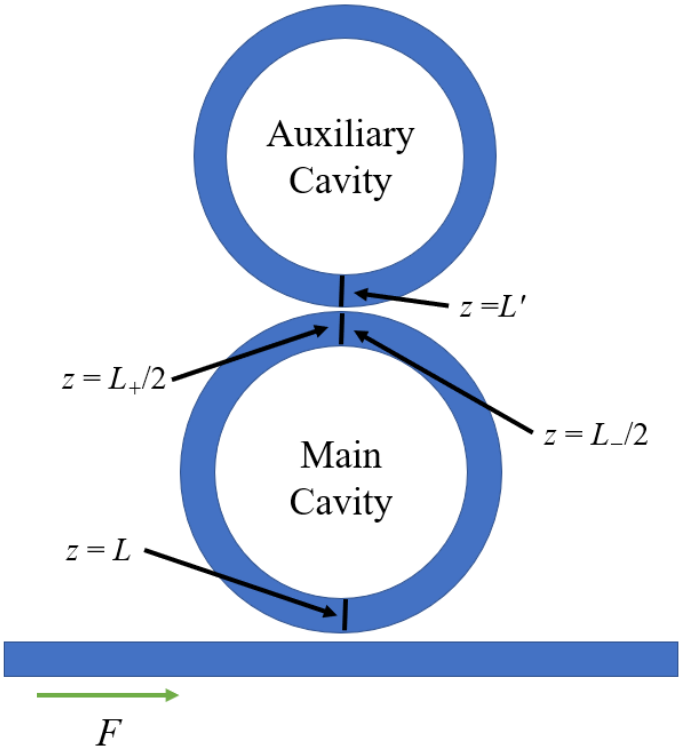

Fig. 2.7 Schematic diagram of coupling points in the coupled microcavities.

3 MI generation in coupled nonlinear microcavity system

In the formation of microcombs, MI plays a crucial role for the initiation of the comb. In this Chapter, we present analytical analysis and numerical simulation of the first pair of MI sidebands generation in a coupled microcavity system. The MI generation marks the emergence of the first pair of sidebands. We start by analyzing MI generation in a single microcavity and then extend the results to the coupled microcavity system.

3.1 MI generation in a single microcavity

3.1.1 Derivation of the MI region

In Fig. 3.1, the pump mode of the microcavity is populated by the external cw pump. Oscillations of the first pair of side modes are initiated by the pump mode through MI.

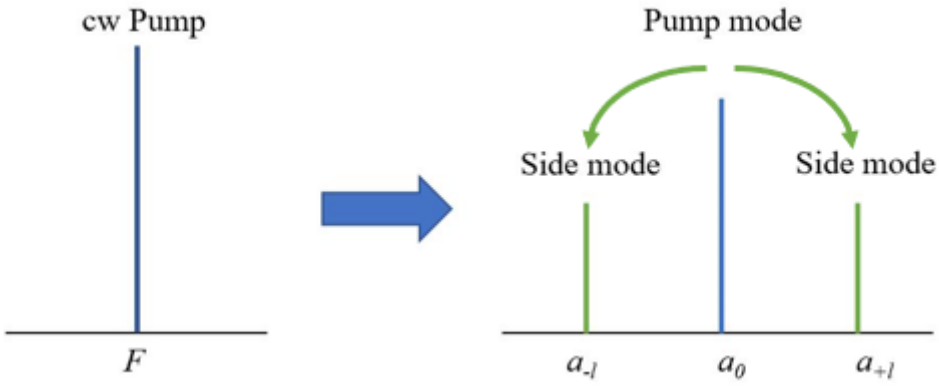

Fig. 3.1 MI generation in a microcavity.

To find the MI region leading to oscillation for a given pair of side modes $a_{\pm 1}$, we investigate the linear stability of the trivial solution $a_{\pm 1} = 0$. We perturb the solution

with small fluctuations $\delta a_{\pm l}$ and the boundary of MI region is defined by the set of the parameters for which the perturbations grow (onset of side modes oscillations). In the stability analysis, we assume only the pump mode a_0 and the pair of side modes $a_{\pm l}$ are oscillating. From Eq. (2.4), the side mode perturbations obey

$$\frac{\partial \delta a_{+l}}{\partial z} = -i\delta k_{+l}\delta a_{+l} - \frac{\alpha}{2}\delta a_{+l} + i\gamma\left(a_0^2 \delta a_{-l}^{*} + 2\left|a_0\right|^2 \delta a_{+l}\right), \tag{3.1}$$

$$\frac{\partial \delta a_{-l}^{*}}{\partial z} = i\delta k_{-l}\delta a_{-l}^{*} - \frac{\alpha}{2}\delta a_{-l}^{*} - i\gamma\left(a_0^{2*} \delta a_{+l} + 2\left|a_0\right|^2 \delta a_{-l}^{*}\right). \tag{3.2}$$

Eqs. (3.1) and (3.2) can be rewritten as

$$\begin{bmatrix} \dfrac{\partial \delta a_{+l}}{\partial z} \\ \dfrac{\partial \delta a_{-l}^{*}}{\partial z} \end{bmatrix} = \begin{bmatrix} -i\delta k_{+l} - \dfrac{\alpha}{2} + 2i\gamma\left|a_0\right|^2 & i\gamma a_0^2 \\ -i\gamma a_0^{2*} & i\delta k_{-l} - \dfrac{\alpha}{2} - 2i\gamma\left|a_0\right|^2 \end{bmatrix} \begin{bmatrix} \delta a_{+l} \\ \delta a_{-l}^{*} \end{bmatrix}. \tag{3.3}$$

At steady state, the side modes are created when at least one of the eigenvalues λ of the secular equation

$$\begin{bmatrix} -i\delta k_{+l} - \dfrac{\alpha}{2} + 2i\gamma\left|a_0\right|^2 - \lambda & i\gamma a_0^2 \\ -i\gamma a_0^{2*} & i\delta k_{-l} - \dfrac{\alpha}{2} - 2i\gamma\left|a_0\right|^2 - \lambda \end{bmatrix} = 0 \tag{3.4}$$

has a positive real part. Solving Eq. (3.4), we have

$$\lambda_{\pm} = \left(-i\delta k_{+l} + i\delta k_{-l} - \alpha\right) \pm \sqrt{-\left(\delta k_{-l} + \delta k_{+l} - 4\gamma\left|a_0\right|^2\right)^2 + 4\gamma^2\left|a_0\right|^4}. \tag{3.5}$$

Thus, the MI generation requires

$$-\alpha + \sqrt{-\left(\delta k_{-l} + \delta k_{+l} - 4\gamma\left|a_0\right|^2\right)^2 + 4\gamma^2\left|a_0\right|^4}\,] > 0. \tag{3.6}$$

Since α is the cavity loss, the MI gain G_{MI} is given by

$$G_{\mathrm{MI}} = \sqrt{-\left(\delta k_{-l} + \delta k_{+l}\right)^2 + 8\left(\delta k_{-l} + \delta k_{+l}\right)\gamma\left|a_0\right|^2 - 12\gamma^2\left|a_0\right|^4}. \tag{3.7}$$

From Eq. (3.6), the side modes are created when the MI gain is larger than the cavity loss. Substitution of Eq. (2.5) into Eq. (3.7), we have

$$G_{\mathrm{MI}} = \sqrt{-\left(2\delta k_0 + D_2 l^2\right)^2 + 8\left(2\delta k_0 + D_2 l^2\right)\gamma \left|a_0\right|^2 - 12\gamma^2 \left|a_0\right|^4}. \qquad (3.8)$$

From Eq. (3.8), the MI gain is a function of the pump mode wave vector detuning δk_0 and the pump mode power $|a_0|^2$. For a fixed δk_0, the maximum MI gain is given by

$$G_{\mathrm{MI,max}} = \frac{\delta k_{-l} + \delta k_{+l}}{\sqrt{3}} = \frac{2\sqrt{3}}{3}\left(\delta k_0 + \frac{D_2}{2} l^2\right), \qquad (3.9)$$

and the corresponding pump mode power is

$$\left|a_0\right|^2_{\mathrm{MI,max}} = \frac{\delta k_{-l} + \delta k_{+l}}{3\gamma} = \frac{2\delta k_0 + D_2 l^2}{3\gamma}. \qquad (3.10)$$

In the case of nearly zero dispersion, we plot the MI region where the MI gain exceeds the cavity loss rate as a function of δk_0 and $|a_0|^2$ in Fig. 3.2, where $|a_0|^2$ is normalized to the threshold of pump laser power for MI generation. The cusp of the MI region represents the case where the maximum MI gain equals the cavity loss.

$$\delta k_0 = \frac{\sqrt{3}}{2}\alpha - \frac{D_2}{2} l^2. \qquad (3.11)$$

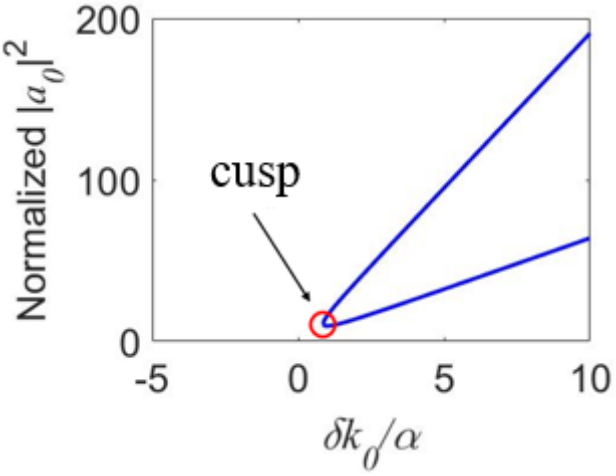

Fig. 3.2 MI region of a single microcavity with nearly zero dispersion.

3.1.2 MI generation in red-detuned regime only

From Fig. 3.2, the MI region in a single microcavity exists only in the red-detuned side ($\delta k_0 > 0$). In this Subsection, we discuss the reason MI is triggered only in the red-detuned region in a single microcavity.

Below the MI generation threshold, only the pump mode propagates in the microcavity. The pump mode a_0 obeys Eq. (2.4) as

$$\frac{\partial a_0}{\partial z} = -i\delta k_0 a_0 - \frac{\alpha}{2} a_0 + i\gamma \left|a_0\right|^2 a_0 + i\sqrt{\theta} F. \tag{3.12}$$

At steady state, the phase accumulation of the pump mode in one roundtrip is

$$\phi = -\delta k_0 L + \gamma L_{\text{eff}} \left|a_0\right|^2, \tag{3.13}$$

where $L_{\text{eff}} = (1\text{-}e^{-\alpha L})/\alpha$ is the effective nonlinear length [85]. The resonance condition of the microcavity requires $\phi = 0$. Thus, the pump mode wave vector detuning δk_0 has to be red-detuned to fulfill the resonance condition. The inclusion of Kerr effect effectively red shifts the cavity resonance. If the pump laser is initially blue-detuned with respect to the cold cavity wave vector as shown in Fig. 3.3(a), when the

microcavity is pumped and the Kerr effect is included, the pump laser wave vector will move away from the cavity resonance as shown in Fig. 3.3(b). As a result, a blue-detuned pump cannot couple enough light into the microcavity to trigger MI generation.

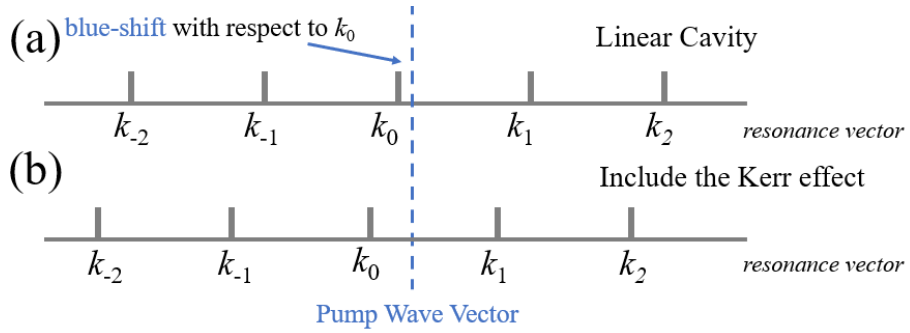

Fig. 3.3 (a) The laser wave vector and cavity resonances for a blue-detuned pump in a linear cavity; (b) The cavity resonances when the microcavity is pumped and Kerr effect is included.

3.2 MI region in coupled microcavity system

In this Section, we study how the MI region of the main cavity is affected by the coupling with an auxiliary cavity.

3.2.1 The MI region in the main cavity

The MI region of the main cavity is determined as follows. We assume the energy of the cw pump laser is coupled to the nearest cavity mode of the main cavity (pump mode) with mode number $\mu = 0$. We look for the condition that the 0-th mode of the main cavity acts as a pump to excite neighboring side modes in the main cavity through MI. We do so by investigating the linear stability of the side modes of the main cavity with $\mu = \pm l$, where l is the mode number of the first excited side mode. Note that in the auxiliary cavity, the mode $\mu' = 0$ is excited by the coupling to the mode with $\mu = 0$ in the main cavity. For simplicity we assume that the auxiliary cavity is linear, therefore

the 0-th mode of the auxiliary cavity will not excite the side modes of the mode $\mu' \neq 0$ in the auxiliary cavity. The side modes in the auxiliary cavity however will be excited by the coupling to the corresponding side modes of the main cavity.

We first determine the relation between the external cw pump laser power and the pump mode power. When the side modes are not excited in both the main and auxiliary cavities, the cw pump is only coupled to the 0-th modes, i.e., only the pump modes are oscillating in both the cavities. From Eqs. (2.10) and (2.11), we have

$$\frac{\partial a_0}{\partial z} = -i\delta k_0 a_0 - \frac{\alpha}{2} a_0 + i\gamma \left|a_0\right|^2 a_0 + i\sqrt{\theta_c}\, a_0' + i\sqrt{\theta} F, \tag{3.14}$$

$$\frac{\partial a_0'}{\partial z} = -i\delta k_0' a_0' - \frac{\alpha'}{2} a_0' + i\sqrt{\theta_c}\, a_0. \tag{3.15}$$

In steady state, i. e., $\partial a_0/\partial z = 0$ and $\partial a'_0/\partial z = 0$, the relation between the pump mode power $|a_0|^2$ and the cw pump power $|F|^2$ in the main cavity is given by

$$\theta\left|F\right|^2 = \left[\left(-\frac{\alpha}{2} - \frac{\frac{\alpha'}{2}\theta_c}{\delta k_0'^2 + \frac{\alpha'^2}{4}}\right)^2 + \left(\gamma\left|a_0\right|^2 - \delta k_0 + \frac{\delta k_0' \theta_c}{\delta k_0'^2 + \frac{\alpha'^2}{4}}\right)^2\right]\left|a_0\right|^2. \tag{3.16}$$

Eq. (3.16) is a cubic equation relating $|a_0|^2$ and $|F|^2$.

In the main cavity, we determine the stability of the trivial solutions of the $\pm l$ modes $a_{\pm l} = 0$ by perturbing the mode with small fluctuations $\delta a_{\pm l}$. The corresponding perturbations of the auxiliary cavity are $\delta a'_{\pm l'}$. The boundary of the MI region is defined by the threshold parameters at which the perturbations grow. In the stability analysis, only the 0-th modes and the particular perturbated modes are oscillating in the main

and auxiliary cavities. From Eqs. (2.10) and (2.11), the side mode perturbations $\delta a_{\pm l}$ and $\delta a'_{\pm l'}$ obey

$$\frac{\partial \delta a_{+l}}{\partial z} = -i\delta k_{+l}\delta a_{+l} - \frac{\alpha}{2}\delta a_{+l} + i\gamma\left(a_0^2\delta a_{-l}^* + 2\left|a_0^2\right|\delta a_{+l}\right) + i\sqrt{\theta_c}\delta a'_{+l'}, \tag{3.17}$$

$$\frac{\partial \delta a_{-l}^*}{\partial z} = i\delta k_{-l}\delta a_{-l}^* - \frac{\alpha}{2}\delta a_{-l}^* - i\gamma\left(a_0^{*2}\delta a_{+l} + 2\left|a_0^2\right|\delta a_{-l}^*\right) - i\sqrt{\theta_c}\delta a'^*_{-l'}, \tag{3.18}$$

$$\frac{\partial \delta a'_{+l'}}{\partial z} = -i\delta k'_{+l'}\delta a'_{+l'} - \frac{\alpha'}{2}\delta a'_{+l'} + i\sqrt{\theta_c}\delta a_{+l}, \tag{3.19}$$

$$\frac{\partial \delta a'^*_{-l'}}{\partial z} = i\delta k'_{-l'}\delta a'^*_{-l'} - \frac{\alpha'}{2}\delta a'^*_{-l'} - i\sqrt{\theta_c}\delta a_{-l}^*. \tag{3.20}$$

Eqs. (3.17)-(3.20) can be rewritten as

$$\begin{bmatrix} \frac{\partial \delta a_{+l}}{\partial z} \\ \frac{\partial \delta a_{-l}^*}{\partial z} \\ \frac{\partial \delta a'_{+l'}}{\partial z} \\ \frac{\partial \delta a'^*_{-l'}}{\partial z} \end{bmatrix} = \begin{bmatrix} -i\delta k_{+l} + i2\gamma\left|a_0^2\right| - \frac{\alpha}{2} & i\gamma a_0^2 & i\sqrt{\theta_c} & 0 \\ -i\gamma a_0^{*2} & i\delta k_{-l} - i2\gamma\left|a_0^2\right| - \frac{\alpha}{2} & 0 & -i\sqrt{\theta_c} \\ i\sqrt{\theta_c} & 0 & -i\delta k'_{+l'} - \frac{\alpha'}{2} & 0 \\ 0 & -i\sqrt{\theta_c} & 0 & i\delta k'_{-l'} - \frac{\alpha'}{2} \end{bmatrix} \begin{bmatrix} \delta a_{+l} \\ \delta a_{-l}^* \\ \delta a'_{+l'} \\ \delta a'^*_{-l'} \end{bmatrix}. \tag{3.21}$$

The MI is generated when at least one of the eigenvalues λ of the secular equation shown in Eq. (3.22) has a positive real part. The secular equation is a quartic equation with respect to the eigenvalue λ and the parameters are $\delta k_{\pm l}$, $\delta k'_{\pm l'}$ and the pump mode power $|a_0|^2$. We numerically solve the quartic equation to determine the MI region, which is a function of the pump laser wave vector detuning δk_0 and pump mode power $|a_0|^2$.

$$\begin{bmatrix} -i\delta k_{+l} + i2\gamma\left|a_0^2\right| - \frac{\alpha}{2} - \lambda & i\gamma a_0^2 & i\sqrt{\theta_c} & 0 \\ -i\gamma a_0^{*2} & i\delta k_{-l} - i2\gamma\left|a_0^2\right| - \frac{\alpha}{2} - \lambda & 0 & -i\sqrt{\theta_c} \\ i\sqrt{\theta_c} & 0 & -i\delta k'_{+l'} - \frac{\alpha'}{2} - \lambda & 0 \\ 0 & -i\sqrt{\theta_c} & 0 & i\delta k'_{-l'} - \frac{\alpha'}{2} - \lambda \end{bmatrix} = 0 \quad (3.22)$$

3.2.2 The effect of coupling coefficient θ_c on the MI region

To investigate the dependence of the MI region of the main cavity on the coupling coefficient, we assume the coupled microcavities are identical except for the Kerr nonlinearity, thus the two microcavities have the same parameters save the Kerr coefficient. In this Subsection, the loss of the main cavity is fixed and we neglect the cavity dispersion and detuning between the resonances of the two cavities.

Coupling induced blue-detuned MI region

The MI region obtained from Eq. (3.22) is mainly determined by the coupling coefficient between the cavities θ_c. Figs. 3.4(a) and 3.4(b) show the MI region with $\sqrt{\theta_c} = 0.1\alpha$ and $\sqrt{\theta_c} = 3.5\alpha$, respectively. When the coupling coefficient is small, MI occurs in the red-detuned region only (the same as in a single microcavity). When $\sqrt{\theta_c}$ increases, a new MI region emerges in the blue-detuned side as shown in Fig. 3.4(b). We define the smallest and largest detuning values of the blue-detuned MI region as the left detuning boundary (LB) and right detuning boundary (RB), respectively. The pump laser power is an important parameter in experiments. The relationship between

the pump mode power in the main cavity $|a_0|^2$ and the cw pump laser power $|F|^2$ is given in Eq. (3.16). Fig. 3.4(c) shows the blue-detuned MI region as a function of the pump laser detuning and pump mode power with $\sqrt{\theta_c}$ = 3.5α and 3.8α. We note that when $\sqrt{\theta_c}$ increases, the MI region expands both in the detuning range and pump power. In experiments, the detuning range and the minimum pump power for MI generation are important parameters. We define the separation between the LB and the RB as the detuning range and the lowest cw pump laser power we can get in MI region at the minimum cw pump laser power. Fig. 3.4(c) shows the LB's, RB's and the locations of the minimum pump powers.

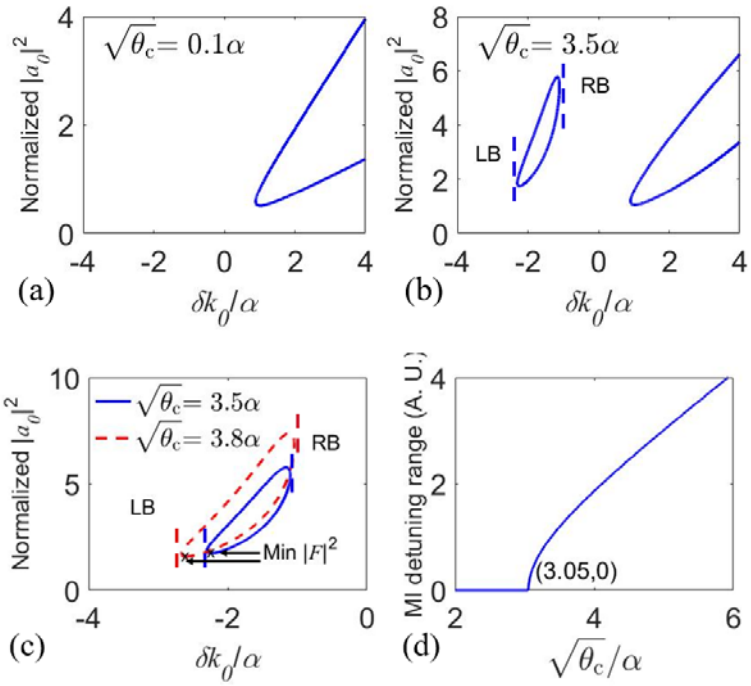

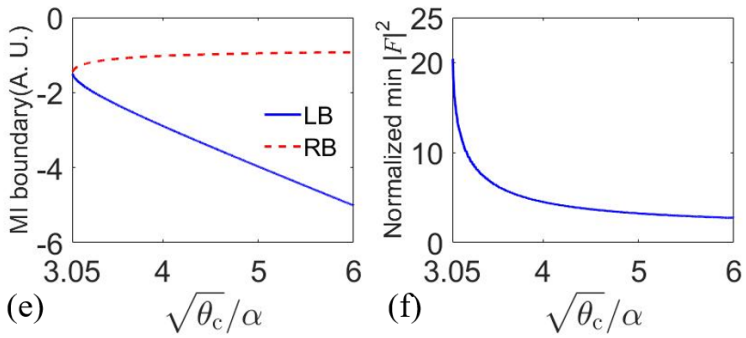

Fig. 3.4 The MI region as a function of the pump detuning and the normalized intracavity pump mode power with (a) $\sqrt{\theta_c} = 0.1\alpha$ and (b) $\sqrt{\theta_c} = 3.5\alpha$. The blue-detuned MI region as a function of the pump detuning and normalized pump laser power with (c) $\sqrt{\theta_c} = 3.5\alpha$ (blue solid lines) and $\sqrt{\theta_c} = 3.8\alpha$ (red dashed lines). Evolution of the normalized (d) MI detuning range, (e) left MI boundary (LB) and right MI boundary (RB), and (f) the minimum pump laser power as a function of $\sqrt{\theta_c}$.

Figs. 3.4(d), 3.4(e), and 3.4(f) show the evolution of the detuning range, LB and RB, and the lowest pump laser power, respectively, in the MI region as a function of $\sqrt{\theta_c}$. From Fig. 3.4(d), the MI detuning range is zero when $\sqrt{\theta_c}$ is below a threshold value (~3.05α) and increases quasi-linearly with $\sqrt{\theta_c}$. Thus, the blue-detuned MI region requires sufficiently strong coupling between the two microcavities to exist. Fig. 3.4(e) gives the locations of the LB (blue solid lines) and RB (red dashed lines) of the blue-detuned MI region as a function of $\sqrt{\theta_c}$. When $\sqrt{\theta_c}$ increases, the LB of the MI region is blue-shifted while the RB of the MI region is red-shifted. The MI detuning range is therefore broadened. When $\sqrt{\theta_c}$ increases from 3.05α to 6α, the LB moves about 7 times that of the RB. The broadening of the MI detuning range is therefore mainly contributed by the blue shift of the LB. Fig. 3.4(f) shows the evolution of the minimum pump laser power as a function of $\sqrt{\theta_c}$. The minimum pump power first decreases rapidly and then more gradually. In summary, the new blue-detuned MI region is induced by the coupling between the two microcavities, which will emerge

only after a threshold $\sqrt{\theta_c}$ is reached, and the stronger the coupling the larger the MI region.

Qualitative explanation for the blue-detuned MI region

The coupling of the auxiliary cavity creates a new blue-detuned MI region in the main cavity. We note that while light in the main cavity is coupled into the auxiliary cavity, light in the auxiliary cavity is also coupled back into the main cavity. Thus, the main cavity can be regarded as being pumped by both the external cw laser and the auxiliary cavity.

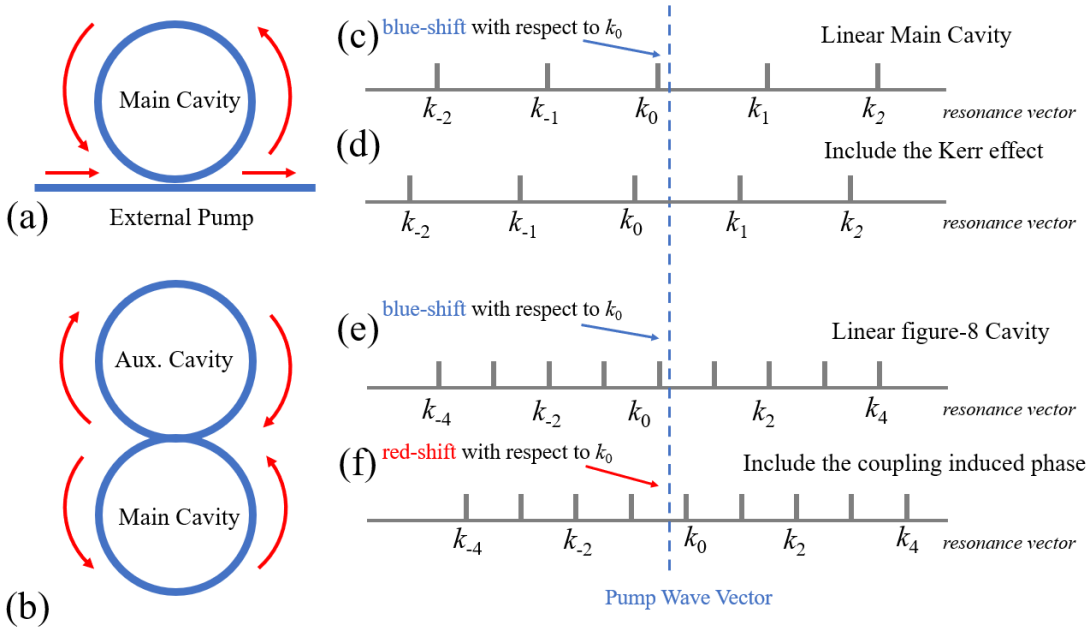

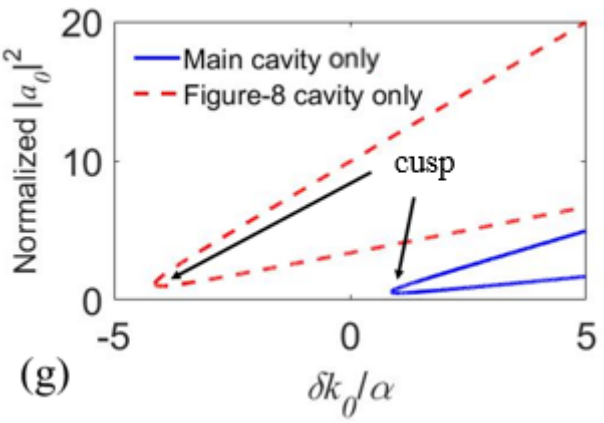

Fig. 3.5 (a) The optical path when light only propagates in the main cavity. (b) The figure-8 optical path when light propagates in both the main and auxiliary cavities. (c) The cavity resonances of a linear main cavity. The external cw pump (blue dashed line) is blue-detuned with respect to the nearest resonance wave vector; (d) The resonance wave vectors of the blue-detuned pumped main cavity with Kerr effect. (e) The resonances of the figure-8 cavity with twice the cavity length of the main cavity, which align with that of the linear main cavity but the corresponding D_1 is half. (f) The resonances of the figure-8 cavity including the coupling induced π phase shift. (g) The MI regions of the main cavity (Fig. 3.5(a)) is pumped by only the external cw light (blue solid lines) and a single figure-8 cavity (Fig. 3.5(b)) with the π phase shift pumped only by the light returning from the auxiliary cavity (red dashed lines).

As shown in Fig. 3.5, the light coupled into the main cavity from the external cw pump may propagate through either the main cavity in a circular path (Fig. 3.5(a)) or both the main and auxiliary cavities in a figure-8 path (Fig. 3.5(b)). The length of the figure-8 cavity is twice that of the main cavity as the auxiliary cavity is assumed to be identical to the main cavity. For the additional figure-8 cavity, the mode wave vector spacing D_1 is half of that of the main cavity because its length is doubled as shown in Fig. 3.5(e). Since the coupling between the two microcavities introduces an additional π phase shift to the optical path of the figure-8 cavity, the resonance wavevectors of the figure-8 cavity are blue-shifted by $D_1/4$ as shown in Fig. 3.5(f). From Figs. 3.5(f) and 3.5(c), the cw pump (blue dashed line) is blue-detuned with respect to the nearest resonance wave vector of the main cavity but red-detuned with respect to that of the

figure-8 cavity. As a result, it is possible to generate MI in the main cavity by the light returned from the auxiliary cavity while the external cw pump is still in the blue-detuned region of the main cavity. Fig. 3.5(g) shows the numerically determined MI regions when only one of the optical paths is considered. First, we consider only the main cavity (Fig. 3.5(a)) is pumped by only the external cw light (blue solid lines in Fig. 3.5(g)). Then we consider a single figure-8 cavity (Fig. 3.5(b)) with the π phase shift pumped only by the light returning from the auxiliary cavity (red dashed lines in Fig. 3.5(g))). From Fig. 3.5(g), the external pump only supports MI generation in the red-detuned side of the main cavity but part of the MI region from light returning from the auxiliary cavity is in the blue-detuned side of the main cavity. The MI region of the coupled microcavities is related to, but not a linear combination the two MI regions shown in Fig 3.5(g), as MI is a nonlinear effect.

3.2.3 Coupled microcavity system in steady state

Steady state calculation

Besides the qualitative explanation, in this Subsection, we determine the blue-detuned MI region of the coupled microcavity system in steady state. Here we assume the auxiliary cavity is in steady state first and study the dynamics of the main cavity. Although this assumption is not realistic, it allows us to analytically determine the MI region. The analytically determined MI region will be compared to that determined numerically in Section 3.2.1

In steady state, we have $\partial a'_{\mu'}/\partial z = 0$. Substitution into Eq. (2.11) gives

$$a_{\mu'}{}' = \frac{i\sqrt{\theta_c}}{i\delta k_{\mu'}{}' + \frac{\alpha'}{2}} a_\mu. \tag{3.23}$$

Substitution of Eq. (3.23) into Eq. (2.10), we have

$$\frac{\partial a_\mu}{\partial z} = -i\left(\delta k_\mu - \frac{\delta k_{\mu'}{}'\theta_c}{\delta k_{\mu'}{}'^2 + \frac{\alpha'^2}{4}}\right)a_\mu - \left(\frac{\alpha}{2} + \frac{\theta_c\alpha'}{2\delta k_{\mu'}{}'^2 + \frac{\alpha'^2}{2}}\right)a_\mu + i\gamma\sum_{\mu_1,\mu_2,\mu_3} a_{\mu 1}a_{\mu 2}a_{\mu 3}{}^* + i\delta_{\mu 0}\sqrt{\theta}F \tag{3.24}$$

If we introduce the effective wave vector detuning $\delta k_{\mu,\text{eff}}$ and effective cavity loss rate α_{eff} as

$$\delta k_{\mu,\text{eff}} = \delta k_\mu - \frac{\delta k_{\mu'}{}'\theta_c}{\delta k_{\mu'}{}'^2 + \frac{\alpha'^2}{4}}, \tag{3.25}$$

$$\alpha_{\text{eff}} = \alpha + \frac{\theta_c\alpha'}{\delta k_{\mu'}{}'^2 + \frac{\alpha'^2}{4}}, \tag{3.26}$$

Eq. (3.24) can be rewritten as

$$\frac{\partial a_\mu}{\partial z} = -i\delta k_{\mu,\text{eff}}a_\mu - \frac{\alpha_{\text{eff}}}{2}a_\mu + i\gamma\sum_{\mu_1,\mu_2,\mu_3} a_{\mu 1}a_{\mu 2}a_{\mu 3}{}^* + i\delta_{\mu 0}\sqrt{\theta}F. \tag{3.27}$$

Eq. (3.27) has the same form of the CMEs model for a single microcavity as shown in Eq. (2.4). That means, in steady state, we can consider the coupled microcavity system as a single microcavity where the wave vector detuning and cavity loss are modified by the inclusion of auxiliary cavity as shown in Eqs. (3.25) and (3.26). Thus, we can use the results in Section 3.1.1 to determine the MI region of a coupled microcavity system. From Eq. (3.7), the MI gain of the $a_{\pm l}$ modes in the main cavity are

$$G_{\text{MI}} = \sqrt{-\left(\delta k_{-l,\text{eff}} + \delta k_{+l,\text{eff}}\right)^2 + 8\left(\delta k_{-l,\text{eff}} + \delta k_{+l,\text{eff}}\right)\gamma\left|a_0\right|^2 - 12\gamma^2\left|a_0\right|^4}. \tag{3.28}$$

For a fixed pump laser wave vector, the maximum MI gain is

$$G_{\mathrm{MI,max}} = \frac{\delta k_{-l,\mathrm{eff}} + \delta k_{+l,\mathrm{eff}}}{\sqrt{3}}. \tag{3.29}$$

The corresponding main cavity pump mode power is

$$\left|a_0\right|^2_{\mathrm{MI,max}} = \frac{\delta k_{-l,\mathrm{eff}} + \delta k_{+l,\mathrm{eff}}}{3\gamma}. \tag{3.30}$$

If we defined the wave vector detuning between the 0-th modes of the main cavity and the auxiliary cavity as

$$\Delta k_0 = \delta k_0 - \delta k_0', \tag{3.31}$$

we have

$$\delta k_{-l,\mathrm{eff}} + \delta k_{+l,\mathrm{eff}} = 2\delta k_0 + D_2 l^2 - \frac{2\theta_c\left(\delta k_0 - \Delta k_0 + \frac{D_2'}{2} l'^2\right)}{\left(\delta k_0 - \Delta k_0 + \frac{D_2'}{2} l'^2\right)^2 + \frac{\alpha'^2}{4}}. \tag{3.32}$$

The maximum MI gain for a particular main cavity wave vector detuning value is

$$G_{\mathrm{MI,max}} = \frac{2}{\sqrt{3}}\left[\delta k_0 + \frac{D_2}{2} l^2 - \frac{\theta_{\mathrm{c}}\left(\delta k_0 - \Delta k_0 + \frac{D_2'}{2} l'^2\right)}{\left(\delta k_0 - \Delta k_0 + \frac{D_2'}{2} l'^2\right)^2 + \frac{\alpha'^2}{4}}\right]. \tag{3.33}$$

The boundaries of the MI region can be calculated by solving Eq. (3.34) where the maximum MI gain equals the effective cavity loss rate,

$$\frac{2}{\sqrt{3}}\left[\delta k_0 + \frac{D_2}{2} l^2 - \frac{\theta_{\mathrm{c}}\left(\delta k_0 - \Delta k_0 + \frac{D_2'}{2} l'^2\right)}{\left(\delta k_0 - \Delta k_0 + \frac{D_2'}{2} l'^2\right)^2 + \frac{\alpha'^2}{4}}\right] = \alpha + \frac{\theta_{\mathrm{c}}\alpha'}{\left(\delta k_0 - \Delta k_0 + \frac{D_2'}{2} l'^2\right)^2 + \frac{\alpha'^2}{4}}. \tag{3.34}$$

If we introduce the variables

$$S_{l'} = \Delta k_0 - \frac{D_2'}{2} l'^2 \text{ and } r_l = \frac{\sqrt{3}}{2}\alpha - \frac{D_2}{2} l^2, \tag{3.35}$$

Eq. (3.34) can be rewritten as

$$\delta k_0^{\,3} + \left(-2S_{l'} - r_l\right)\delta k_0^{\,2} + \left(S_{l'}^{\,2} + \frac{\alpha'^2}{4} - \theta_c + 2S_{l'} r_l\right)\delta k_0 - r_l\left(S_{l'}^{\,2} + \frac{\alpha'^2}{4}\right) + \theta_c\left(S_{l'} - \frac{\sqrt{3}}{2}\alpha'\right) = 0. \tag{3.36}$$

We note that $S_{l'}$ represents the detuning between mode $a_{\pm l}$ and $a'_{\pm l'}$ in the absence of main cavity dispersion, and r_l is the detuning value of the cusp of the MI region in a single microcavity.

Eq. (3.36) is a cubic equation of δk_0 and it can have one, two or three different real roots. When there are three different real roots, the three roots correspond to the three extrema of the blue-detuned and red-detuned MI regions as shown in Fig. 3.6.

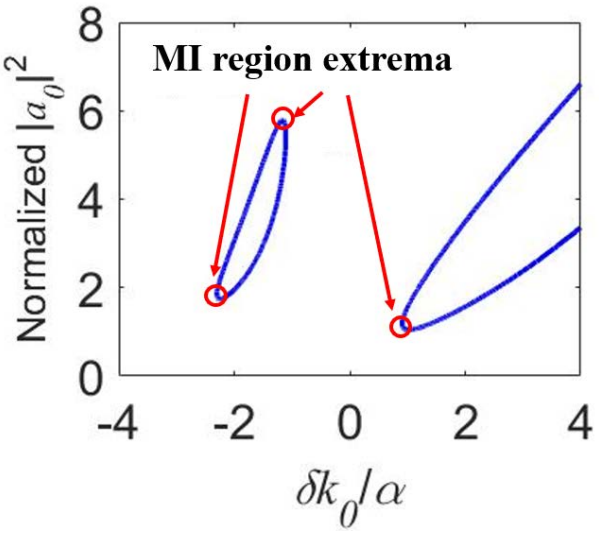

Fig. 3.6 Three extrema of blue-detuned and red-detuned MI regions.

Thus, the blue-detuned MI region exists when the discriminant of Eq. (3.36) satisfies

$$\Delta = \left(\frac{q}{2}\right)^2 + \left(\frac{p}{3}\right)^3 < 0, \tag{3.37}$$

where

$$p = \frac{-4{S_{l'}}^2 + 3\alpha'^2 - 12\theta_c + 8S_{l'}r_l - 4r_l^2}{12}, \tag{3.38}$$

$$q = -\frac{\sqrt{3}}{2}\alpha'\theta_c + \frac{\left(S_{l'} - r_l\right)\left(4{S_{l'}}^2 + 4r_l^2 + 16r_l S_{l'} + 9\alpha'^2 + 18\theta_c\right)}{54}. \tag{3.39}$$

If the blue-detuned MI region exists, by solving Eq. (3.36), the boundaries of the blue-detuned MI region are given by

$$\begin{aligned} &\frac{2\sqrt{3}}{3}\sqrt{-p}\cos\left[\frac{1}{3}\arccos\left(-\frac{3\sqrt{3}q}{2\sqrt{-p^3}}\right)+\frac{2}{3}\pi\right]+\frac{2S_{l'}+r_l}{3}, \text{ and} \\ &\frac{2\sqrt{3}}{3}\sqrt{-p}\cos\left[\frac{1}{3}\arccos\left(-\frac{3\sqrt{3}q}{2\sqrt{-p^3}}\right)+\frac{4}{3}\pi\right]+\frac{2S_{l'}+r_l}{3}. \end{aligned} \tag{3.40}$$

Thus, the MI detuning range is given by the absolute values of the difference of the two boundaries as

$$\left|2\sqrt{-p}\sin\left[\frac{1}{3}\arccos\left(-\frac{3\sqrt{3}q}{2\sqrt{-p^3}}\right)\right]\right|. \tag{3.41}$$

The minimum main cavity pump mode power is

$$\frac{2}{3\gamma}\left[\delta k_0 + \frac{D_2}{2}l^2 - \frac{\theta_c\left(\delta k_0 - S_{l'}\right)}{\left(\delta k_0 - S_{l'}\right)^2 + \frac{\alpha'^2}{4}}\right]. \tag{3.42}$$

The effect of coupling coefficient

Here we analyze the blue-detuned MI region with different coupling coefficients and compare the results with Section 3.2.2.

In the case of two identical cavities except the Kerr nonlinearity, we have $S_{l'} = 0$, $r_l = \sqrt{3}\alpha/2$, $p = -\theta_c$, and $q = -2\sqrt{3}\alpha\theta_c/3 - \sqrt{3}\alpha^3/9$. From Eq. (3.37), the existence of blue-detuned MI region requires

$$\frac{1}{108} + \frac{\theta_c}{9\alpha^2} + \frac{\theta_c^2}{3\alpha^4} - \frac{\theta_c^3}{27\alpha^6} < 0. \tag{3.43}$$

Solving the inequation (3.43), the requirement of the coupling coefficient for the existence of MI region is $\sqrt{\theta_c}/\alpha > 3.0536$. The threshold value calculated with the SSC method corresponds well with the numerical result shown in Fig. 3.4(d).

Besides determining the threshold for the existence of blue-detuned MI region, we can also determine the MI regions analytically. Fig. 3.7 shows the numerically and analytically determined MI regions with different coupling coefficient θ_c. The parameters in Fig. 3.7(a) and 3.7(b) are the same as Fig. 3.4(a) and 3.4(b), respectively. In Fig. 3.7, the numerically and analytically determined MI region are denoted with blue solid line and red dashed line, respectively. The analytical and numerical results are in good agreement for determining the blue-detuned side MI region as shown in Fig. 3.7(b). The numerically and analytically determined red-detuned MI regions are different as shown in Fig. 3.7(a) and 3.7(b). As discussed in Section 3.2.2, we attribute the red-detuned MI region to the optical path of the main cavity. The steady state auxiliary cavity assumption (analytical method) treats the auxiliary cavity as a linear

filter providing additional phase shift and loss to all optical paths in the coupled microcavity system. However, the light traveling only in the main cavity does not see the filter function of the auxiliary cavity. Moreover, the light returning from the auxiliary cavity contributes to dynamics in the main cavity through the Kerr nonlinearity. Thus, the numerically and analytically determined red-detuned MI regions are different. If we adjust the phase shift and loss of the analytically determined red-detuned MI regions, they can cover a large part of the numerically determined red-detuned MI region as shown in Fig. 3.7(c) and 3.7(d).

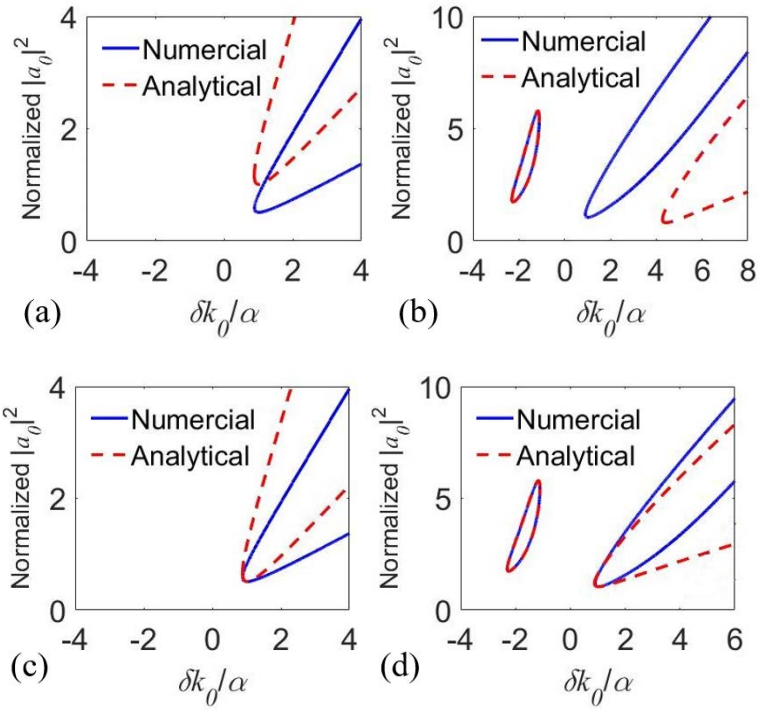

Fig. 3.7. Comparison of numerically (blue solid lines) and analytically (red dashed lines) determined MI regions. The parameters in (a) and (b) are the same as Fig. 3.4(a) and 3.4(b), respectively. (c) and (d) Analytically determined red-detuned MI regions can cover a large part of the numerically determined red-detuned MI regions with the adjustment of phase and loss. The parameters in (c) and (d) correspond to (a) and (b) respectively.

Fig. 3.8 shows the comparison of numerically and analytically determined blue-detuned MI regions. The parameters in Figs. 3.8(a), 3.8(d), 3.8(e), 3.8(f) correspond to the parameters in Fig. 3.4(c), 3.4(d), 3.4(e) and 3.4(f), respectively. Fig. 3.8(a) shows that the numerical and analytical results agree well for the blue-detuned MI region with different coupling coefficients. The numerical error of the numerically determined MI region depends on the step size chosen in the numerical simulations. We calculate the difference between the numerically and analytically determined $|a_0|^2$ in Fig. 3.8(a) with coupling coefficient $\sqrt{\theta_c} = 3.5\alpha$. The difference between the results of the two methods is always smaller than the numerical error, no matter when the step size is 0.01 or 0.001 as shown in Figs. 3.8(b) and 3.8(c), respectively. As discussed in Section 3.2.2, the blue-detuned MI region originates from the figure-8 optical path. The numerically and analytically determined blue-detuned MI regions are in good agreement because in the figure-8 optical path, the auxiliary cavity functions as a linear filter providing phase shift and loss.

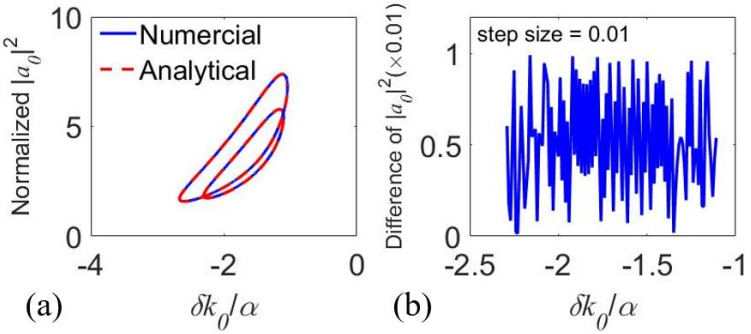

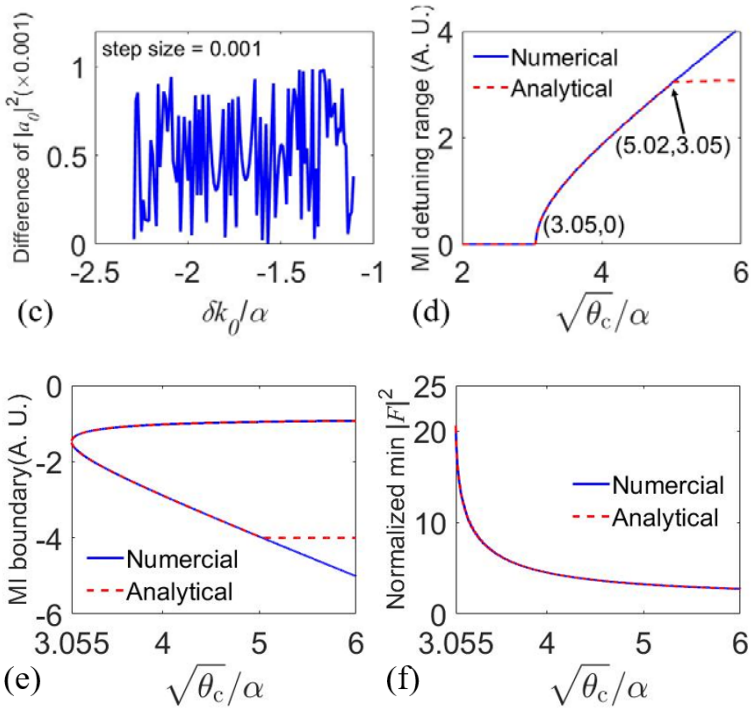

Fig. 3.8 Comparison between the numerically and analytically determined blue-detuned MI regions. The parameter in (a), (d), (e), (f) are the same as Fig. 3.4(c), 3.4(d), 3.4(e) and 3.4(f), respectively. Difference of numerically and analytically determined $|a_0|^2$ with step size of (b) 0.01 and (c) 0.001.

Fig. 3.8(d) presents the numerically and analytically determined the variation of the MI detuning range with coupling coefficient. The two results agree well when the coupling coefficient $\sqrt{\theta_c}/\alpha < 5.02$. When the coupling coefficient exceeds this threshold, the analytical results deviate from the numerical results. As discussed before, the analytical method assumes that the auxiliary cavity goes to steady state first. This assumption is reasonable when the optical power is mainly in the main cavity, i.e., the coupling coefficient between the two cavities is small. The assumption is not appliable when the optical power inside the auxiliary cavity becomes large. In such cases, the evolution of the two cavities should be considered together. Fig. 3.8(e) presents the numerical and analytical results of MI boundaries versus the coupling coefficient. The

two methods agree well for depicting the RB evolution while the analytically determined LB evolution deviates from the numerical results when the coupling coefficient $\sqrt{\theta_c}/\alpha > 5.02$. In Fig. 3.8(f), the numerical and analytical results correspond well for determining the dependence of the minimum pump power $|F|^2$ evolution on coupling coefficient θ_c.

3.2.4 The effect of the auxiliary parameters on the blue-detuned MI region

The blue-detuned MI region of the main cavity is mainly determined by the auxiliary cavity loss α' and the coupling modes detuning $S_{l'}$. In this Subsection, we discuss how these two parameters affect the blue-detuned MI region.

Effect of auxiliary cavity loss α′

In experiments, the loss rates of the two cavities of a coupled microcavity system can be different. Here we discuss how the blue-detuned MI region is affected by the loss in the auxiliary cavity. In the following discussion, we neglect the group velocity dispersion and assume the detuning between the resonances of the two cavities is zero.

We first use the analytical method introduced in Section 3.2.3 to determine the blue-detuned MI region. In Figs. 3.9(a)-3.9(d), the coupling coefficient between the two cavities is $\sqrt{\theta_c} = 3.5\alpha$. Fig. 3.9(a) shows the blue-detuned MI regions with auxiliary cavity loss α' = 0.9α, 1.0α and 1.1α. We note that when the auxiliary cavity loss increases, the MI region shrinks. The detuning range narrows and the minimum pump

laser power increases. Fig. 3.9(b) plots the MI detuning range as a function of α'/α. The MI detuning range decreases when the auxiliary cavity loss increases and vanishes when $\alpha' > 1.18\alpha$. Fig. 3.9(c) shows the change of the LB (red dashed line) and RB (blue solid line). The decrease of the MI detuning range is due to the red-shift of LB and blue-shift of the RB. When α' increases from 0.1α to 1.18α, the LB red-shifts from -3.04α to -1.72α and the RB blue-shifts from -0.1α to -1.72α. Thus, the shift of the RB is about 1.23 times that of the LB. The RB will approach the main cavity resonance as α' decreases, but it will not reach zero detuning even when $\alpha' = 0$. Fig. 3.9(d) presents the evolution of the minimum pump laser power as a function of α'. The minimum pump power is nearly zero when the auxiliary cavity loss is small, and increases rapidly when the auxiliary cavity loss increases. The curve in Fig. 3.9(d) terminates at $\alpha' = 1.18\alpha$ as the blue-detuned MI region vanishes when $\alpha' > 1.18\alpha$.

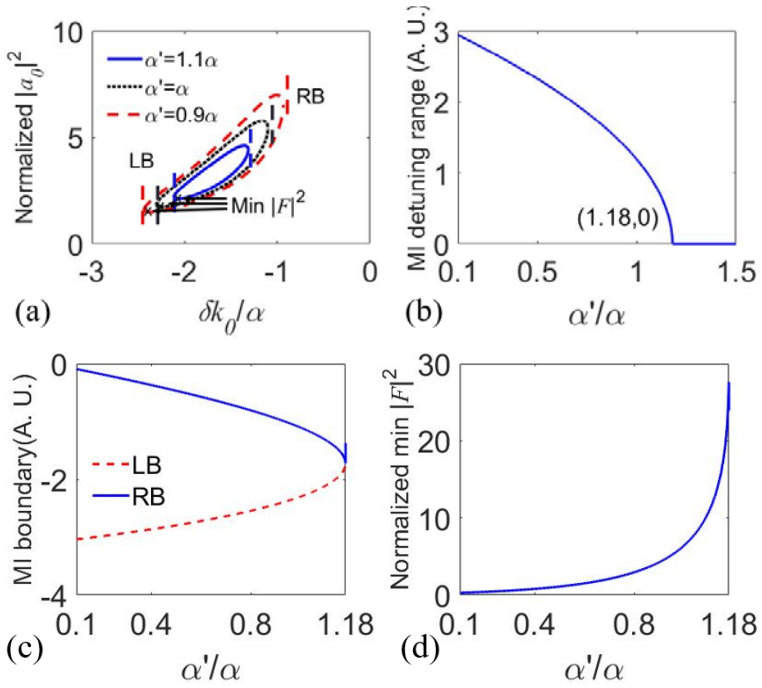

Fig. 3.9 The blue-detuned MI region as a function of the pump detuning and normalized pump mode power for (a) $\alpha' = 0.9\alpha$, 1.0α and 1.1α. Evolution of the (b) MI detuning range, (c) LB (red dashed line) and RB (blue solid line), and (d) normalized minimum pump laser power as a function of α'.

We also use the numerical method to determine the MI region with Eq. (3.22). The numerically and analytically determined MI regions are shown in Fig. 3.10 with blue solid line and red dashed line, respectively. The parameters used in Fig. 3.10 are the same as the parameters in Fig. 3.9. The numerical results agree well with the analytical results for determining MI regions with different auxiliary cavity loss α'.

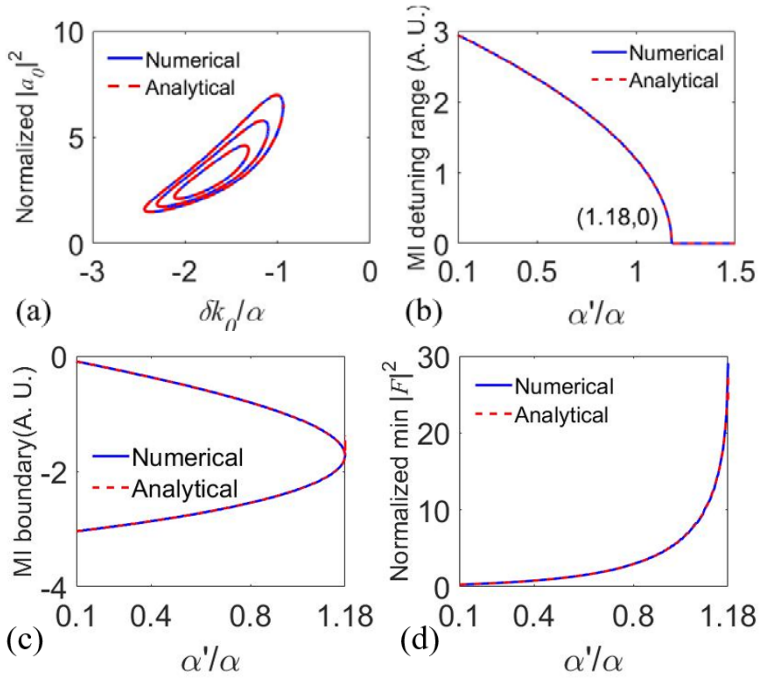

Fig. 3.10 Comparison between the numerically and analytically determined MI regions with different auxiliary cavity loss α'. The numerical and analytical results are denoted with blue solid and red dashed lines, respectively. The parameters of (a)-(d) are the same as Fig. 3.9(a)-3.9(d).

We then study the dependence of the MI detuning range and the minimum pump laser power for different values of α' and $\sqrt{\theta_c}$. Figs. 3.11(a) and 3.11(b) show the analytical results. In Fig. 3.11(a), the color bar represents the value of the MI detuning range. We note that the deep blue region in the lower right corner represents the parameter regime in which there is no MI. The edge of the deep blue region indicates the threshold value of $\sqrt{\theta_c}$ for the existence of blue-detuned MI area as a function of α'. The threshold value of $\sqrt{\theta_c}$ for the blue-detuned MI region decreases when α' decreases. From Fig. 3.11(a), for $\alpha' = 0.55\alpha$, the threshold value of $\sqrt{\theta_c}$ for the existence of the blue-detuned MI region is ~2α. Fig. 3.11(b) shows the minimum pump laser power for different α' and $\sqrt{\theta_c}$. The color bar represents minimum $|F|^2$. Again, the deep blue region in the lower right corner represents parameter regime in which there

is no MI. We observe that the minimum $|F|^2$ is small in the upper left corner. For a fixed $\sqrt{\theta_c}$, when α' increases the minimum pump laser power increases until α' reaches the threshold value beyond which no blue-detuned MI region exists as discussed in Fig. 3.9(d). For a fixed α', no blue-detuned MI region exists for small $\sqrt{\theta_c}$. After reaching the threshold $\sqrt{\theta_c}$ value, a high minimum pump laser power is required to achieve MI generation in the blue-detuned region. When $\sqrt{\theta_c}$ increases further, the minimum pump laser power decreases as shown in Fig. 3.4(f). Figs. 3.11(c) and 3.11(d) show the numerical results corresponding to Figs. 3.11(a) and 3.11(b), respectively. The numerical results agree well with the analytical results. The boundaries between the MI region and no MI region in the analytical figures are smooth lines while the boundaries in the numerical figures are step-like lines because of numerical discretization. Compared to analytical method, the numerical method is much more computationally demanding.

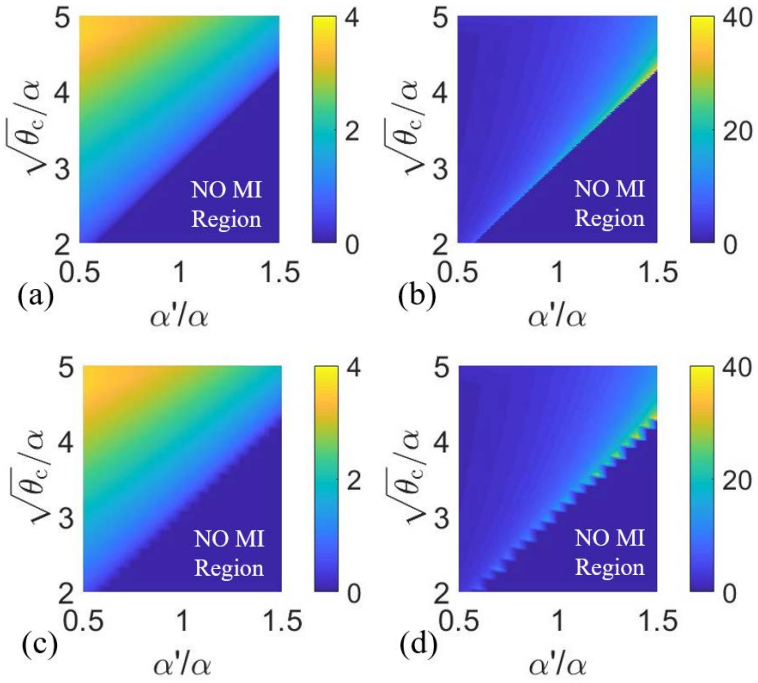

Fig. 3.11 The color plots of the analytically determined (a) blue-detuned MI detuning range and (b) minimum pump laser power; and numerically determined (c) blue-detuned MI detuning range and (d) minimum pump laser power for different $\sqrt{\theta_c}$ and α'.

Effects of detuning between the coupling modes in the auxiliary cavity

Main and auxiliary cavity having different size and/or dispersion will lead to the detuning between the coupling modes of the two cavities $S_{l'}$. In this Subsection, we study the effect of the detuning between the coupling modes in the auxiliary cavity. In the following discussion, the two cavities are assumed to have the same loss and we neglect the group velocity dispersion in the main cavity. The coupling coefficient between the two cavities is assumed to be 3.5α. We first analytically determine the blue-detuned MI region with the method introduced in Section 3.2.3.

Fig. 3.12(a) shows the blue-detuned MI region with $S_{l'}$ equals -0.5α, 0 and 0.5α. When $S_{l'}$ increases, the MI detuning range broadens and the minimum pump laser power decreases. Fig. 3.12(b) shows the variation of the MI detuning range as a function of $S_{l'}$.

We note that the blue-detuned MI region does not exist for $S_{l'} < -0.75\alpha$ and the MI detuning range increases from 0 to 2α when $S_{l'}$ increases from -0.75α to 0.95α. Fig. 3.12(c) plots the variation of the LB and RB versus $S_{l'}$. Both boundaries are red-shifted when $S_{l'}$ increases. The LB red-shifts from around -2.3α to -1.99α and the RB red-shifts from around -2.3α to 0 when $S_{l'}$ increases from -0.75α to 0.95α. Thus, the entire blue-detuned MI region is red-shifted when $S_{l'}$ increases. The MI detuning range is broadened because of the stronger red shift of the RB than that of the LB. Fig. 3.12(d) shows that the minimum pump laser power decreases when $S_{l'}$ increases. We note that the rate of decrease of the minimum pump laser power also decreases when $S_{l'}$ increases.

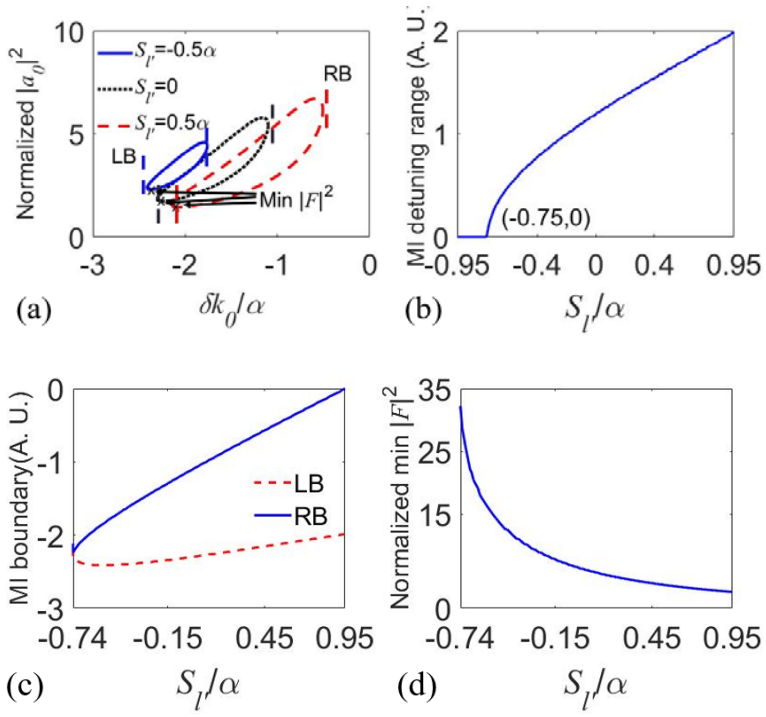

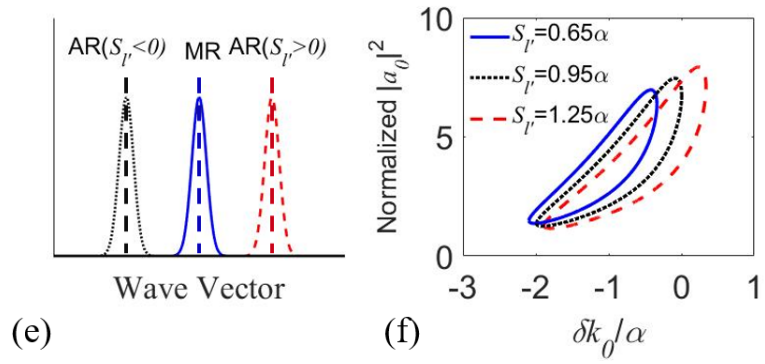

Fig. 3.12 The analytically determined blue-detuned MI region as a function of the pump detuning and normalized pump power with (a) $S_{I'} = -0.5\alpha$, 0 and 0.5α. The variation of the (b) MI detuning range, (c) left and right MI boundary, and (d) normalized minimum pump laser power as a function of $S_{I'}$. (e) The relative positions of the main cavity resonance (MCR) and auxiliary cavity resonance (ACR) with $S_{I'} < 0$ (black dotted lines) and $S_{I'} > 0$ (red dashed lines). (f) The initially blue-detuned MI region is shifted to the red-detuned side when $S_{I'}$ increases from 0.65α to 1.25α.

The observation in Figs. 3.12(a)-3.12(d) can be understood as follows. The detuning between the resonances of the two cavities $S_{I'}$ is the detuning of the cold cavities, i.e., there is no pump laser injection. The sign of $S_{I'}$ indicates the relative position of the two cavities' resonances. Fig. 3.12(e) shows the position of auxiliary cavity resonance (ACR) relative to the main cavity resonance (MCR) for both $S_{I'} < 0$ and $S_{I'} > 0$. With the injection of cw pump, the resonance of the main cavity is red shifted by the Kerr nonlinearity while the resonance of the auxiliary cavity is not affected. That adds an extra positive detuning between the main cavity and the auxiliary cavity. Note that the auxiliary cavity functions as a linear filter. When $S_{I'} < 0$, the red-shift of the main cavity moves the MCR away from the ACR. The effective coupling loss is therefore increased. Thus, the blue-detuned MI region shrinks. When the magnitude of detuning is sufficiently large, i.e., -0.75α, very little light is coupled from the main cavity to the auxiliary cavity. The coupled structure is reverted to a single

cavity system, and no blue-detuned MI region exists. When $S_{l'} > 0$, the red-shift of the main cavity moves the MCR toward the ACR. The effective coupling loss is decreased. Thus, the blue-detuned MI region expands. For large $S_{l'}$, part of the initially blue-detuned MI region is red-shifted to the red-detuned side. It should be noted that the blue-detuned MI region to the main cavity is in fact red-detuned to the figure-8 optical path. The results in Fig. 3.12 indicate that the resonances of the figure-8 optical path are also affected by the detuning of the coupling modes $S_{l'}$ between the two cavities. The shift of the figure-8 optical path resonances can be approximated from the MI region shifts.

Fig. 3.12(f) shows that at $S_{l'} = 0.65\alpha$, the blue-detuned MI region is entirely in the blue-detuned side. At $S_{l'} = 0.95\alpha$, the right boundary of the blue-detuned MI region is at the resonance of the main cavity. At $S_{l'} = 1.25\alpha$, the right boundary of the blue-detuned MI region crosses the zero detuning line and enters to the red-detuned side. For comparison, the MI region of a single microcavity, which is in the red-detuned side, can never reach zero detuning. Thus, the detuning range around zero detuning can be accessed by the MI region by properly choosing $S_{l'}$ in the coupled microcavity system. When $S_{l'}$ increases further, the initially blue-detuned MI region can be completely shifted into the red-detuned side and there is no MI in the blue-detuned region. The blue-detuned MI region originates from the red-detuned region of the figure-8 optical path. That indicates the resonances of the figure-8 optical path also shift to the red-detuned side of the main cavity resonances.

We compare the analytical results to the numerically determined MI regions in Fig. 3.13, where the numerical results and analytical results are denoted with blue solid lines and red dashed lines, respectively. Figs. 3.13(a)-3.13(d) correspond to the results in Figs. 3.12(a)-3.12(d) respectively and Fig. 3.13(e) corresponds to Fig. 3.12(f). The analytical results agree well with the numerical results for determining the figure-8 optical path induced blue-detuned MI regions.

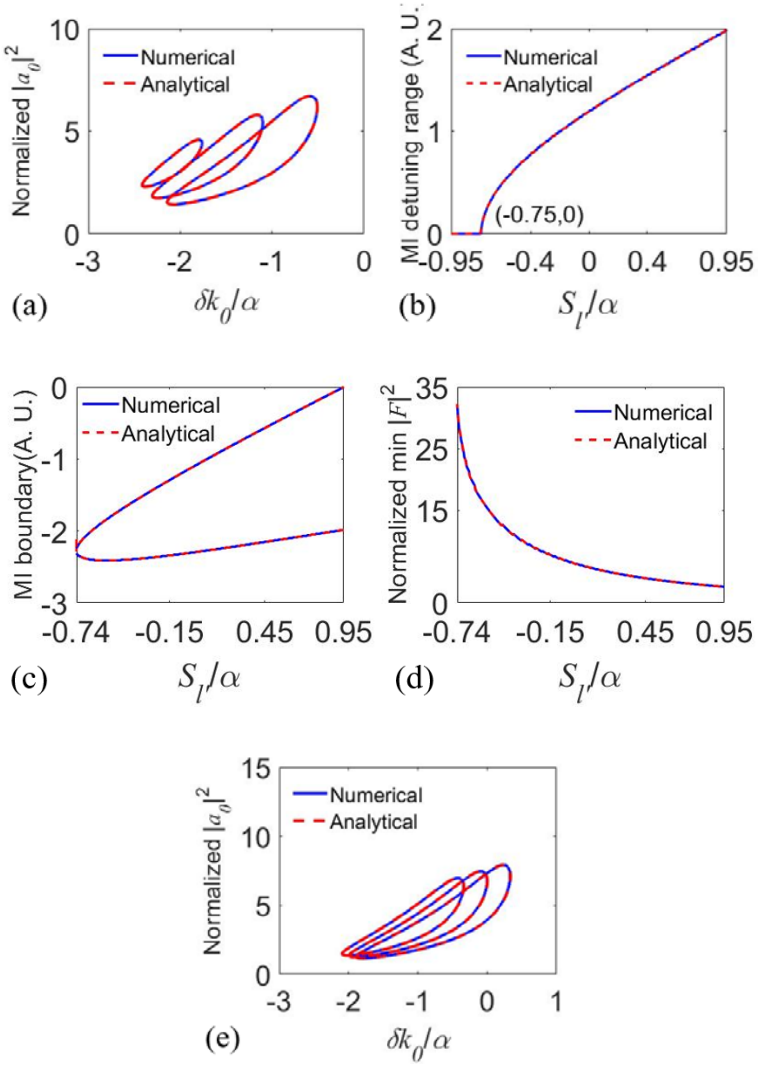

Fig. 3.13 Comparison between the numerically and analytically determined MI regions with different coupling modes detuning $S_{l'}$. The numerical results and analytical results are denoted with blue solid lines and red dashed lines, respectively. The parameters of (a)-(d) are the same as Fig. 3.12(a)-3.12(d) and the parameters of (e) correspond to Fig. 3.12(f).

Fig. 3.14(a) shows numerically determined the MI region with $S_{I'} = 10\alpha$, the 'blue-detuned' MI region almost entirely red-shifts to the red-detuned side and begins to merge with the initially red-detuned MI region. For larger detuning values, e.g., $S_{I'} = 11\alpha$ shown in Fig. 3.14(b), the initially blue-detuned MI region red-shifts more and merges with the initially red-detuned MI region leaving only one MI region. The new MI region existed completely in the blue-detuned region only for $-0.75\alpha \leqslant S_{I'} \leqslant 0.95\alpha$. The merging of the MI regions involves the initially red-detuned region induced by the main cavity optical path. Here we use the numerical results to discuss the merging of the blue-detuned and red-detuned MI regions because the analytical results can only be used to determine the blue-detuned MI region induced by the figure-8 optical path. As discussed in Section 3.2.3, the red-detuned MI region induced by the main cavity optical path cannot be analytically determined. Thus, the merging of blue-detuned and red-detuned MI regions can only be studied numerically. Figs. 3.14(c) and 3.14(d) show the analytically determined MI regions with $S_{I'} = 10\alpha$ and $S_{I'} = 11\alpha$, respectively. The analytical results agree with the numerical results for determining the blue-detuned MI region, while deviating from the numerical results for determining the red-detuned MI region.

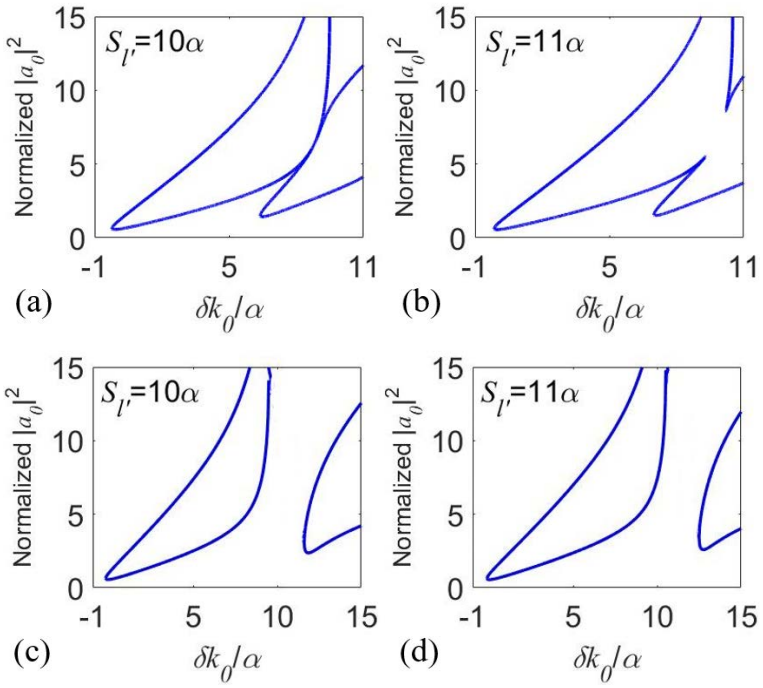

Fig. 3.14 The numerically and analytically determined MI region as a function of the pump detuning and normalized pump laser power $S_{l'} = 10\alpha$ and $S_{l'} = 11\alpha$. (a)(b) and (c)(d) are numerical results and analytical results respectively.

The merging of the two MI regions means that we can use a single pump laser to achieve MI generation with optical fields in both the main cavity optical path and the figure-8 optical path. The generated MI side bands can be coherent or incoherent. MI generation in the merged region should improve the conversion efficiency of the pump to the MI side bands. In this thesis, we focus on the MI generation in blue-detuned MI region. MI generation with red-detuned pump laser in a coupled microcavity system will be studied in our future work.

3.3 Numerical simulation of MI and MI comb generation in coupled microcavity

In this Section, we numerically simulate the MI generation with blue-detuned pump laser. The simulation is based on the coupled mode equations as shown in Eqs. (2.10)

and (2.11). For microcavities with dispersion, the size and location of the blue-detuned MI region depend on the specific mode number under investigation. Here we arbitrarily choose one pair of modes with $l = \pm 150$ and carry out the simulations. In other words, we assume the 150-th modes are the first pair of modes that grow. Other choice of mode number will not affect the results as we have assumed a flat MI gain profile. When the MI gain profile is included, the pair of modes with the highest effect MI gain will grow first. Microcavities with both anomalous and normal dispersion are studied.

We then consider more modes in the simulation with the same pumping parameters. We found that blue-detuned MI will lead to MI combs generation. For a single cavity, MI comb generation arises from cascaded MI processes in the red-detuned MI region with anomalous dispersion. Here we demonstrate that MI comb generation from the blue-detuned MI region in coupled microcavities is possible for both anomalous and normal dispersion. The simulation parameters are extracted from a calcium fluoride microcavity with FSR of 10 GHz, where $\alpha = \alpha' = 402$ kHz, $\gamma = 0.0007$ Hz, and $\theta = 402$ kHz^2. The pump wavelength is 1560 nm and the corresponding Q factor of the cavities is 4.85×10^8. The coupling coefficient and detuning between the two microcavities are chosen as $\theta_c = 1.4$ MHz and $S_{l'} = 0$ Hz, respectively. In our simulation, we consider 850 modes for MI comb generation, the spectrum is sufficiently wide in most cases to prevent aliasing.

3.3.1 MI and MI comb generation in microcavities with anomalous dispersion

We first simulate MI and MI comb generation in the coupled cavities both with anomalous dispersion, where $D_2 = D_2' = 15.7$ Hz. The dispersion parameters are chosen from a practical calcium fluoride microcavity. Eq. (3.16) is a cubic equation and for a given pump power $|F|^2$, there could be three solutions for the pump mode power $|a_0|^2$. It is well known that when there are three solutions, one of the solutions is always unstable leading to a forbidden region of $|a_0|^2$. In the above Sections, we focus on the generation of new MI sidebands and assume there is no limit for $|a_0|^2$. In numerical simulations, the bistability induced limit for $|a_0|^2$ should be considered.

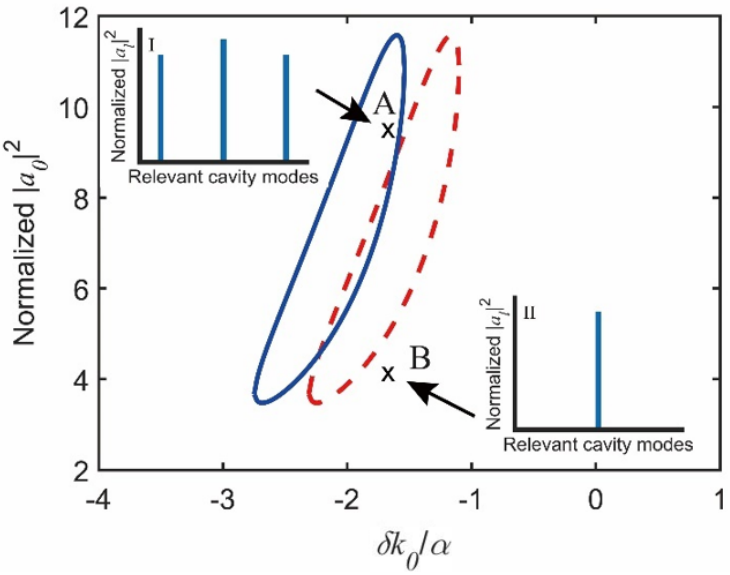

Fig. 3.15 Numerical simulations of MI generation inside (point A) and outside (point B) the blue-detuned MI region. Both the main and auxiliary cavity are with anomalous dispersion. The blue solid lines depict the blue-detuned MI region and the red dashed lines present the forbidden region for $|a_0|^2$. The simulation time is 20 ms and pump parameters for point A are $\delta k_0 = -696$ kHz and $|F|^2 = 30\alpha/\gamma$ and that for point B are $\delta k_0 = -696$ kHz and $|F|^2 = 25\alpha/\gamma$.

Fig. 3.15 presents the selected pumps with parameters inside and outside the blue-detuned MI region and the corresponding simulation results of MI generation. In the simulations, we only consider three modes, the pump mode and the first pair of side modes as we discussed in the previous Sections. The blue solid lines in Fig. 3.15 depict the blue-detuned MI region and the red dashed lines present the forbidden region for $|a_0|^2$. Here we choose point A and point B inside and outside the blue-detuned MI region, respectively, with $\delta k_0 = -696$ kHz, $|F|^2 = 30\alpha/\gamma$, $\delta k_0 = -696$ kHz, and $|F|^2 = 25\alpha/\gamma$. The two points are chosen as representatives inside and outside MI regions, other points in the same parameter space will have similar results. After simulating light propagation for 20 ms in the microcavities, the sidemodes of the pump at point A are fully populated as shown in inset I and no sidemode is excited for point B as shown in inset II of Fig. 3.15. The simulation results show that the pump parameters for MI generation can be selected from the MI region determined with theoretical analysis.

With the same pumping parameters at point A, we consider more modes in the simulations to investigate MI comb generation in microcavities with anomalous dispersion. Fig. 3.16(a) presents the spectrum evolution in the main cavity of the coupled cavity structure. Fig. 3.16(b) presents the spectrum evolution in a single cavity with the same cavity parameters as the main cavity of the coupled cavities. The pumping parameters in the two cases are the same as point A in Fig. 3.15. In Fig. 3.16(a), for the coupled microcavities, the modes around the pump mode begin to be excited at ~0.05 ms. After 0.4 ms, nearly all the modes are populated and form a broadband MI

comb. In comparison, for a single cavity, the modes near the pump mode exist for a short period of time (~0.2 ms) but only the pump mode survives in the microcavity afterward. Thus, the coupled microcavity configuration enables MI comb generation in anomalous dispersion with blue-detuned pump.

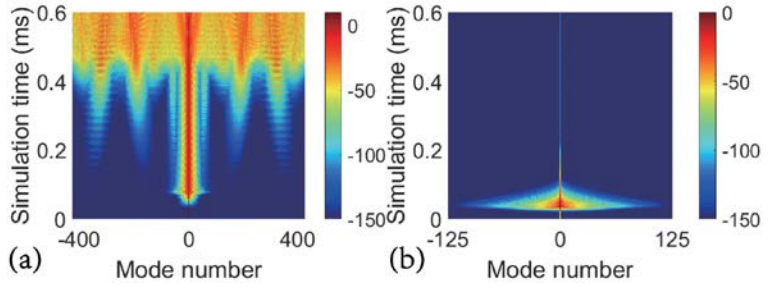

Fig. 3.16 MI comb generation when both microcavities have anomalous dispersion. (a) Spectrum evolution in the main microcavity of a coupled microcavities with the pump parameters of point A in Fig. 3.15. (b) Spectrum evolution in a single microcavity with the same parameters and pump as the main microcavity of the coupled microcavities of point A in Fig. 3.15.

3.3.2 MI and MI comb generation in microcavities with normal dispersion

The blue-detuned MI region induced by the coupled microcavity structure exists in both anomalous and normal dispersion. Here we present the numerical simulations of MI and MI comb generation when both microcavities are normally dispersive with D_2 = D_2' = −15.7 Hz. Fig. 3.17 presents the numerical simulations of MI generation in coupled microcavities with normal dispersion. Only three modes are considered in the simulations. The blue solid lines in Fig. 3.17 show the blue-detuned MI region and the red dashed lines depict the forbidden region for $|a_0|^2$. We choose two pumps with parameters inside and outside the blue-detuned MI region at point A with δk_0 = –426 kHz and $|F|^2 = 165\alpha/\gamma$ and point B with δk_0 = –804 kHz and $|F|^2 = 14\alpha/\gamma$. After a

simulation time of 20 ms, the selected sidemodes with the pump at point A are excited but only the pump mode exists in the cavity with the pump at point B. In a single microcavity, MI generation in microcavities with normal dispersion is only available in a small region at the red-detuned side. The simulation results demonstrate that the coupled microcavity system provides a new blue-detuned region for MI generation in microcavities with normal dispersion.

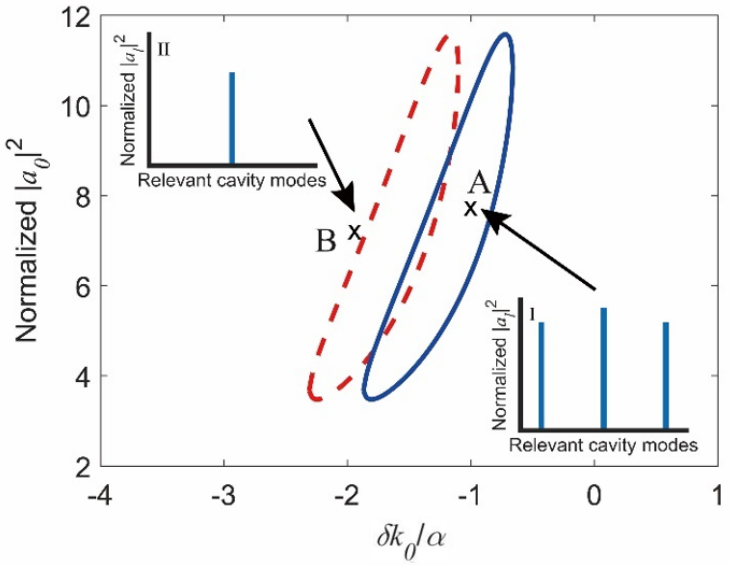

Fig. 3.17 Numerical simulations of MI generation inside (point A) and outside (point B) the blue-detuned MI region when both microcavities are normally dispersive. The solid lines depict the blue-detuned MI region and the dashed lines depict the forbidden region for $|a_0|^2$. The simulation time is 20 ms and the pump parameters for point A are $\delta k_0 = -426$ kHz and $|F|^2 = 165\alpha/\gamma$ and for point B are $\delta k_0 = -804$ kHz and $|F|^2 = 14\alpha/\gamma$.

We consider more modes in the simulation and investigate MI comb generation in normal dispersion microcavities with blue-detuned pumps at point A in Fig. 3.17. Fig. 3.18(a) presents the spectrum evolution in the main cavity of the coupled microcavities. Fig. 3.18(b) shows the spectrum evolution in a single cavity with the same parameters

as the main cavity of the coupled cavities. In Fig. 3.18(a), the first set of sidebands are excited at 0.8 ms and they are away from the pump mode. At around 1 ms, more modes are excited and form a broadband MI comb. Fig. 3.18(b) shows that in a single cavity no mode except the pump mode is excited with the blue-detuned pump. The coupled cavity configuration provides a new region for MI comb generation in normal dispersion microcavities.

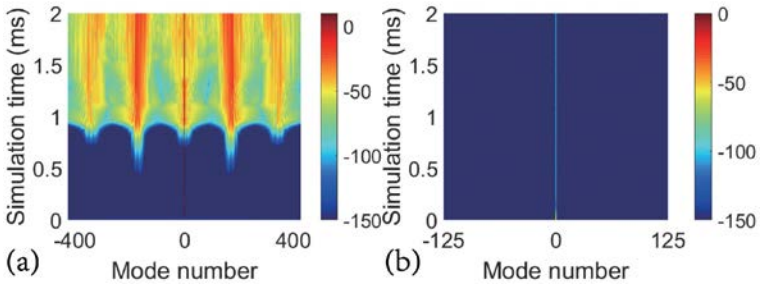

Fig. 3.18 MI comb generation when both microcavities have normal dispersion. (a) Spectrum evolution in the main cavity of a coupled microcavities with the pump parameters at point A of Fig. 3.17. (b) Spectrum evolution in a single cavity with the same parameters and pump as the main cavity of the coupled microcavities.

3.4 Summary

In this Chapter, we theoretically analyze MI generation in coupled microcavities with blue-detuned cw pump laser. MI and MI comb generations based on the blue-detuned pumping regime are numerically simulated in coupled microcavities with both anomalous and normal dispersion. We discovered the existence of a new MI region in the blue-detuned pumping regime when an auxiliary cavity with negligible Kerr nonlinearity is coupled to the main nonlinear cavity. We determine the conditions for the emergence of the blue-detuned MI region by carrying out a stability analysis of a set of modified coupled mode equations. We attribute the blue-detuned MI region to

the additional optical path introduce by the auxiliary cavity, i.e., the figure-8 path. The pump laser is red-detuned with respect to the figure-8 cavity while blue-detuned with respect to the main cavity. We analytically determine the blue-detuned MI region by assuming the auxiliary cavity is in steady state. The analytical results agree well with the numerical results except in some special cases. Firstly, the analytical method cannot be used to determine the initially red-detuned MI region induced by the main cavity optical path. The analytical method assumes the auxiliary cavity functions as a linear filter, while the light propagating in the main cavity only couples with the light returning from the auxiliary cavity through the Kerr nonlinearity. Secondly, the analytical method does not work when the coupling coefficient is too large. This is because when the optical power in the auxiliary cavity is strong, the assumption of the auxiliary cavity going to steady state first breaks down. In such cases, the evolution of the two cavities should be considered together.

4 Soliton microcomb generation in coupled nonlinear microcavities

Compared to MI microcombs, soliton microcombs are more attractive for their low noise spectra. However, the triggering of soliton microcomb in a single microcavity faces several challenges as introduced in Chapter 1. Different techniques such as combined forward and backward cw pump laser [86], two-step “power kicking” by scanning the cw pump laser and decreasing the pump power with acousto-optic modulator [87], slow frequency tuning of the pump laser in conjunction with phase or amplitude modulation [88], and seeding the microcavity with a cw pump laser and a single shot pulse trigger [89], have been proposed to optimize soliton microcomb generation. These solutions all require additional devices that cannot be integrated with the microcavity. In this Chapter, we show that the challenges of soliton generation in a single microcavity can be overcome in a coupled microcavity system. To determine how microcomb solitons are triggered in a coupled microcavity system, we first introduce the soliton microcomb generation in a single microcavity.

4.1 Soliton microcomb generation in a single microcavity

4.1.1 Optical bistability in a single microcavity

The single microcavity pumped by a cw laser is modeled by Eqs. (2.13) and (2.14). Optical bistability is a common phenomenon in nonlinear systems. Previous studies show that soliton microcomb generation is related to the bistability behavior [21]. In

this Subsection, we study the bistability in a single microcavity by considering the stationary cw solutions of the Ikeda map Eqs. (2.13) and (2.14), and determine their temporal stability. The cw solution of Eq. (2.13) is given by

$$E_s(t,L) = E_s(t,0)\exp\left(-i\delta k_0 L - \frac{\alpha L}{2} + i\gamma L_{\text{eff}}\left|E_s(t,0)\right|^2\right), \tag{4.1}$$

where $L_{\text{eff}} = (1-e^{-\alpha L})/\alpha$ is the effective nonlinear length. In steady state, the periodic boundary condition requires $E_{s+1}(t,0) = E_s(t,0)$. Take Eq. (4.1) into Eq. (2.14), we have

$$E_s(t,0) = \sqrt{1-\theta}E_s(t,0)\exp\left(-i\delta k_0 L - \frac{\alpha L}{2} + i\gamma L_{\text{eff}}\left|E_s(t,0)\right|^2\right) + i\sqrt{\theta}F. \tag{4.2}$$

Thus, the intracavity power $|E_s(t,0)|^2$ satisfies the following condition:

$$F^2 = \frac{\left|E_s(t,0)\right|^2}{\theta}\left[(1-\theta)\exp(-\alpha L) - 2\sqrt{1-\theta}\exp(-\alpha L/2)\cos\left(-\delta k_0 L + \gamma L_{\text{eff}}\left|E_s(t,0)\right|^2\right) + 1\right]. \tag{4.3}$$

From Eq. (4.3), for a particular pump laser power F^2, the corresponding intracavity power $|E_s(t,0)|^2$ can have multiple values depending on the parameters θ, α, L, δk_0 and γ. Recall that in Section 3.1.2, effective power coupling from the pump laser to the cavity requires the detuning of the pump laser to balance the nonlinear effect induced phase accumulation, i.e., $(-\delta k_0 L+\gamma L_{\text{eff}}|E_s(t,0)|^2)$ is a small value. Thus, we use the Taylor expansion of $\cos(-\delta k_0 L+\gamma L_{\text{eff}}|E_s(t,0)|^2)$ and ignore the higher-order terms as $1-0.5(-\delta k_0 L+\gamma L_{\text{eff}}|E_s(t,0)|^2)^2$. Eq. (4.3) can be rewritten as

$$\begin{aligned} F^2 = \frac{1}{\theta}\Big\{&\left[(1-\theta)\exp(-\alpha L) + 1 - 2\sqrt{1-\theta}\exp(-\alpha L/2) + 2\sqrt{1-\theta}\exp(-\alpha L/2)\delta k_0{}^2 L^2\right]\left|E_s(t,0)\right|^2 \\ &-4\sqrt{1-\theta}\exp(-\alpha L/2)\delta k_0 \gamma L L_{\text{eff}}\left|E_s(t,0)\right|^4 + 2\sqrt{1-\theta}\exp(-\alpha L/2)\gamma^2 L_{\text{eff}}{}^2\left|E_s(t,0)\right|^6\Big\}. \end{aligned} \tag{4.4}$$

Eq. (4.4) is a cubic polynomial equation in $|E_s(t,0)|^2$, which can have one, two, or three real-valued solutions depending on the parameters F^2, θ, α, L, δk_0 and γ. In a polynomial equation, multiple solutions arise with local extrema. We determine the local extrema by finding the critical values of $|E_s(t,0)|^2$ that make the partial derivative

$$\frac{\partial\left(F^2\right)}{\partial\left(\left|E_s\left(t,0\right)\right|^2\right)}=\frac{1}{\theta}\Big[\left(1-\theta\right)\exp\left(-\alpha L\right)+1-2\sqrt{1-\theta}\exp\left(-\alpha L/2\right)+2\sqrt{1-\theta}\exp\left(-\alpha L/2\right)\delta k_0{}^2L^2$$
$$-8\sqrt{1-\theta}\exp\left(-\alpha L/2\right)\delta k_0\gamma LL_{\text{eff}}\left|E_s\left(t,0\right)\right|^2+6\sqrt{1-\theta}\exp\left(-\alpha L/2\right)\gamma^2L_{\text{eff}}{}^2\left|E_s\left(t,0\right)\right|^4\Big] \tag{4.5}$$

equal to zero. The righthand side of Eq. (4.5) is a quadratic equation in $|E_s(t,0)|^2$, and its discriminant Δ is

$$\Delta=\frac{8\sqrt{1-\theta}\gamma^2L_{\text{eff}}{}^2\exp\left(-\alpha L/2\right)}{\theta^2}\Big[2\sqrt{1-\theta}\exp\left(-\alpha L/2\right)\delta k_0{}^2L^2$$
$$-3\left(1-\theta\right)\exp\left(-\alpha L\right)+6\sqrt{1-\theta}\exp\left(-\alpha L/2\right)-3\Big]. \tag{4.6}$$

Thus, as shown in Fig. 4.1(a), if $2\sqrt{1-\theta}\exp\left(-\alpha L/2\right)\delta k_0{}^2L^2-3\left(1-\theta\right)\exp\left(-\alpha L\right)+6\sqrt{1-\theta}\exp\left(-\alpha L/2\right)-3<0$, there are no such critical values of $|E_s(t,0)|^2$ because there exists no local extrema whereas in Fig. 4.1(b), for $2\sqrt{1-\theta}\exp\left(-\alpha L/2\right)\delta k_0{}^2L^2-3\left(1-\theta\right)\exp\left(-\alpha L\right)+6\sqrt{1-\theta}\exp\left(-\alpha L/2\right)-3\geq 0$, these critical values are

$$\left|E_s(t,0)\right|_{\pm}^{\ 2}=\Big\{4\sqrt{1-\theta}\exp\left(-\alpha L/2\right)\delta k_0L\pm\Big[4\left(1-\theta\right)\exp\left(-\alpha L\right)\delta k_0{}^2L^2$$
$$-6\left(1-\theta\right)\sqrt{1-\theta}\exp\left(-3\alpha L/2\right)+12\left(1-\theta\right)\exp\left(-\alpha L\right)-6\sqrt{1-\theta}\exp\left(-\alpha L/2\right)\Big]^{1/2}\Big\} \tag{4.7}$$
$$/\Big[6\sqrt{1-\theta}\exp\left(-\alpha L/2\right)\gamma L_{\text{eff}}\Big].$$

The corresponding pumping terms $F_{\pm}^2$ can be calculated through Eq. (4.4). In this case, there is a range of pumping power $F_{-}^2\leq F^2\leq F_{+}^2$, where there are three equilibria $|E_s(t,0)|^2_{(1)}$, $|E_s(t,0)|^2_{(2)}$ and $|E_s(t,0)|^2_{(3)}$ ordered as $|E_s(t,0)|^2_{(1)}\leq|E_s(t,0)|^2_{-}\leq|E_s(t,0)|^2_{(2)}\leq$

$|E_s(t,0)|^2_+ \leq |E_s(t,0)|^2_{(3)}$. If these solutions are perturbed in the temporal domain, the extremal solutions $|E_s(t,0)|^2_{(1)}$ and $|E_s(t,0)|^2_{(3)}$ are always stable while the intermediate solution $|E_s(t,0)|^2_{(2)}$ is always unstable. This is well-known bistability in dynamical systems with cubic nonlinearity. Outside the interval $[F_-^2, F_+^2]$, there is always a solution as shown in Fig. 4.1(b). The solutions can be shown to be stable.

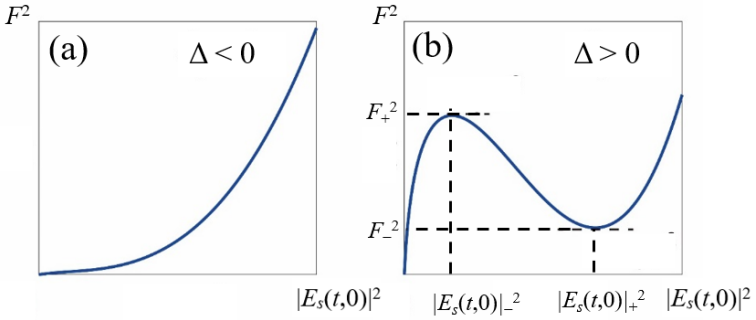

Fig. 4.1 The relationship between the number of steady state solutions in the main cavity and the pump power F^2. (a) For $\Delta < 0$, there is only one solution, and (b) for $\Delta > 0$, there is a range of F^2 in which three solutions exist.

4.1.2 Comb states inside and outside the bistability region

In a microcavity, the loss rate α, cavity length L, Kerr nonlinear coefficient γ, and pump laser coupling coefficient θ are fixed. Thus, the quadratic equation discriminant Δ shown in Eq. (4.6) is function of the wave vector detuning δk_0. We plot a phase diagram in the parameter space of the pump laser power F^2 and wave vector detuning δk_0 to show the bistability region of the single microcavity. In Fig. 4.2, for $\delta k_0 < \rho = \sqrt{\left[3(1-\theta)\exp(-\alpha L/2) - 6\sqrt{1-\theta} + 3\exp(\alpha L/2)\right] / \left(2\sqrt{1-\theta}L^2\right)}$, there is no bistability in the system as shown in Fig. 4.1(a). For $\delta k_0 > \rho$, in the shaded area (between the two curves $F_\pm^2$) in Fig 4.2, the system has three equilibria and bistability (corresponds to

the case in Fig. 4.1(b)) whereas, there is only one stable equilibrium outside the shaded area. The shaded area is referred to as the bistability region.

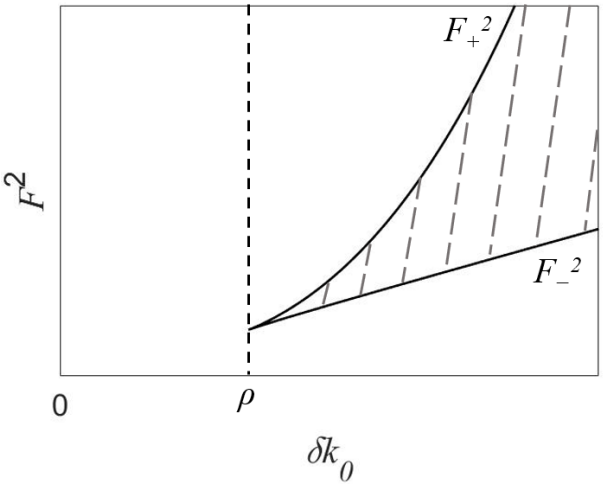

Fig. 4.2 Phase diagram in the parameter space of F^2 and δk_0 to show the bistability region. For $\delta k_0 < \rho$, there is no bistability. For $\delta k_0 > \rho$, the bistability is in the shaded area which is between the two curves for F_+^2 and F_-^2.

We investigate the pulse formation inside and outside the bistability region with numerical simulations. We seed a weak Gaussian pulse in a microcavity with anomalous dispersion and simulate the pulse evolution with different pump parameters inside and outside the bistability region. Fig. 4.3 presents how the pump parameters lead to various stationary states in a cw pumped microcavity. The initial pulse evolves to different states including the chaotic, Turing rolls, cw and soliton state depending on the pumping condition. Note that solitons can only be achieved in the bistability region. However, if we directly use a cw laser with parameters inside the bistability region to pump the microcavity, soliton combs cannot be generated from noise. As discussed in Section 1.2.4, the soliton microcombs cannot grow spontaneously from small perturbations of the cw pump. In Fig. 4.2, if we use a cw laser with parameters inside

the bistability region to pump a cold microcavity, the intracavity optical field will evolve to either of the two stable cw solutions on the boundaries of the bistability region [22]. To achieve the soliton states with cw pumping, the wavelength of the cw pump has to be tuned from outside to inside of the bistability region as discussed in Section 1.2.5. The understanding and control of the bistability region is important for the generation of soliton comb in microcavities. In the following sections in this Chapter, we show that the bistability region of the main cavity can be controlled by the coupling of an auxiliary cavity to the main cavity.

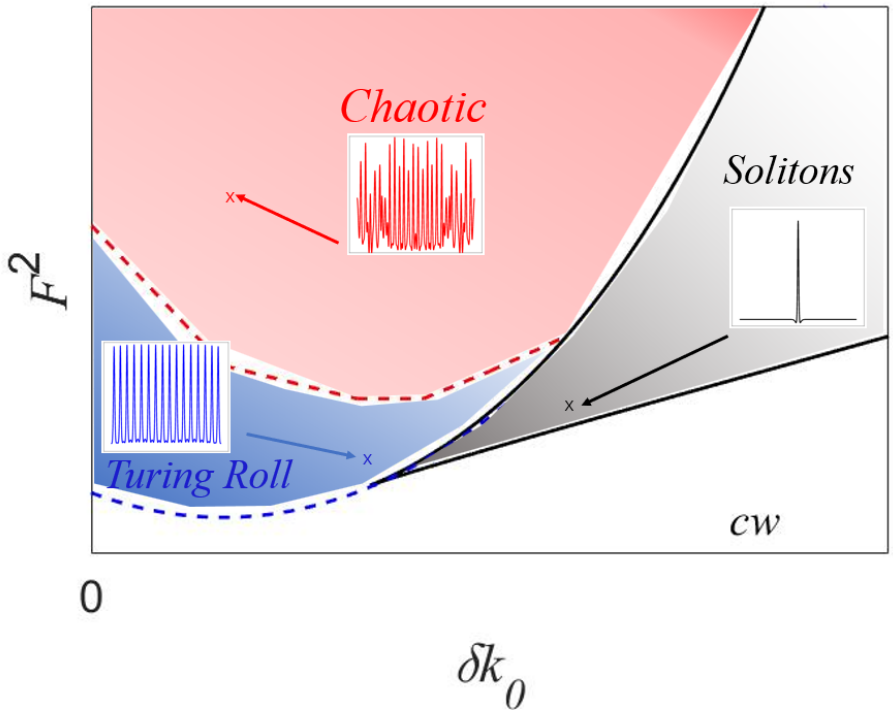

Fig. 4.3 The phase diagram in the (δk_0, F^2)-parameter space showing the different solution regions of a cw pump microcavity. Various solutions including chaotic, Turing rolls, cw and soliton state can be generated. The solitons can only be achieved in the bistability region.

4.2 Bistability region in coupled nonlinear microcavities

Similar to the case of a single microcavity, we determine the bistability region of the coupled nonlinear microcavity system by considering the cw solution of the modified Ikeda map Eqs. (2.15) to (2.19). By setting the temporal derivative in Eq. (2.16) to zero, we have

$$E_s'(t,L') = E_s'(t,0)\exp\left(-i\delta k_0' L' - \alpha' L'/2 + i\gamma' L_{\text{eff,A}}\left|E_s'(t,0)\right|^2\right), \tag{4.8}$$

where $L_{\text{eff,A}} = [1-\exp(-\alpha' L')]/\alpha'$ is the effective nonlinear length of the auxiliary cavity because of the cavity loss. The periodic boundary condition requires $E_{s+1}'(t, 0) = E_s'(t, 0)$. Substitution of Eq. (4.8) into Eq. (2.18), we have

$$E_s(t,L_-/2) = iE_s'(t,0)\left[-1+\sqrt{1-\theta_c}\exp\left(-i\delta k_0' L' - \alpha' L'/2 + i\gamma' L_{\text{eff,A}}\left|E_s'(t,0)\right|^2\right)\right]/\sqrt{\theta_c}. \tag{4.9}$$

Here we use the propagation distance of the optical field to mark the half position of the main cavity. The subscript – and + denote right before and after the position, respectively. From Eqs. (4.8) and (4.9), we can express $E_s(t, L_+/2)$ in Eq. (2.17) as

$$E_s(t,L_+/2) = iE_s'(t,0)\left[\exp\left(-i\delta k_0' L' - \alpha' L'/2 + i\gamma' L_{\text{eff,A}}\left|E_s'(t,0)\right|^2\right)-\sqrt{1-\theta_c}\right]/\sqrt{\theta_c}. \tag{4.10}$$

The cw solution of the optical fields at the coupling point between the main cavity and the auxiliary cavity $E_s'(t, L')$, $E_s(t, L_+/2)$ and $E_s(t, L_-/2)$ can be expressed as functions of $E_s'(t, 0)$. The intracavity power of the main cavity can be determined from the auxiliary cavity field power $|E_s'(t, 0)|^2$. We would like to connect the field $E_s'(t, 0)$ with the pump laser field F such that by using the intermediate variable $E_s'(t, 0)$, we can find the

dependence of the pump laser power F^2 on the intracavity power of the main cavity $|E_s(t, 0)|^2$ and determine the bistability region of the main cavity.

The cw solution of Eq. (2.15) is given by

$$E_s\left(t, L_- / 2\right) = E_s\left(t, 0\right)\exp\left(-i\delta k_0 L / 2 - \alpha L / 4 + i\gamma L_{\text{eff,M}}\left|E_s\left(t, 0\right)\right|^2\right), \tag{4.11}$$

$$E_s\left(t, L\right) = E_s\left(t, L_+ / 2\right)\exp\left(-i\delta k_0 L / 2 - \alpha L / 4 + i\gamma L_{\text{eff,M}}\left|E_s\left(t, L_+ / 2\right)\right|^2\right), \tag{4.12}$$

where $L_{\text{eff,M}} = [1-\exp(-\alpha L/2)]/\alpha$ denotes the effective nonlinear length in the main cavity. Substitution of Eq. (4.11) into Eq. (4.9) we have

$$\begin{aligned} E_s\left(t, 0\right) = iE_s'\left(t, 0\right)\Bigg[-1 + \sqrt{1-\theta_c}\exp\left(-i\delta k_0' L' - \frac{\alpha' L'}{2} + i\gamma' L_{\text{eff,A}}\left|E_s'\left(t, 0\right)\right|^2\right)\Bigg] \\ \exp\left(i\delta k_0 L / 2 + \alpha L / 4 - i\gamma L_{\text{eff,M}}\left|E_s\left(t, 0\right)\right|^2\right) / \sqrt{\theta_c}. \end{aligned} \tag{4.13}$$

Substitution of Eq. (4.10) into Eq. (4.12) we have

$$\begin{aligned} E_s\left(t, L\right) = iE_s'\left(t, 0\right)\Bigg[\exp\left(-i\delta k_0' L' - \alpha' L' / 2 + i\gamma' L_{\text{eff,A}}\left|E_s'\left(t, 0\right)\right|^2\right) - \sqrt{1-\theta_c}\Bigg] \\ \exp\left(-i\delta k_0 L / 2 - \alpha L / 4 + i\gamma L_{\text{eff,M}}\left|E_s\left(t, L_+ / 2\right)\right|^2\right) / \sqrt{\theta_c}. \end{aligned} \tag{4.14}$$

Note that in Eqs. (4.13) and (4.14), $|E_s(t, L_+/2)|^2$ and $|E_s(t, 0)|^2$ can be expressed as a function of $E_s'(t, 0)$ by solving Eqs. (4.10) and (4.13), respectively. As the periodic boundary condition requires $E_{s+1}(t, 0) = E_s(t, 0)$, substitution of Eqs. (4.13) and (4.14) into Eq. (2.19), we can get

$$\begin{aligned} F = E_s'\left(t, 0\right)\Bigg[\left(-1 + \sqrt{1-\theta_c}X_{\text{Aux}}\right)\exp\left(i\delta k_0 L / 2 + \alpha L / 4 - i\gamma L_{\text{eff,M}}\left|E_s\left(t, 0\right)\right|^2\right) \\ -\sqrt{1-\theta}\left(X_{\text{Aux}} - \sqrt{1-\theta_c}\right)\exp\left(-i\delta k_0 L / 2 - \alpha L / 4 + i\gamma L_{\text{eff,M}}\left|E_s\left(t, L_+ / 2\right)\right|^2\right)\Bigg] / \sqrt{\theta_c\theta}, \end{aligned} \tag{4.15}$$

where $X_{\text{Aux}} = \exp\left(-i\delta k_0' L' - \alpha' L' / 2 + i\gamma' L_{\text{eff,A}}\left|E_s'\left(t, 0\right)\right|^2\right)$. The pump laser amplitude F is expressed as a function of $E_s'(t, 0)$. Both the pump laser power F^2 and the main cavity intracavity power $|E_s(t, 0)|^2$ can be determined from the auxiliary cavity power $|E_s'(t,$

0)|^2. We can therefore find the relationship between F^2 and |E_s (t, 0)|^2 through |E_s' (t, 0)|^2, and determine the bistability region of the main cavity. However, from Eq. (4.13) we have

$$\left|E_s(t,0)\right|^2 = \left|E_s'(t,0)\right|^2 \exp(\alpha L/2)\left[1+(1-\theta_c)\exp(-\alpha' L') -2\sqrt{1-\theta_c}\exp(-\alpha' L'/2)\cos\left(-\delta k_0' L' + \gamma' L_{\text{eff,A}}\left|E_s'(t,0)\right|^2\right)\right]/\theta_c, \tag{4.16}$$

where for a particular |E_s (t, 0)|^2, the corresponding |E_s' (t, 0)|^2 can have multiple values depending on the parameters $\delta k_0'$, L', α', θ_c and γ'. Here we would use |E_s' (t, 0)|^2 as an intermediate variable and numerically determine its value from Eq. (4.16) to represent |E_s' (t, 0)|^2 as a function of |E_s (t, 0)|^2, which requires one |E_s' (t, 0)|^2 corresponds to one |E_s (t, 0)|^2, i.e., no bistability in the auxiliary cavity. Recall that we have studied the existence of the bistable steady state in Section 4.1.1. We expand $\cos(-k_0'L'+\gamma' L_{\text{eff,A}}|E_s'(0,t)|^2)$ in a Taylor series about the phase $-k_0'L'+\gamma' L_{\text{eff,A}}|E_s'(0,t)|^2 = 0$ where the detuning between the pump laser frequency and the auxiliary cavity resonance is zero. We neglect terms beyond first order and approximate $\cos(-k_0'L'+\gamma' L_{\text{eff,A}}|E_s'(0,t)|^2)$ as $1-0.5(-k_0'L'+\gamma' L_{\text{eff,A}}|E_s'(0,t)|^2)^2$. With this assumption, Eq. (4.16) is a cubic polynomial equation of $|E_s'(0,t)|^2$. There will be no bistability in the auxiliary cavity for the detuning $\delta k_0' < \rho' = \left[3(1-\theta_c)\exp(-\alpha' L'/2) - 6\sqrt{1-\theta_c} + 3\exp(\alpha' L'/2)\right]^{1/2} / \left(2\sqrt{1-\theta_c}L'^2\right)^{1/2}$, and one $|E_s'(0,t)|^2$ corresponds to one $|E_s(0,t)|^2$. Thus, we can numerically find the relationship between $|E_s(0,t)|^2$ and F^2 through the intermediate variable $|E_s'(0,t)|^2$ with Eqs. (4.15) and (4.16).

4.3 Effect of coupling coefficient on the bistability region of coupled nonlinear microcavities

We first investigate how the coupling coefficient between the two cavities affects the bistability region of the main cavity. In this Section, we assume the two cavities are identical. The parameters of the cavities are cavity length L = 628 μm, cavity loss α = 19.1 /m, group velocity dispersion β_2 = -59 ps^2/km, Kerr nonlinear coefficient γ = 1 /W/m, and the coupling coefficient between the main cavity and the waveguide is θ = 0.0025. The parameters are extracted from a practical silicon nitride microring cavity.

To obtain the bistability region in the main cavity, we consider a series of pump laser detuning values. For each detuning value, we numerically determine if there is bistability in the main cavity and calculate the corresponding local extrema $F_-^2(\delta k_0)$ and $F_+^2(\delta k_0)$. The bistability region of the main cavity with $\theta_c = \theta$ is shown in Fig. 4.4 (a). Compared to the bistability region of a single microcavity in Fig. 4.2, the coupling of the auxiliary cavity creates the bistability region in the blue-detuned side ($\delta k_0 < 0$), where the bistability region of a single cavity only exists in the red-detuned side ($\delta k_0 > 0$). In February 2022, the blue-detuned soliton microcomb generation in coupled nonlinear microcavities was experimentally observed in an arXiv preprint [90].

To investigate whether we can use the bistability region in Fig. 4.4(a) to predict soliton generation, we choose two different pumping parameters, one outside and the other inside the bistability region corresponding to points A and B respectively in Fig. 4.4(a), to study the formation of different stationary solutions. We numerically simulate

Eqs. (2.15)-(2.19) to study the evolution of the optical fields inside the coupled microcavities.

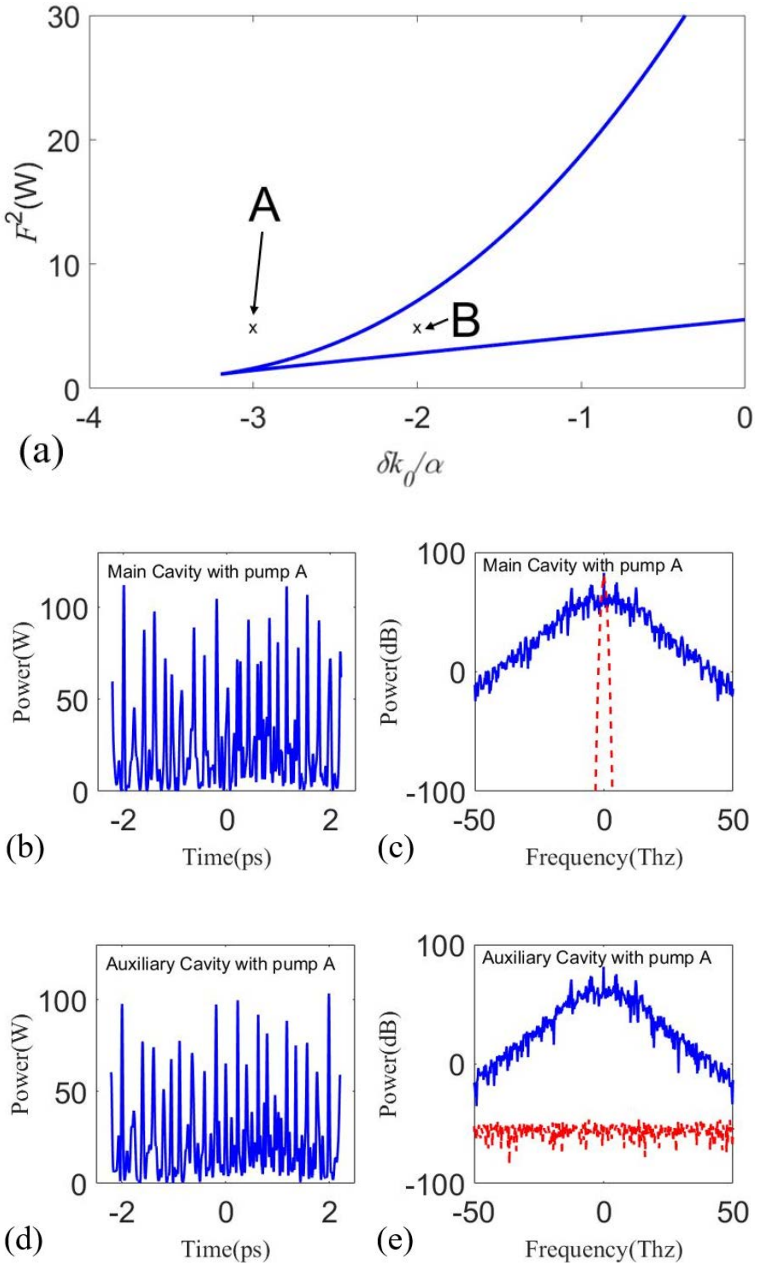

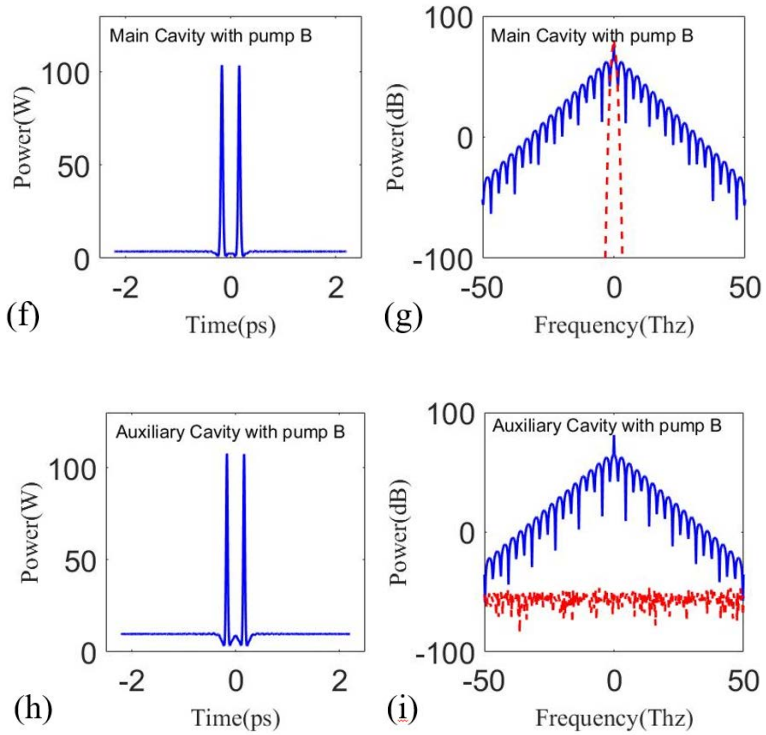

Fig. 4.4 (a) The bistability region of the main cavity with $\theta_c = \theta$. The two blue solid curves correspond to F_- $(\delta k_0)^2$ and F_+ $(\delta k_0)^2$. The (b) temporal and (c) spectral profiles of the chaotic state generated in the main cavity with the pumping parameters at point A of Fig. 4.4(a). The corresponding (d) temporal and (e) spectral profiles in the auxiliary cavity. The (f) temporal and (g) spectral profiles of the soliton generation in the main cavity with pumping parameters at point B of Fig. 4.4(a). The corresponding (h) temporal and (i) spectral profiles in the auxiliary cavity. In the simulations, the initial condition in the main cavity is a Gaussian pulse and the initial condition in the auxiliary cavity is white noise. The spectra of the initial fields inside the corresponding cavities are shown with red dashed lines.

As discussed in Section 4.1.2, noise cannot spontaneously evolve to soliton states. We set the initial field in the main cavity as a weak Gaussian pulse for soliton generation and white noise in the auxiliary cavity. The spectra of the initial optical fields inside the two cavities are shown in Figs. 4.4(c), 4.4(e), 4.4(g) and 4.4(i) with red dashed lines. The pumping parameters outside (point A) and inside (point B) the bistability region are δk_0(A) = -3α, F^2(A) = 5 W and δk_0(A) = -2α, F^2(A) = 5 W, respectively. Figs. 4.4(b) and 4.4(c) respectively show the temporal waveform and the spectrum in the main

cavity after a simulation time of 60 ns for the pumping parameters at point A in Fig. 4.4(a). Both the temporal and spectral profiles of the initial Gaussian pulse evolve to the chaotic state. Figs. 4.4(d) and 4.4(e) respectively show the temporal waveform and spectrum in the auxiliary cavity after 60 ns. The temporal and spectral profiles are also the chaotic state with the similar intracavity power in the main cavity. The spectrum of optical field inside the auxiliary cavity shown in Fig. 4.4(e) is similar to the spectrum of field in the main cavity shown in Fig. 4.4(c). They both have five peaks above the spectrum envelope and the frequencies of the peaks agree well. Figs. 4.4(f)-4.4(i) show the evolution of the initial Gaussian pulse with the pump inside the soliton region at point B. After a simulation time of 60 ns, soliton states are generated in both the main and auxiliary cavities as shown in Figs. 4.4(f) and 4.4(h). The peak power of the solitons in the two cavities are nearly the same and the background cw power in the auxiliary cavity is somewhat higher. Figs. 4.4(g) and 4.4(i) show that the spectra of the pulses in the two cavities are both hyperbolic secant in shape. The spectrum of optical fields in the two cavities are nearly the same. The simulation results suggest that the conditions to generate soliton combs in coupled cavities are similar to that in the single cavity, i.e., we can use the bistability region in coupled microcavity system to predict the conditions for soliton microcomb generation.

We further consider the effect on the bistability region when the coupling coefficient between the two cavities θ_c changes. Fig. 4.5(a) shows three different bistability regions for different coupling coefficients. We find that the bistability region

blue-shifts when the coupling coefficient increases. The soliton that can be generated in the bistability region with the largest blue shift is at the cusp of the bistability region. We define the detuning value and pump laser power at the cusp of the bistability region as δk_p and F_p^2, respectively. We investigate the evolutions of δk_p and F_p^2 at the cusp when the coupling coefficient increases from 0.5θ to 10θ. In Fig. 4.5(b), the detuning of cusp continues to shift deeper into the blue region when θ_c increases. When θ_c increase from 0.5θ to 10θ, δk_p decreases from -1.97α to -12.21α. Fig. 4.5(c) shows the corresponding change of pump laser power at the cusp. We note that $|F_p|^2$ remains almost unchanged, it only decreases slightly from 1.154 to 1.141 W. That is $|\delta k_p|$ increases by ~520% while $|F_p|^2$ decreases by ~1.1% when θ_c increases from 0.5θ to 10θ. Thus, at the cusp, the variation of θ_c mainly affects the detuning but has nearly no effect on the pump laser power.

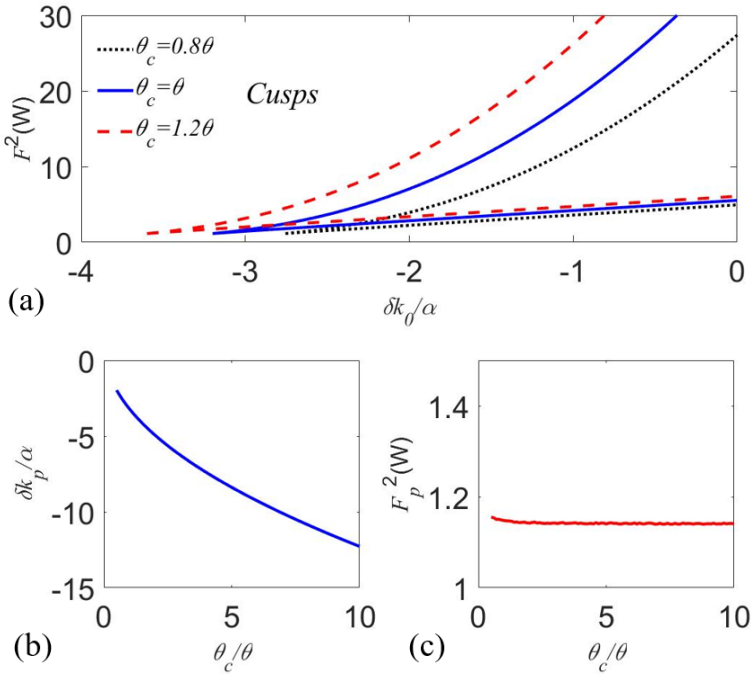

Fig. 4.5 (a) The soliton region of the coupled nonlinear microcavities with $\theta_c = 0.8\theta$ (dotted lines), θ (solid lines), and 1.2θ (dashed lines). The (b) detuning and (c) power of the pump laser at the cusp versus θ_c.

4.4 Resonances of different optical paths

We numerically determine the bistability region of the main cavity with Ikeda map. However, it is hard to explain why the bistability region moves with the variation of coupling coefficient θ_c in Section 4.3. As discussed in Section 3.2.2, the blue-detuned MI region is induced by the figure-8 optical path with the coupling of an auxiliary cavity to the main cavity. It is likely that the blue-detuned bistability region is also related with the figure-8 optical path in the coupled microcavity system. To get a better sense of the physical distribution of the intracavity fields and explain observation in Section 4.3, we analyze the effective wave vector detuning and loss of the figure-8 optical path at steady state.

4.4.1 Figure-8 optical path at steady state

We use the resonance condition to differentiate different optical paths. If the auxiliary cavity length is different from the main cavity, there exists three sets of resonances, i.e., three optical paths. As shown in Fig. 4.6, the three optical paths are the main cavity path, figure-8 cavity path and auxiliary cavity path. To get the effective wave vector detuning and loss of the figure-8 path, we need to study light propagation in the three optical paths.

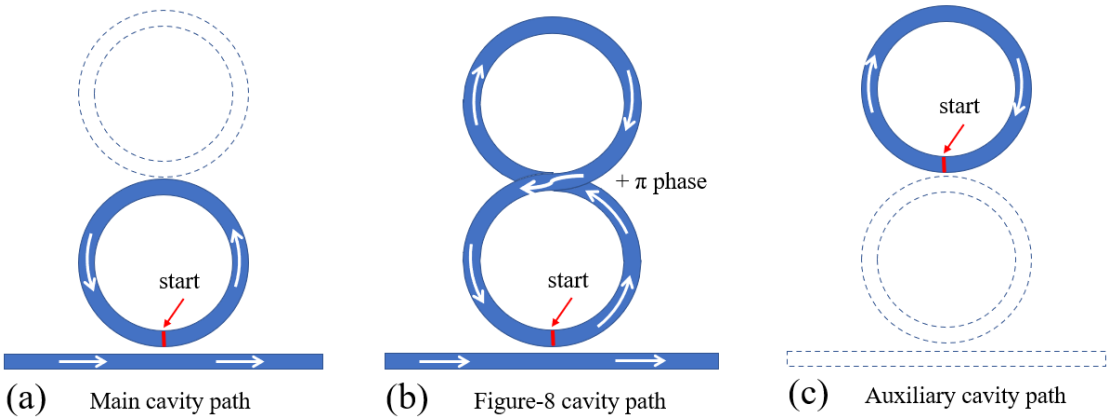

Fig. 4.6. Schematic of three optical paths in a coupled microcavity system: (a) Main cavity path, (b) figure-8 cavity path, and (c) auxiliary cavity path.

The main cavity optical path is shown in Fig. 4.6(a). It starts from the main cavity and does not go through the auxiliary cavity. It is the same as a single microcavity. The optical field propagation of the main cavity path is described by

$$\frac{\partial E_{s,\mathrm{M}}(t,z)}{\partial z} = -i\delta k_0 E_{s,\mathrm{M}}(t,z) - \frac{\alpha}{2} E_{s,\mathrm{M}}(t,z) - i\frac{\beta_2}{2}\frac{\partial^2 E_{s,\mathrm{M}}(t,z)}{\partial t^2} + i\gamma\left(\left|E_{s,\mathrm{M}}(t,z)\right|^2 + \left|E_{s,\mathrm{f8}}(t,z)\right|^2\right)E_{s,\mathrm{M}}(t,z), \tag{4.17}$$

where $E_{s,\mathrm{M}}$ and $E_{s,\mathrm{f8}}$ are the s-th roundtrip fields of the main cavity optical path and figure-8 optical path, respectively.

Fig. 4.6(b) shows the figure-8 optical path. It starts from the main cavity, and goes into the auxiliary cavity at the coupling point between the two cavities. After propagation in the auxiliary cavity, figure-8 optical path meets the coupling point again and goes back to the main cavity. The route of figure-8 path is a compound cavity combined of the main cavity and the auxiliary cavity. Note that at the coupling point, once the optical path goes into a different cavity, it adds π/2 phase to the field. Thus, figure-8 optical path gain π phase in one roundtrip. The light propagation of the figure-8 optical path is divided into two parts. For the part in the main cavity, the field is described by

$$\frac{\partial E_{s,\mathrm{f8}}(t,z)}{\partial z} = -i\delta k_0 E_{s,\mathrm{f8}}(t,z) - \frac{\alpha}{2}E_{s,\mathrm{f8}}(t,z) - i\frac{\beta_2}{2}\frac{\partial^2 E_{s,\mathrm{f8}}(t,z)}{\partial t^2} + i\gamma\left(\left|E_{s,\mathrm{M}}(t,z)\right|^2 + \left|E_{s,\mathrm{f8}}(t,z)\right|^2\right)E_{s,\mathrm{f8}}(t,z). \tag{4.18}$$

For the part in the auxiliary cavity, the field propagation is given by

$$\frac{\partial E_{s,\mathrm{f8}}(t,z)}{\partial z} = -i\delta k_0' E_{s,\mathrm{f8}}(t,z) - \frac{\alpha'}{2}E_{s,\mathrm{f8}}(t,z) - i\frac{\beta_2'}{2}\frac{\partial^2 E_{s,\mathrm{f8}}(t,z)}{\partial t^2} + i\gamma'\left(\left|E_{s,\mathrm{A}}(t,z)\right|^2 + \left|E_{s,\mathrm{f8}}(t,z)\right|^2\right)E_{s,\mathrm{f8}}(t,z). \tag{4.19}$$

where $E_{s,\mathrm{A}}$ is the s-th roundtrip field of auxiliary cavity optical path.

Fig. 4.6(c) gives the auxiliary cavity optical path. It starts from the auxiliary cavity and only propagates in the auxiliary cavity. The equations describing field propagation of auxiliary cavity path is given by

$$\frac{\partial E_{s,\mathrm{A}}(t,z)}{\partial z} = -i\delta k_0' E_{s,\mathrm{A}}(t,z) - \frac{\alpha'}{2}E_{s,\mathrm{A}}(t,z) - i\frac{\beta_2'}{2}\frac{\partial^2 E_{s,\mathrm{A}}(t,z)}{\partial t^2} + i\gamma'\left(\left|E_{s,\mathrm{A}}(t,z)\right|^2 + \left|E_{s,\mathrm{f8}}(t,z)\right|^2\right)E_{s,\mathrm{A}}(t,z). \tag{4.20}$$

Since the main cavity path is the same as a single cavity, its bistability region locates in the red-detuned region with respect to the main cavity resonance. It is not the cause of the blue-detuned bistability region. The light propagating in the auxiliary path does not go into the main cavity. It bears no relation to the bistability region of the main cavity. Thus, we attribute the blue-detuned bistability region to the figure-8 optical path. It should be noted that while the pump cw frequency is blue-detuned with respect to the main cavity resonance, it is red-detuned with respect to the figure-8 cavity. For simplicity, we assume the size of the auxiliary cavity is identical to the main cavity. The FSR of the figure-8 cavity is half of the FSR of the main cavity and the coupling induced π phase blue shifts the resonances of the figure-8 cavity. The resulting resonances of the main cavity and the figure-8 cavity are shown in Fig. 4.7. The blue-detuned bistability region with respect to the main cavity is in fact red-detuned with respect to the figure-8 cavity.

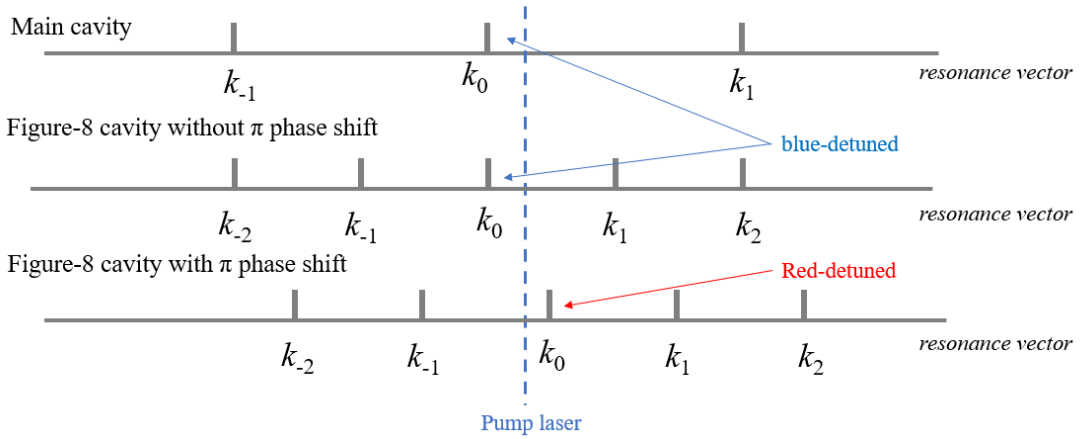

Fig. 4.7 Cavity resonances of main cavity, figure-8 cavity without π phase shift and figure-8 cavity with π phase shift. Due to the coupling induced π phase, the pump cw frequency is blue-detuned with respect to the main cavity resonance while red-detuned with respect to the figure-8 cavity.

4.4.2 Effective detuning and loss of figure-8 cavity

In this Subsection, we derive the expression of optical field in the figure-8 cavity at steady state. With the comparison of figure-8 cavity field to a single cavity field, we can determine the effective wave vector detuning and loss of the figure-8 cavity with a cw pump. The bistability region moving with the change of coupling coefficient discussed in Section 4.3 can be explained with the effective wave vector detuning of figure-8 cavity.

At steady state, the periodic boundary conditions require that

$$\sqrt{1-\theta_c}\left[E_{s,A}\left(t,L_-'\right)+E_{s,f8}\left(t,L/2+L_-'\right)\right]=E_{s,A}\left(t,0\right). \tag{4.21}$$

Here we use the field propagation distance to mark the positions of the cavities and the subscript – denotes the points right before the positions. From Eq. (4.20), we have

$$E_{s,A}\left(t,L_-'\right)=E_{s,A}\left(t,0\right)\exp\left[-i\delta k_0{}'L'-\alpha'L'/2+i\gamma'L_{\text{eff,A}}\left(\left|E_{s,f8}\left(t,L_+/2\right)\right|^2+\left|E_{s,A}\left(t,0\right)\right|^2\right)\right]. \tag{4.22}$$

From Eqs. (4.18) and (4.19), we can get

$$\begin{aligned}E_{s,f8}\left(t,L_+/2\right)&=iE_{s,f8}\left(t,L_-/2\right)\\&=iE_{s,f8}\left(t,0\right)\exp\left[-i\delta k_0L/2-\alpha L/4+i\gamma L_{\text{eff,M}}\left(\left|E_{s,f8}\left(t,0\right)\right|^2+\left|E_{s,M}\left(t,0\right)\right|^2\right)\right],\end{aligned} \tag{4.23}$$

$$\begin{aligned}&E_{s,f8}\left(t,L/2+L_-'\right)=\\&\quad E_{s,f8}\left(t,L_+/2\right)\exp\left[-i\delta k_0{}'L'-\alpha'L'/2+i\gamma'L_{\text{eff,A}}\left(\left|E_{s,f8}\left(t,L_+/2\right)\right|^2+\left|E_{s,A}\left(t,0\right)\right|^2\right)\right].\end{aligned} \tag{4.24}$$

Substitution of Eqs. (4.22), (4.23) and (4.24) into Eq. (4.21), we have

$$E_{s,A}\left(t,0\right)=\frac{\sqrt{1-\theta_c}E_{s,f8}\left(t,L_+/2\right)}{\exp\left[i\delta k_0{}'L'+\alpha'L'/2-i\gamma'L_{\text{eff,A}}\left(\left|E_{s,f8}\left(t,L_+/2\right)\right|^2+\left|E_{s,A}\left(t,0\right)\right|^2\right)\right]-\sqrt{1-\theta_c}}. \tag{4.25}$$

At steady state, the coupling condition requires that

$$E_{s,\mathrm{f8}}\left(t,L/2+L_{+}'\right)=i\sqrt{\theta_{\mathrm{c}}}E_{s,\mathrm{A}}\left(t,0\right)/\sqrt{1-\theta_{\mathrm{c}}}. \tag{4.26}$$

From Eq. (4.18), we have

$$\begin{aligned}E_{s,\mathrm{f8}}\left(t,L+L'\right)&=E_{s,\mathrm{f8}}\left(t,L/2+L_{+}'\right)\\&\exp\left[-i\delta k_0 L/2-\alpha L/4+i\gamma L_{\mathrm{eff,M}}\left(\left|E_{s,\mathrm{f8}}\left(t,L/2+L_{+}'\right)\right|^2+\left|E_{s,\mathrm{M}}\left(t,L/2\right)\right|^2\right)\right].\end{aligned} \tag{4.27}$$

Substitution of Eqs. (4.25) and (4.26) into Eq. (4.27), we can get

$$E_{s,\mathrm{f8}}\left(t,L+L'\right)=\frac{-\sqrt{\theta_{\mathrm{c}}}\exp\left(-i\delta k_0 L-\alpha L/2+i\gamma L_{\mathrm{eff,M}}P_{\mathrm{mix1}}\right)}{\exp\left(i\delta k_0{}'L'+\alpha' L'/2-i\gamma' L_{\mathrm{eff,A}}P_{\mathrm{mix2}}\right)-\sqrt{1-\theta_{\mathrm{c}}}}E_{s,\mathrm{f8}}\left(t,0\right), \tag{4.28}$$

where $P_{\mathrm{mix1}}=\left|E_{s,\mathrm{f8}}\left(t,0\right)\right|^2+\left|E_{s,\mathrm{M}}\left(t,0\right)\right|^2+\left|E_{s,\mathrm{f8}}\left(t,L/2+L_{+}'\right)\right|^2+\left|E_{s,\mathrm{M}}\left(t,L/2\right)\right|^2$, $P_{\mathrm{mix2}}=\left|E_{s,\mathrm{f8}}\left(t,L_{+}/2\right)\right|^2+\left|E_{s,\mathrm{A}}\left(t,0\right)\right|^2$. The effective wave vector detuning and loss of the figure-8 cavity are independent of Kerr nonlinearity. For simplicity, we drop the nonlinear terms and rewrite Eq. (4.28) as

$$E_{s,\mathrm{f8}}\left(t,L+L'\right)=\frac{-\sqrt{\theta_{\mathrm{c}}}\exp\left(-i\delta k_0 L-\alpha L/2\right)}{\exp\left(i\delta k_0{}'L'+\alpha' L'/2\right)-\sqrt{1-\theta_{\mathrm{c}}}}E_{s,\mathrm{f8}}\left(t,0\right). \tag{4.29}$$

Eq. (4.29) can be rewritten as

$$E_{s,\mathrm{f8}}\left(t,L+L'\right)=\exp(iV+W)E_{s,\mathrm{f8}}\left(t,0\right), \tag{4.30}$$

where

$$V=\arctan\left[-\frac{\exp\left(\alpha' L'/2\right)\sin\left(\delta k_0 L+\delta k_0{}'L'\right)-\sqrt{1-\theta_{\mathrm{c}}}\sin\left(\delta k_0 L\right)}{\exp\left(\alpha' L'/2\right)\cos\left(\delta k_0 L+\delta k_0{}'L'\right)-\sqrt{1-\theta_{\mathrm{c}}}\cos\left(\delta k_0 L\right)}\right], \tag{4.31}$$

$$W=\ln\frac{-\sqrt{\theta_{\mathrm{c}}}\exp\left(-\alpha L/2\right)\cos\left(\delta k_0 L\right)}{\exp\left(\alpha' L'/2\right)\cos\left(\delta k_0{}'L'+V\right)-\sqrt{1-\theta_{\mathrm{c}}}\cos\left(V\right)}. \tag{4.32}$$

In a single microcavity with a cavity length of $L+L'$, the intracavity field after one round trip can be written as

$$E_s(t, L+L') = \exp\left[-i\delta k_0 (L+L') - \frac{\alpha}{2}(L+L')\right] E_s(t,0). \tag{4.33}$$

Compare Eq. (4.30) to Eq. (4.33), the effective wave vector detuning $\delta k_{0,f8}$ and effective loss α_{f8} of the figure-8 cavity can be expressed as

$$\delta k_{0,f8} = -V/(L+L'), \tag{4.34}$$

$$\alpha_{f8} = -2W/(L+L'). \tag{4.35}$$

We use Eq. (4.34) to determine the evolution of the effective wave vector detuning of the figure-8 cavity optical path with the change of coupling coefficient. The result is shown in Fig. 4.8. In Fig. 4.8, with the increase of θ_c from 0.5θ to 10θ, the effective wave vector detuning $\delta k_{0,f8}$ blue-shifts from 128.5α to 118.0α. The shift of effective wave vector detuning of the figure-8 cavity optical path can explain the shift of the bistability region shown in Fig. 4.5.

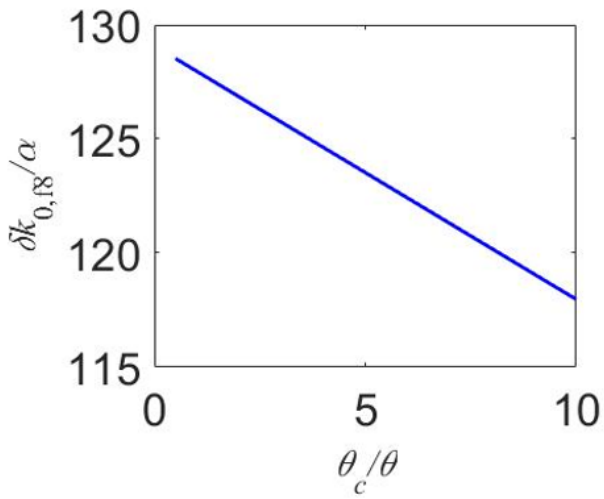

Fig. 4.8 The evolution of effective wave vector detuning of the figure-8 cavity optical path $\delta k_{0,f8}$ with the increase of coupling coefficient θ_c.

4.5 Soliton microcomb generation by tuning the coupling

4.5.1 Trigger of soliton microcomb generation in coupled identical microcavities

As discussed in Chapter 1, excitation of the soliton state is difficult for soliton microcomb generation because it requires to tune the pump laser frequency from outside to inside the bistability region. In this Section, we propose a new soliton comb generation scheme based on our results in Section 4.3. Instead of tuning the pump laser, we tune the bistability region by changing the coupling coefficient between the coupled microcavities. Compared to tuning the pump laser frequency, tuning the coupling coefficient has two major advantages. Firstly, this method avoids using a tunable cw laser making it possible to achieve chip-scale integration for soliton comb generation. Secondly, if we use a microheater to control the coupling coefficient between the cavities, the heating area will be very small. We only need to cover the small region where the two cavities meet with each other. Thus, the tuning efficiency and stability will not be affected by the cavity size, i.e., this method can be applied to microcavities with relatively large scales.

We numerically simulated soliton comb generation by tuning the coupling coefficient of a pair of coupled Si_3N_4 microcavities. The simulation parameters are L = 628 μm, δk_0 = –40.1 /m, α = 19.1 /m, β_2 = –59 ps^2/km, γ = 1 /W/m, θ = 0.0025, and F^2 = 3 W. Fig. 4.9 shows the simulation results of light propagation inside the main cavity and the auxiliary cavity. Fig. 4.9(a) depicts the change of the coupling coefficient. In

the first 8000 roundtrips (around 35 ns), θ_c increases linearly from 0 to θ, and then stays constant at θ in the next 8000 roundtrips. Figs. 4.9(b) and 4.9(c) show the evolution of the temporal and spectral profiles of the optical field in the main cavity. The intracavity optical field experiences MI and chaotic states before a single soliton emerges. Figs. 4.9(d) and 4.9(e) respectively show the temporal and spectral profiles of the field in the main cavity at the final roundtrip (16000-th). Figs. 4.9(f) and 4.9(g) show the corresponding temporal and spectral evolutions of the optical field in the auxiliary cavity. The field evolution in the auxiliary cavity is similar to that in the main cavity. MI grows at around the 6000-th roundtrip and after about another 2000 roundtrips, a single soliton emerges from the chaotic state. Figs. 4.9(h) and 4.9(i) show the temporal and spectral profiles of the field in the auxiliary cavity at the final roundtrip, which are similar to that in the main cavity. The simulation results demonstrate that soliton combs can be generated by tuning the coupling coefficient in coupled microcavities.

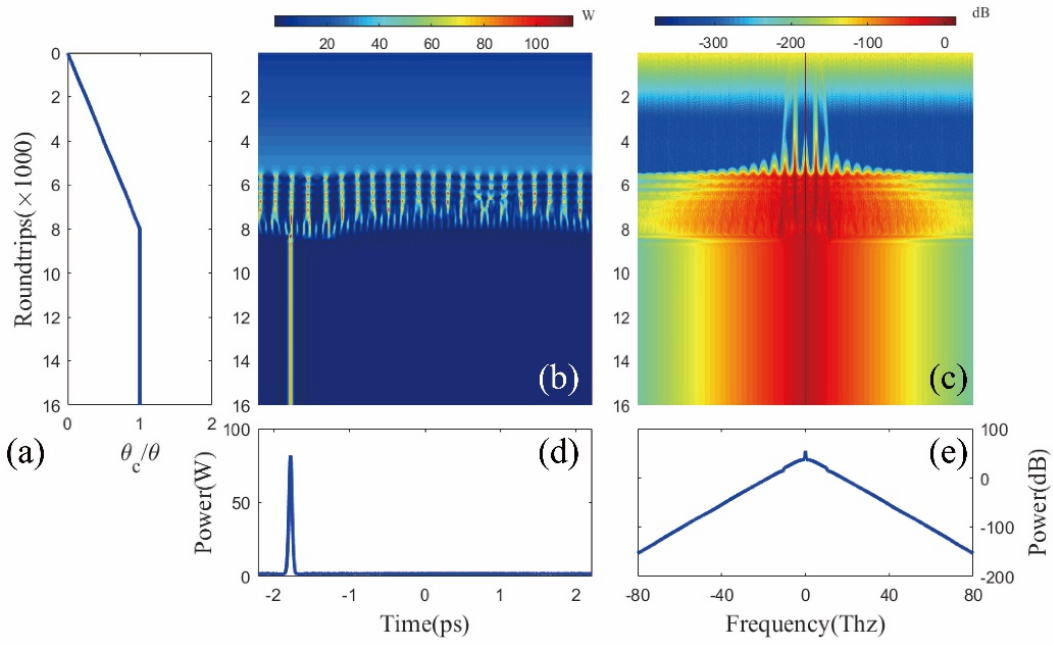

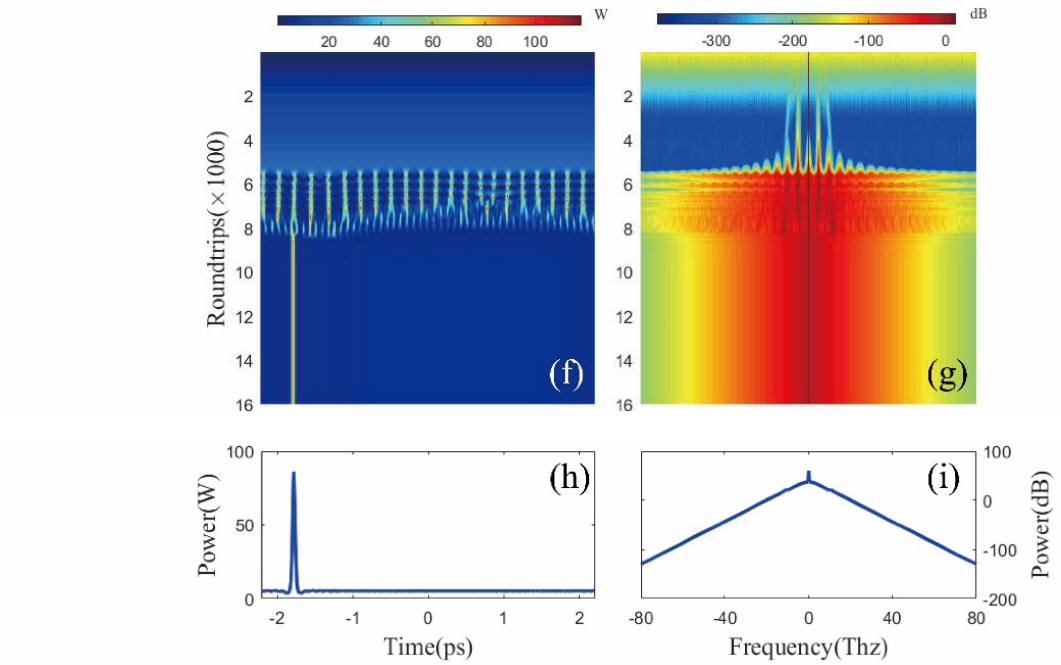

Fig. 4.9. (a) The change in the coupling coefficient in 16000 roundtrips. The (b) temporal and (c) spectral evolution of the intracavity optical field in the main cavity. The instantaneous (d) temporal and (e) spectral profiles of the optical field in the main cavity at the 16000-th roundtrip. The (f) temporal and (g) spectral evolution of the intracavity optical field in the auxiliary cavity. The instantaneous (h) temporal and (i) spectral profiles of optical field in the auxiliary cavity at the 16000-th roundtrip.

4.5.2 Soliton microcomb generation in a CW-CCW coupled nonlinear microcavity by tuning the coupling

In practice, it is difficult to fabricate two coupled microcavities with exactly the same parameters. Thus, it is advantageous if the two coupled light waves are generated in the same microcavity as in the case of a CW-CCW coupled microcavity.

Schematic of a CW-CCW coupled microcavity

The analysis in Section 4.3 is not limited to two physically separated microcavities, but can also describe the coupling of the CW and CCW modes in the same microcavity. We propose a Sagnac loop like structure to achieve soliton microcomb generation by

tuning the coupling between the CW and CCW modes. Fig. 4.10 shows the schematic of the proposed microcavity configuration. The coupling coefficient between the CW and CCW modes is tuned at the coupling region.

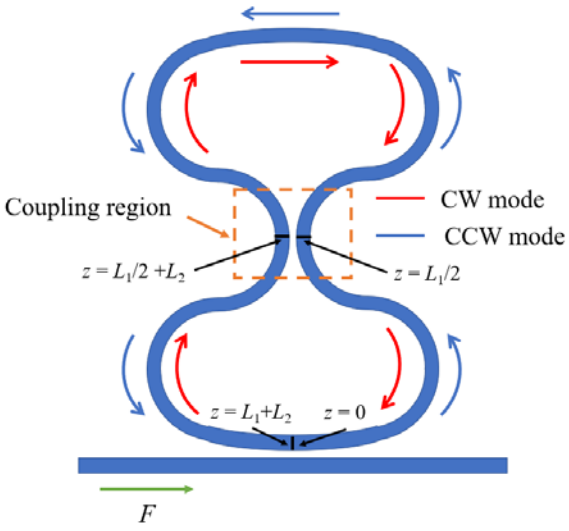

Fig. 4.10 Schematic of a CW-CCW coupled microcavity. The CW and CCW modes are presented with red and blue solid lines. The coupling points are marked with black solid line, where the lengths of the lower half cavity and the upper half cavity are L_1 and L_2.

The CW-CCW coupled microcavity is different from the two physically separated microcavities in two aspects. Firstly, since the CW and CCW modes propagate in the same waveguide, we need to include the effect of cross phase modulation (XPM) between the two modes. In addition to the linear coupling at the coupling region, CW and CCW modes are nonlinearly coupled through XPM. Secondly, in the CW-CCW coupled microcavity, the CW and CCW modes couple twice in one roundtrip, where in two physically separated microcavities, the main cavity mode and auxiliary mode couple only once in one roundtrip. Thus, the Ikeda map describing CW-CCW coupled microcavity should be modified as

$$\frac{\partial E_s(t,z)}{\partial z} = -i\delta k_0 E_s(t,z) - \frac{\alpha}{2} E_s(t,z) - i\frac{\beta_2}{2}\frac{\partial^2 E_s(t,z)}{\partial t^2} + i\gamma\left(\left|E_s(t,z)\right|^2 + 2\left|E_s'(t,z)\right|^2\right)E_s(t,z), \tag{4.36}$$

$$\frac{\partial E_s'(t,z)}{\partial z} = -i\delta k_0 E_s'(t,z) - \frac{\alpha}{2} E_s'(t,z) - i\frac{\beta_2}{2}\frac{\partial^2 E_s'(t,z)}{\partial t^2} + i\gamma\left(\left|E_s'(t,z)\right|^2 + 2\left|E_s(t,z)\right|^2\right)E_s'(t,z), \tag{4.37}$$

$$E_s\left[t,(L_1/2)_+\right] = \sqrt{1-\theta_c}E_s\left[t,(L_1/2)_-\right] + i\sqrt{\theta_c}E_s'\left[t,(L_1/2+L_2)_-\right], \tag{4.38}$$

$$E_s\left[t,(L_1/2+L_2)_+\right] = \sqrt{1-\theta_c}E_s\left[t,(L_1/2+L_2)_-\right] + i\sqrt{\theta_c}E_s'\left[t,(L_1/2)_-\right], \tag{4.39}$$

$$E_s'\left[t,(L_1/2+L_2)_+\right] = \sqrt{1-\theta_c}E_s'\left[t,(L_1/2+L_2)_-\right] + i\sqrt{\theta_c}E_s\left[t,(L_1/2)_-\right], \tag{4.40}$$

$$E_s'\left[t,(L_1/2)_+\right] = \sqrt{1-\theta_c}E_s'\left[t,(L_1/2)_-\right] + i\sqrt{\theta_c}E_s\left[t,(L_1/2+L_2)_-\right], \tag{4.41}$$

$$E_s(t,0) = \sqrt{1-\theta_c}E_s(t,L_1+L_2) + i\sqrt{\theta_c}F, \tag{4.42}$$

$$E_s'(t,L_1+L_2) = \sqrt{1-\theta_c}E_s'(t,0), \tag{4.43}$$

where E_s and E_s' denote the s-th roundtrip optical fields of the CCW mode and the CW mode. The coupling coefficient between the two modes at the coupling region is θ_c. We use the coupling point to divide the cavity into two parts. L_1 and L_2 are the lengths of the lower half cavity and upper half cavity, respectively. In Fig. 4.10, we mark the positions at the coupling points as z = 0, $L_1/2$, $L_1/2+L_2$ and L_1+L_2. X_- and X_+, where X = $L_1/2$, $L_1/2+L_2$, or L_1+L_2, denote the locations just before and just after the point X, respectively.

Although there are differences between the CW-CCW coupled microcavities and the physically separated coupled microcavities, we expect that soliton microcomb can still be generated by tuning the coupling coefficient in a CW-CCW coupled

microcavities. The effect of XPM is to increase the nonlinear phase change, which effectively increases the Kerr nonlinear coefficient. The value of the Kerr nonlinear coefficient does not affect the soliton triggering scheme. As for the difference in the number of couplings in one roundtrip, here we show that the double coupling can be regarded as a single coupling with a different coupling strength if we ignore the nonlinear effects and assume cw solution in the CW-CCW coupled microcavity.

In steady state, the stationary solution of Eqs. (4.36) and (4.37) give

$$E_s\left[t,\left(L_1/2+L_2\right)_-\right]=E_s\left[t,\left(L_1/2\right)_+\right]\exp\left(-i\delta k_0L_2-\alpha L_2/2\right), \tag{4.44}$$

$$E_s'\left[t,\left(L_1/2\right)_-\right]=E_s'\left[t,\left(L_1/2+L_2\right)_+\right]\exp\left(-i\delta k_0L_2-\alpha L_2/2\right). \tag{4.45}$$

Substitution of Eqs. (4.44), (4.45), (4.38) and (4.40) into Eqs. (4.39) and (4.41), we have

$$\begin{aligned}&E_s\left[t,\left(L_1/2+L_2\right)_+\right]=\\&\left\{\sqrt{1-4\left(1-\theta_c\right)\theta_c}E_s\left[t,\left(L_1/2\right)_-\right]+i\sqrt{4\left(1-\theta_c\right)\theta_c}E_s'\left[t,\left(L_1/2+L_2\right)_-\right]\right\}\exp\left(-i\delta k_0L_2-\alpha L_2/2\right),\end{aligned} \tag{4.46}$$

$$\begin{aligned}&E_s'\left[t,\left(L_1/2\right)_+\right]=\\&\left\{i\sqrt{4\left(1-\theta_c\right)\theta_c}E_s\left[t,\left(L_1/2\right)_-\right]+\sqrt{1-4\left(1-\theta_c\right)\theta_c}E_s'\left[t,\left(L_1/2+L_2\right)_-\right]\right\}\exp\left(-i\delta k_0L_2-\alpha L_2/2\right).\end{aligned} \tag{4.47}$$

Eqs. (4.46) and (4.47) can be rewritten as

$$\begin{aligned}&\begin{Bmatrix}E_s\left[t,\left(L_1/2+L_2\right)_+\right]\\E_s'\left[t,\left(L_1/2\right)_+\right]\end{Bmatrix}=\\&\begin{Bmatrix}\sqrt{1-4\left(1-\theta_c\right)\theta_c} & i\sqrt{4\left(1-\theta_c\right)\theta_c}\\ i\sqrt{4\left(1-\theta_c\right)\theta_c} & \sqrt{1-4\left(1-\theta_c\right)\theta_c}\end{Bmatrix}\begin{Bmatrix}E_s\left[t,\left(L_1/2\right)_-\right]\\E_s'\left[t,\left(L_1/2+L_2\right)_-\right]\end{Bmatrix}\exp\left(-i\delta k_0L_2-\alpha L_2/2\right).\end{aligned} \tag{4.48}$$

Compare Eq. (4.48) to Eq. (1.8), the double coupling shown in Eqs. (4.38)-(4.41) can be considered as a single coupling, where the effective coupling coefficient is $\theta_{c,eff} = 4(1-\theta_c)\theta_c$.

Numerical simulation of soliton microcomb generation in a CW-CCW coupled microcavity by tuning the coupling

We use Eqs. (4.36) - (4.43) to simulate the soliton microcomb generation by tuning the coupling in a CW-CCW coupled microcavity. The simulation parameters are L_1 = 251 μm, L_2 = 377 μm, δk_0 = –40.1 /m, α = 19.1 /m, β_2 = –59 ps^2/km, γ = 1 /W/m, θ = 0.0025, and F^2 = 0.5 W. Note that XPM effectively increases the Kerr nonlinear coefficient, the pump laser power required for soliton microcomb generation in a CW-CCW coupled microcavity is lower than the pump power requirement in two physically separated coupled cavities with same parameters. Fig. 4.11 shows the simulation results. The coupling coefficient is increased linearly from 0 to 0.25θ in the first 8000 roundtrips and kept constant in the next 8000 roundtrips as shown in Fig. 4.11(a). Figs. 4.11(b) and 4.11(c) respectively show that the optical field and spectrum in the CCW direction first experience MI and then a single soliton emerges from the chaotic state. Figs. 4.11(d) and 4.11(e) show the temporal and spectral profiles of the CCW mode at the 16000-th roundtrip. The corresponding optical field and spectrum evolution in the CW direction are shown in Figs. 4.11(f) and 4.11(g), respectively. The optical field propagation of the CW mode is similar to that of the CCW mode. The temporal and spectral profiles of the single soliton generated in the CW direction at the 16000-th round trip are shown

in Figs. 4.11(h) and 4.11(i), respectively. The simulation results demonstrate soliton microcomb generation by tuning the coupling in a CW-CCW coupled microcavity. The proposed scheme provides a simple and effective solution to realize on-chip integrated soliton microcomb sources.

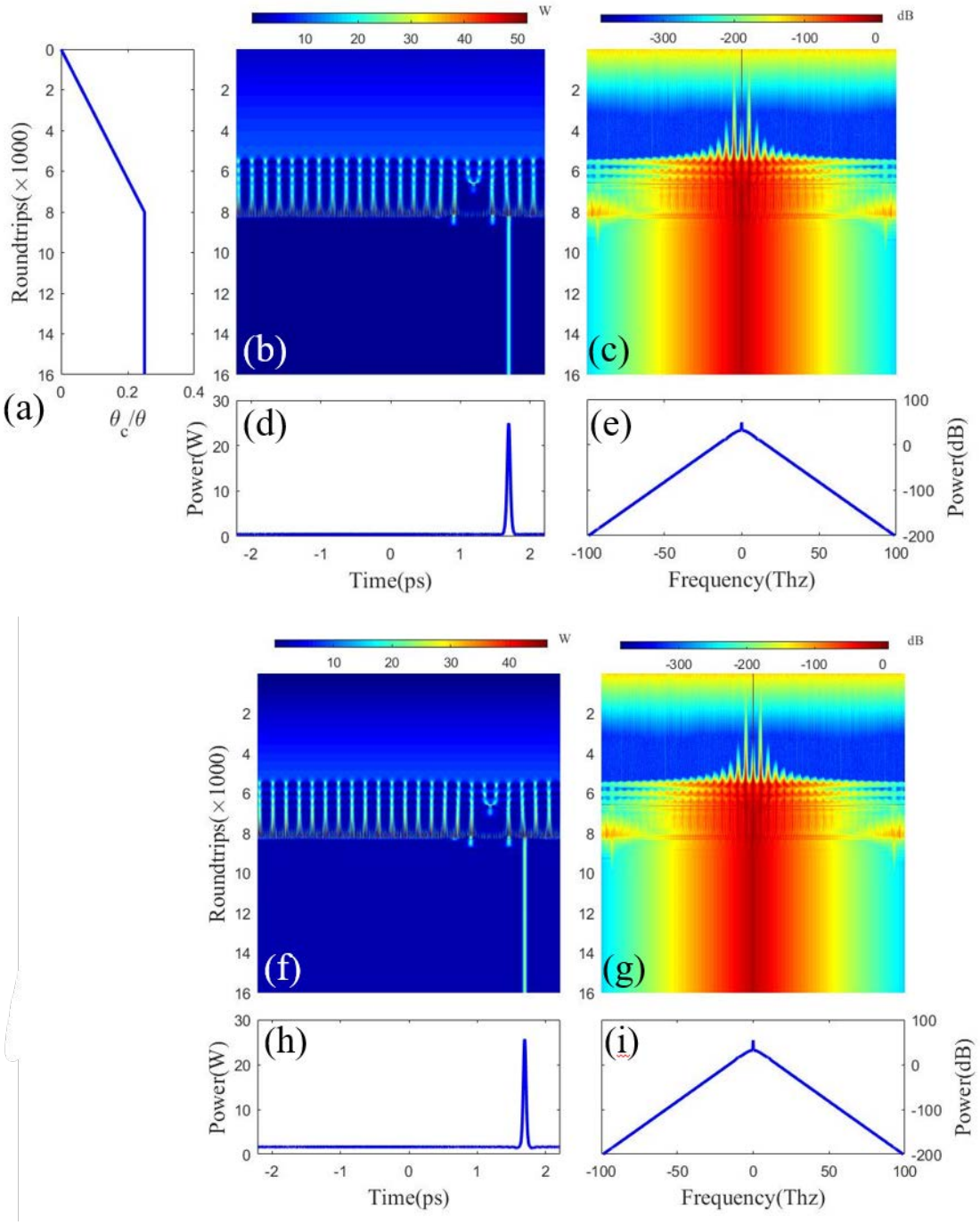

Fig. 4.11 (a) The change in the coupling coefficient in 16000 roundtrips. The (b) temporal and (c) spectral evolution of the intracavity optical field of the CCW mode. The instantaneous (d) temporal and (e) spectral profiles of the optical field of the CCW mode at the 16000-th roundtrip. The (f) temporal and (g) spectral evolution of the intracavity optical field of the CW mode. The instantaneous (h) temporal and (i) spectral profiles of the optical field of the CW mode at the 16000-th roundtrip.

4.6 Reducing the requirement of Q factor for soliton microcomb generation by coupling an auxiliary cavity with gain

The requirement for high Q (low loss) microcavities is another challenge for soliton microcomb generation as discussed in Chapter 1. In an optical fiber cavity, it is easy to add a gain element in the cavity to decrease the total cavity loss [91]. However, it is hard to insert a gain element in a microcavity. Although an on-chip erbium-doped waveguide with gain has been reported recently [92], it is hard to fabricate a microcavity with different materials because of the mode matching between waveguides with different materials. Thus, it is still a challenge to fabricate an on-chip microcavity with partial gain element. In this Section, we propose to solve the problem by coupling an auxiliary cavity with gain to the main cavity. Compare to matching the modes in two on-chip waveguides, it is easier to achieve mode coupling between two microcavities with the various techniques discussed in Section 2.1.1. In the following, we demonstrate soliton microcomb generation in a low Q main cavity by coupling to an auxiliary cavity with gain.

In a single microcavity, as shown in Fig. 4.2, the minimum pump laser power for soliton microcomb generation is at the cusp of the bistability region. The cusp power is proportional to the cavity loss. When the cavity loss increases, higher pump laser power is required to generate soliton microcombs. For a microcavity with a Q factor of 2.3×10^6 (the corresponding cavity loss is 0.3 dB/cm), the pump laser power for soliton

microcomb generation should be larger than 1 W. However, the power of a typical on-chip semiconductor laser is less than 100 mW. Thus, the power required for soliton microcomb generation must be lower than 100 mW to realize chip-scale comb sources.

We first investigate the effect of an auxiliary gain cavity on the bistability region of the main cavity, where the Q factor of the main cavity is 7.6×10^6. The coupled microcavity system is shown in Fig. 2.6 and the bistability region is numerically determined with Eq. (4.15). The cavity parameters are the same as Section 4.5 and we assume $L = L'$, $\delta k_0 = \delta k_0'$, $\beta_2 = \beta_2'$, $\gamma = \gamma'$ and $\theta_c = \theta$. Fig. 4.12(a) presents the bistability region when the auxiliary cavity has different gain values. The sign of α' is negative because the auxiliary cavity has gain. When the auxiliary cavity gain increases, the cusp detuning δk_p blue shifts and the cusp power F_p^2 decreases. Fig. 4.12(b) provides a close-up view of the bistability regions with $\alpha' = -0.05\alpha$, $\alpha' = -0.5\alpha$ and $\alpha' = -\alpha$. Fig. 4.12(c) shows the evolution of δk_p and F_p^2 with α' varying from -0.01α to -0.5α. When the gain of the auxiliary cavity increases, δk_p blue shifts from -3.55α to -3.75α and F_p^2 reduces from 0.3 W to 0.08 W.

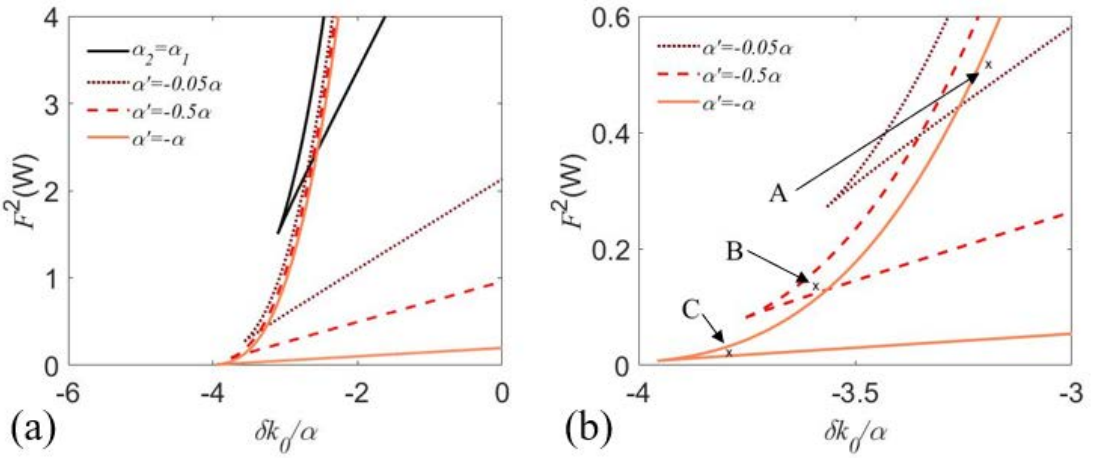

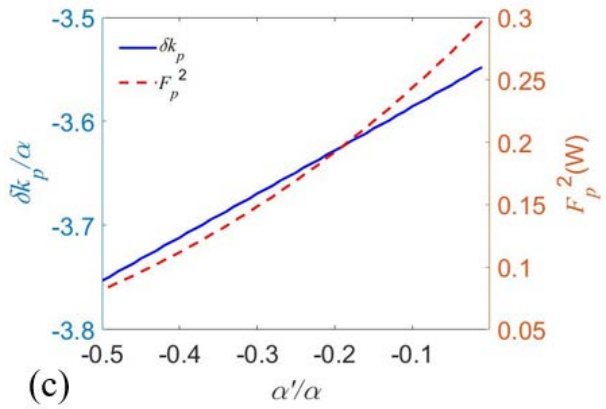

Fig. 4.12 (a) Bistability regions of coupled microcavities with $\alpha' = \alpha$ (black solid line), $\alpha' = -0.05\alpha$ (red dotted lines), $\alpha' = -0.5\alpha$ (red dashed lines), and $\alpha' = -\alpha$ (red solid lines). (b) A close up view the of bistability regions of the coupled microcavities, the detuning at A, B and C are -3.2α, -3.6α and -3.8α, respectively, the corresponding pump power are 0.5 W, 0.139 W and 0.023 W, respectively. (c) Evolution of δk_p and F_p^2 as a function of auxiliary cavity gain.

We perform numerical simulations to see if solitons can be generated in the modified bistability region. We select two pumping conditions A and B in Fig. 4.12 (b), where A is inside the bistability region of $\alpha' = -0.05\alpha$ and outside the bistability region of $\alpha' = \alpha$, B is inside the bistability region of $\alpha' = -0.5\alpha$ and outside the bistability region of $\alpha' = -0.05\alpha$. The detuning value at A and B are -3.2α and -3.6α, respectively, and the corresponding pump powers are 0.5 W and 0.139 W, respectively. The initial condition is also a Gaussian pulse. Figs. 4.13(a) and 4.13(b) show the pulse evolutions with pump at point A. When $\alpha' = \alpha$, no pulse can survive and the initial Gaussian pulse turns into cw state as shown in Fig. 4.13(a). When $\alpha' = -0.05\alpha$ in Fig. 4.13(b), the initial pulse first involves to a soliton molecule and then turns into a single soliton state. When $\alpha' = -0.05\alpha$, the pump at point B is outside the bistability region and no soliton can form with the initial Gaussian pulse as shown in Fig. 4.13(c). At a larger gain value, $\alpha' = -0.5\alpha$ and pump at point B shown in Fig. 4.13(d), the initial pulse directly evolves

into a soliton molecule state. The simulation results demonstrate that the bistability region with an auxiliary gain cavity shown in Fig. 4.12(b) can support the soliton microcomb generation.

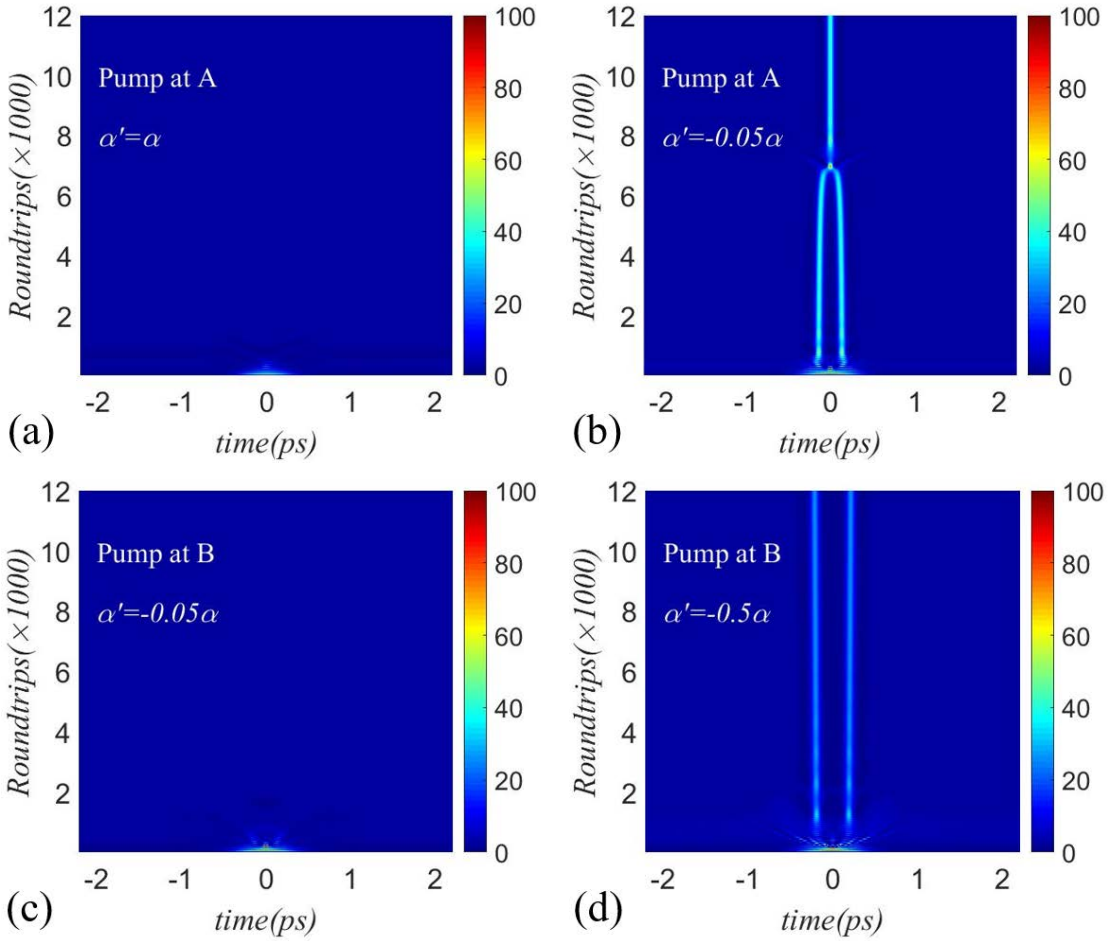

Fig. 4.13 An initial Gaussian pulse evolution in coupled microcavities with pumping condition at (a) point A with $\alpha' = \alpha$, (b) point A with $\alpha' = -0.05\alpha$, (c) point B with $\alpha' = -0.05\alpha$, and (d) point B with $\alpha' = -0.5\alpha$.

The theoretical analysis and the simulation results indicate that if the auxiliary cavity can provide gain, the pump power required for soliton microcomb generation in the main cavity will be reduced compared to a single microcavity. When the auxiliary cavity gain increases, the pump power at the cusp of the bistability region in coupled microcavities can be even lower than that in a single cavity with the same parameters

as the main cavity. Fig. 4.14(a) presents the bistability regions of coupled microcavities with an auxiliary gain cavity and a single microcavity. The cavity parameters of the single cavity are the same as the main cavity of the coupled microcavities. The minimum power at the cusp (i.e., minimum pump laser power for soliton generation) of the bistability region in the coupled cavities with $\alpha' = -0.5\alpha$ is lower than that in a single cavity. Since the power at the cusp of the bistability region is proportional to the cavity loss, Fig. 4.14(a) confirms the idea of using an auxiliary gain cavity to reduce the effective loss of the main cavity.

It should be pointed out that when the gain of the auxiliary cavity is too large, i.e., when the coupled cavity system becomes a gain cavity, DKSs cannot be generated. In Fig. 4.12(b), $\alpha' = -\alpha$ gives a larger bistability region and much lower pump power at the cusp of the bistability region. In order to see if solitons can be generated under that condition, we choose a pump at the point C in the bistability region with $\alpha' = -\alpha$. The corresponding detuning value and pump power are -3.8α and 0.023 W, respectively. We do a numerical simulation of pulse evolution at the point C with $\alpha' = -\alpha$ and the simulation result is shown in Fig. 4.14(b). The soliton comb cannot be generated with such a large gain. The generation of DKSs in microcavities requires a balance between the cavity loss and the MI gain, i.e., the cavities have to be dissipative. As discussed in Section 4.4, the effective loss of the coupled microcavities could be approximate the effective loss of the figure-8 cavity α_{f8} shown in Eq. (4.25). However, the threshold for the existence of DKSs is not $\alpha_{f8} = 0$. When $\alpha' = -\alpha$, the figure-8 cavity is still a

dissipative cavity with $\alpha_{f8} = 0.065\alpha$, while solitons cannot survive in such coupled microcavities as shown in Fig. 4.14(b). The inconsistency between the figure-8 cavity loss and the threshold for DKSs is because the results in Section 4.4 are based on the assumption of cw states inside the microcavities. When the intracavity fields are pulses, the results are not applicable.

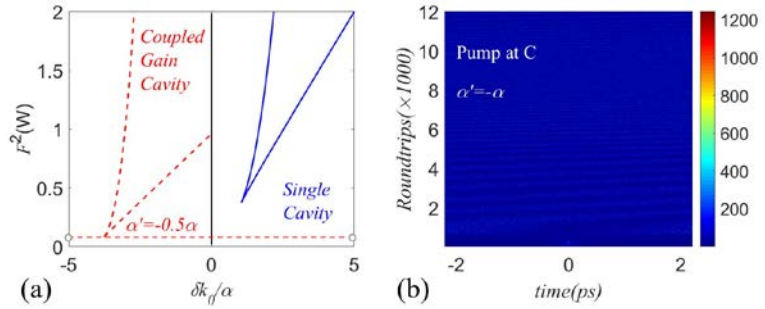

Fig. 4.14 (a) Bistability region of coupled microcavities with $\alpha' = -0.5\alpha$ (red dashed line) and a single microcavity (blue solid line). (b) An initial Gaussian pulse evolution in coupled microcavities with pumping condition at the point C with $\alpha' = -\alpha$.

4.7 Summary

In this Chapter, we demonstrated soliton frequency comb generation in coupled nonlinear microcavities. We theoretically analyze the bistable steady state condition in coupled microcavities by using a set of modified coupled Ikeda map and numerically determine the bistability region. Compared with a single microcavity, we find that the location of the soliton region depends on the coupling coefficient between the two cavities. The soliton region blue-shifts when the coupling coefficient increases and can locate within the blue-detuned region relative to the cold cavity resonance. Therefore, one can tune the soliton region to cover the pump laser wavelength to achieve frequency comb generation, instead of tuning the pump laser wavelength into the soliton region.

We find that the coupling of the auxiliary cavity introduces new optical paths in the coupled microcavity system. We attribute the blue-detuned bistability region to a compound figure-8 optical path. The pump laser frequency is in fact red-detuned with respect to the figure-8 cavity. We numerically demonstrate soliton frequency comb generation in coupled nonlinear microcavities by tuning coupling coefficient between the two microcavities. To overcome the difficulties in practice to fabricate two identical microcavities, we proposed a Sagnac loop like structure to achieve CW-CCW coupling in a single microcavity. The Sagnac loop like single cavity also supports soliton comb generation by tuning the coupling coefficient between the CW and CCW modes. The effect of XPM is included in the simulation.

To overcome the stringent high Q requirement for soliton generation in a single microcavity, we couple a microcavity with gain to a low Q microcavity. We found that there is a threshold of the auxiliary cavity gain for soliton comb generation. When the gain of the auxiliary cavity is below the threshold, the loss of the main cavity can be compensated by the auxiliary cavity and makes it possible to generate soliton frequency combs in low Q microcavities. When the gain of the auxiliary cavity is beyond the threshold, no soliton is generated because the overall cavity is not dissipative. DKS is not a stable solution in such cavities.

5 Summary and future works

In this thesis, we present theoretical analysis of MI and soliton microcomb generation in a coupled nonlinear microcavity system. By coupling an auxiliary cavity, new MI and bistability regions are created at the blue-detuned side with respect to the main cavity resonances where there are only red-detuned MI and bistability regions in a single microcavity. Based on the theoretical results, we proposed a new soliton microcomb excitation scheme by tuning the coupling in coupled microcavities. A method for soliton microcomb generation in low Q microcavities by coupling to an auxiliary cavity with gain is also demonstrated.

For MI generation, we find a new MI generation region with blue-detuned pumping regime when the main nonlinear microcavity is coupled to an auxiliary cavity with negligible Kerr nonlinearity. The conditions for the emergence of the blue-detuned MI region are numerically determined by stability analysis of a set of modified CMEs. We determine how the size and location of this new MI region depend on three main parameters: the coupling coefficient between the two cavities, the loss of the auxiliary cavity, and the detuning between the coupling modes of the two cavities. We attribute the emergence of the new MI region to the additional figure-8 optical path induced by the auxiliary cavity. The blue-detuned MI region with respect to the main cavity is in fact red-detuned to the figure-8 cavity. By assuming the auxiliary cavity is in steady state, the blue-detuned MI region can be determined analytically. Numerical simulations are carried out to verify our theoretical analysis.

The soliton microcomb generation depends on the bistability condition. The variation of the bistability region is numerically demonstrated based on the stability analysis of a set of modified Ikeda map. We find that the location of the bistability region can be tuned by changing the coupling coefficient between the two coupled identical microcavities. The blue-detuned bistability region is due to the additional figure-8 optical path induced by the coupling of an auxiliary cavity. The blue-detuned bistability region with respect to the main cavity resonances is red-detuned to the figure-8 cavity resonances. We determine the effective detuning and loss of the figure-8 cavity at steady state. The change in the bistability region is caused by the change in the effective detuning of the figure-8 cavity. We propose a novel soliton microcomb generation scheme based on tuning the coupling coefficient. The excitation of soliton microcomb by tuning coupling is demonstrated with numerical simulations. For ease of fabrication, we design a Sagnac-like microcavity which couples the CW and CCW propagating modes and numerically demonstrate soliton generation by tuning the coupling in this cavity. To achieve soliton microcomb generation in low Q microcavities, we use an auxiliary cavity with gain to compensate the loss in the main cavity. The gain of the auxiliary cavity should be lower than a threshold to maintain the overall cavity dissipative.

Our findings in this thesis add to the understanding of microcomb generation in coupled nonlinear microcavities and make possible the realization of chip-scale integrated microcomb sources.

In this thesis, we focus on the investigation of MI region at the blue-detuned side with respect to the main cavity resonances. The coupling of the auxiliary cavity also affects the MI region at the red-detuned side.

As discussed in Section 3.2.4, when the initially blue-detuned MI region shifts to the red-detuned side, it can merge with the initially red-detuned MI region. Recall that the blue-detuned MI region and the red-detuned MI region originate from the figure-8 cavity optical path and the main cavity optical path, respectively. The merging means that we can use a single cw pump to excite MI generation with the optical fields in the main cavity optical path and the figure-8 cavity optical path. As shown in Fig. 5.1, a cw pump with parameters at point A can excite MI generations in both optical paths. In this case, there are a number of questions worth exploring. Firstly, are the two MI fields are generated in separate optical path coherent? Secondly, how is the intensity of the MI field generated at this point compared to that of a single microcavity with the same parameters? Thirdly, since a single pump cw laser is used to excite two MI generation, will this regime increase the pump to MI conversion efficiency? These questions are to be investigated in our future work.

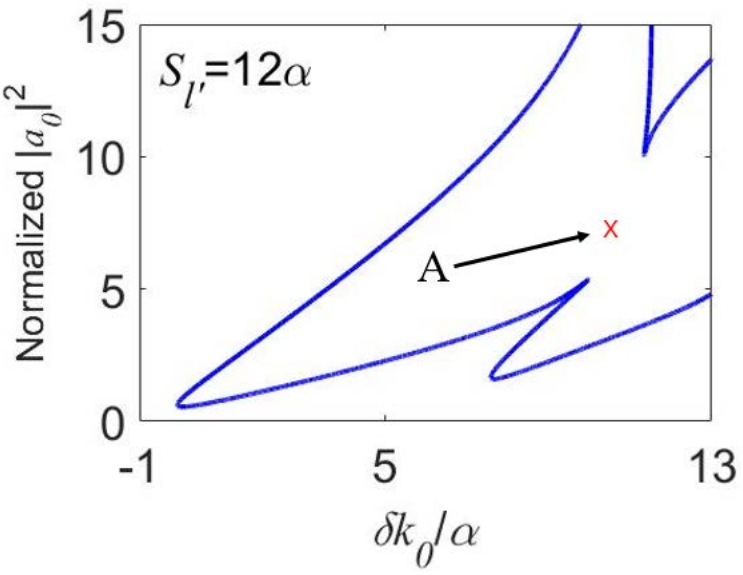

Fig. 5.1 The merging of the blue-detuned MI region and red-detuned MI region with the coupled modes detuning $S_{l'} = 12\alpha$.

In this thesis, for the ease of numerical simulations, we assume the auxiliary cavity size is identical to the main cavity. The size of the auxiliary cavity determines the FSR of the figure-8 cavity optical path induced by the coupling. As shown in Fig. 5.2, if the length of the auxiliary cavity L' increases from L to $3L$, where L is the cavity length of the main cavity, the FSR of the figure-8 optical path will be halved compared to that in the case $L' = L$. If L' further increased to $7L$, the spacing between adjacent resonances of the figure-8 optical path will be a quarter of its value at $L' = L$. If the MI detuning range of the blue-detuned MI region is not affected by the auxiliary cavity length, with a large enough auxiliary cavity, it is possible to achieve the situation where the FSR of the figure-8 optical path is narrower than the MI detuning range. It will be unnecessary to carefully choose the pump laser frequency for MI generation in microcavities. The effect of auxiliary cavity length on the blue-detuned MI region will also be studied in our future work.

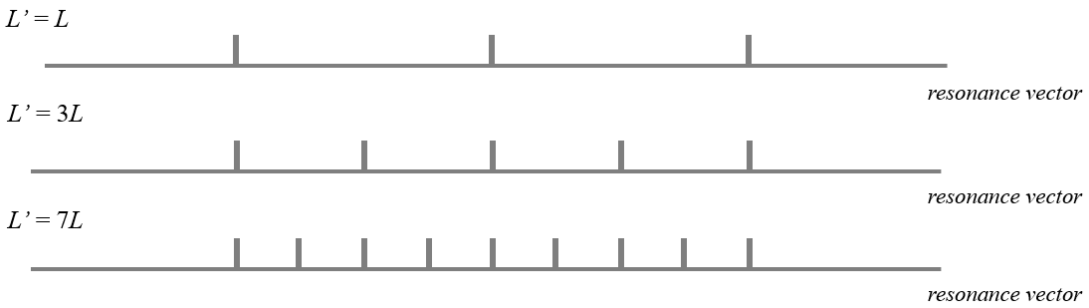

Fig. 5.2. FSR of figure-8 optical path in two coupled microcavities with auxiliary cavity length L' = L, 3L, and 7L, where L is the cavity length of the main cavity.

Appendix A: Acronyms

OFC	optical frequency comb
MLL	mode locked laser
TOF	time of flight
LOS	linear optical sampling
cw	continuous wave
MI	modulation instability
FSR	free spectral range
FWM	four wave mixing
DKS	dissipative Kerr soliton
CMEs	coupled mode equations
GNLSE	Generalized Nonlinear Schrödinger Equation
CW	clockwise
CCW	counter-clockwise
LB	left detuning boundary
RB	right detuning boundary
SSC	steady state calculation method
ACR	auxiliary cavity resonance
MCR	main cavity resonance
XPM	cross phase modulation

Appendix B: A list of symbols used in this thesis

f_r ---- repetition rate of OFCs

v_N ---- exact frequency of the N-th mode

f_0 ---- common offset frequency

T_R ---- roundtrip time of a laser cavity or a microcavity

L ---- cavity length

v_g ---- group velocity

ω_m ---- angular frequency of the m-th mode

n ---- cavity refractive index

c ---- speed of light

m ---- absolute mode number

k_m ---- wave vector of the m-th mode

μ ---- relative mode number

D_1 ---- $2\pi/D_1$ denotes the cavity length

D_2 ---- second order dispersion

D_3 ---- third order dispersion

Q ---- quality factor

U_{cav} ---- energy stored in the cavity

U_{diss} ---- energy dissipated per oscillation cycle

α ---- cavity loss rate

$E(t, z)$ ---- complex optical field

θ_c ---- power transmission coefficient

A_μ ---- amplitude of the μ-th mode

a_μ ---- amplitude of the μ-th mode in the frame of relative wave vector

z ---- evolution variable

θ ---- power coupling coefficient

F ---- pump laser amplitude

k_{pump} ---- wave vector of the pump laser

$\delta_{\mu 0}$ ---- the Kronecker delta function

t ---- ordinary time

δk_0 ---- wave vector detuning from the cavity resonance closest to the pump frequency

β_2 ---- group velocity dispersion

γ ---- Kerr nonlinear coefficient

δa_μ ---- small fluctuation perturbating mode a_μ

λ ---- eigenvalue of a secular equation

G_{MI} ---- MI gain

ϕ ---- phase accumulation in one roundtrip

L_{eff} ---- effective nonlinear length

$L_{eff,A}$---- effective nonlinear length of the auxiliary cavity

$L_{eff,M}$ ---- effective nonlinear length of the main cavity

Δk_0 ---- wave vector detuning between the pump modes of coupled cavities

$S_{l'}$ ---- detuning of the l'-th coupling modes in the auxiliary cavity

Appendix C: Super-modes in a coupled microcavity system

In a coupled microcavity system, the total field in both cavities can be expressed as a super-position of the modes of the compound structure. These modes are called super-modes and we present a derivation of the super-modes in two linear microcavities with cw fields in the cavities.

The fields in the main and auxiliary cavities obey the CMEs as

$$\frac{\partial a_0}{\partial z} = -i\delta k_0 a_0 - \frac{\alpha L}{2} a_0 + i\sqrt{\theta_c}\, a_0', \tag{C-1}$$

$$\frac{\partial a_0'}{\partial z} = -i\delta k_0' a_0' - \frac{\alpha' L'}{2} a_0' + i\sqrt{\theta_c}\, a_0, \tag{C-2}$$

where a_0 and a_0' are field amplitudes of the main and auxiliary cavities, respectively. The other parameters are defined in Appendix B. Eqs. (C-1) and (C-2) can be rewritten as

$$\begin{bmatrix} \frac{\partial a_0}{\partial z} \\ \frac{\partial a_0'}{\partial z} \end{bmatrix} = \begin{bmatrix} -i\delta k_0 - \frac{\alpha L}{2} & i\sqrt{\theta_c} \\ i\sqrt{\theta_c} & -i\delta k_0' - \frac{\alpha' L'}{2} \end{bmatrix} \begin{bmatrix} a_0 \\ a_0' \end{bmatrix}. \tag{C-3}$$

The eigenvalues of Eq. (C-3) $\lambda_\pm$ can be determined by solving

$$\begin{bmatrix} -i\delta k_0 - \frac{\alpha L}{2} - \lambda & i\sqrt{\theta_c} \\ i\sqrt{\theta_c} & -i\delta k_0' - \frac{\alpha' L'}{2} - \lambda \end{bmatrix} = 0, \tag{C-4}$$

where

$$\lambda_{\pm} = \frac{\left(-i\delta k_0' - \frac{\alpha' L'}{2} - i\delta k_0 - \frac{\alpha L}{2}\right) \pm \sqrt{\left(-i\delta k_0' - \frac{\alpha' L'}{2} + i\delta k_0 + \frac{\alpha L}{2}\right)^2 - 4\theta_c}}{2}. \quad \text{(C-5)}$$

Thus, the super-modes in the compound cavity are described by

$$\frac{\partial b_0}{\partial z} = \lambda_+ b_0, \quad \text{(C-6)}$$

$$\frac{\partial b_0'}{\partial z} = \lambda_- b_0', \quad \text{(C-7)}$$

where b_0 and b_0' are field amplitudes of the super-modes in the compound cavity. The imaginary parts of $\lambda_{\pm}$ are the wave vector detuning of the super-modes, and the real parts are the loss rates.

Appendix D: Definition of dispersion coefficients in optical fibers

Dispersion describes the dependence of refractive index $n(\omega)$ on the optical angular frequency ω. Dispersion is important for pulse propagation in optical fibers because different spectral components of the pulse travel with different phase velocity given by $c/n(\omega)$, where c is the speed of light in vacuum. The dispersion coefficients in optical fibers are defined by expanding the mode-propagation constant $\beta(\omega)$ in a Taylor series about the central frequency of pulse spectrum ω_0 [93]:

$$\beta(\omega) = n(\omega)\frac{\omega}{c} = \beta_0 + \beta_1(\omega-\omega_0) + \frac{1}{2}\beta_2(\omega-\omega_0)^2 + \cdots, \tag{D-1}$$

where

$$\beta_m = \left(d^m\beta / d\omega^m\right)_{\omega=\omega_0} \qquad (m = 0,1,2,...). \tag{D-2}$$

The parameters β_1 and β_2 are related to the refractive index $n(\omega)$. β_1 relates with the group velocity v_g through

$$\beta_1 = \frac{1}{v_g} = \frac{n_g}{c} = \frac{1}{c}\left(n + \omega\frac{dn}{d\omega}\right), \tag{D-3}$$

where n_g is the group index. β_2 is the group velocity dispersion coefficient. The relationship between β_2 and the refractive index $n(\omega)$ is given by

$$\beta_2 = \frac{1}{c}\left(2\frac{dn}{d\omega} + \omega\frac{d^2n}{d\omega^2}\right). \tag{D-4}$$

In optical communication community, another definition of the group velocity dispersion coefficient is often used, it is $D = d\beta_1/d\lambda$ where λ is the wavelength. D relates to β_2 and $n(\lambda)$ as

$$D = \frac{d\beta_1}{d\lambda} = -\frac{2\pi c}{\lambda^2}\beta_2 = -\frac{\lambda}{c}\frac{d^2 n}{d\lambda^2}. \tag{D-5}$$

In microcavities, we use the expansion of resonance wave vector to define the dispersion coefficients as shown in Eq. (1.3). An equivalent expression of Eq. (1.3) with resonance frequencies is

$$\omega_\mu = \omega_0 + D_1 c\mu + \frac{1}{2}D_2 c\mu^2 + \frac{1}{6}D_3 c\mu^3 ..., \tag{D-6}$$

where μ is the mode number, D_1 is the mode wave vector spacing, D_2 and D_3 are the second and third order dispersion coefficients as defined in Eq. (1.6). The frequency spacing of two neighboring resonance modes can be expressed as

$$\omega_\mu - \omega_{\mu-1} = \frac{2\pi c}{n(\omega_\mu)L}, \tag{D-7}$$

where L is the cavity length. If we assume the dispersion coefficients beyond second order are small in Eq. (D-6), we can get

$$n(\omega_\mu) = \frac{2\pi}{L\left[D_1 + D_2(2l-1)/2\right]}, \tag{D-8}$$

$$\frac{d\mu}{d\omega_\mu} = \frac{1}{c\sqrt{D_1^2 + 2D_2\left(D_1\mu + D_2\mu^2/2\right)}}. \tag{D-9}$$

From Eqs. (D-8) and (D-9) we have

$$\frac{dn(\omega_\mu)}{d\omega_\mu} = \frac{dn(\omega_\mu)}{d\mu}\frac{d\mu}{d\omega_\mu} = -\frac{2\pi D_2}{Lc\left[D_1 + D_2(2\mu-1)/2\right]^2\sqrt{D_1^2 + 2D_2\left(D_1\mu + D_2\mu^2/2\right)}}, \tag{D-10}$$

$$\frac{d^2 n(\omega_\mu)}{d\omega_\mu{}^2} = \frac{d\left[dn(\omega_\mu)/d\omega_\mu\right]}{dl}\frac{dl}{d\omega_l} = \frac{2\pi D_2{}^2\left\{2\left[D_1^2 + 2D_2\left(D_1\mu + D_2\mu^2/2\right)\right] + (D_1 + D_2\mu)\left[D_1 + D_2(2\mu-1)/2\right]\right\}}{Lc^2\left[D_1 + D_2(2\mu-1)/2\right]^3\left[D_1^2 + 2D_2\left(D_1\mu + D_2\mu^2/2\right)\right]^2}. \tag{D-11}$$

Substitute Eqs. (D-10) and (D-11) into Eq. (D-4), we have

$$\beta_2 = \frac{2\pi\omega_\mu D_2{}^2 \left\{2\left[D_1^2 + 2D_2\left(D_1\mu + D_2\mu^2/2\right)\right] + (D_1 + D_2\mu)\left[D_1 + D_2(2\mu - 1)/2\right]\right\}}{Lc^3\left[D_1 + D_2\left(2\mu - 1\right)/2\right]^3\left[D_1^2 + 2D_2\left(D_1\mu + D_2\mu^2/2\right)\right]^2}$$
$$- \frac{4\pi D_2}{Lc^2\left[D_1 + D_2\left(2\mu - 1\right)/2\right]^2\left[D_1^2 + 2D_2\left(D_1\mu + D_2\mu^2/2\right)\right]^{1/2}}. \quad \text{(D-12)}$$

Bibliography

[1] Fortier, T., Baumann, E., “20 years of developments in optical frequency comb technology and applications,” *Commun Phys* **2**, 153 (2019).

[2] H. Schnatz, B. Lipphardt, J. Helmcke, F. Riehle, and G. Zinner, “First Phase-Coherent Frequency Measurement of Visible Radiation,” *Phys. Rev. Lett.* **76**, 18 (1996).

[3] Telle, H., Steinmeyer, G., Dunlop, A. et al., “Carrier-envelope offset phase control: A novel concept for absolute optical frequency measurement and ultrashort pulse generation,” *Appl Phys B* **69**, 327–332 (1999).

[4] Mengjie Yu, Boris Desiatov, Yoshitomo Okawachi, Alexander L. Gaeta, and Marko Lončar, "Coherent two-octave-spanning supercontinuum generation in lithium-niobate waveguides," *Opt. Lett.* **44**, 1222-1225 (2019).

[5] Hollberg L, Diddams S, Bartels A, et al., “The measurement of optical frequencies,” *Metrologia* **42**, S105 (2005).

[6] Coddington, I., Swann, W., Nenadovic, L. et al., “Rapid and precise absolute distance measurements at long range,” *Nature Photon* **3**, 351–356 (2009).

[7] Dorrer C, Kilper D C, Stuart H R, et al., “Linear optical sampling,” *IEEE Photonics Technology Letters*, **15**, 1746-1748 (2003).

[8] Keller, U, “Recent developments in compact ultrafast lasers,” *Nature* **424**, 831–838 (2003).

[9] Baltuška, A., Udem, T., Uiberacker, M. et al, “Attosecond control of electronic processes by intense light fields,” *Nature* **421**, 611–615 (2003).

[10] Diddams, S., Hollberg, L. & Mbele, V., “Molecular fingerprinting with the resolved modes of a femtosecond laser frequency comb,” *Nature* **445**, 627–630 (2007).

[11] Prasad, K. and Alden, C., “Methane leak detection and sizing over long distances using dual frequency comb laser spectroscopy and a bootstrap inversion technique,” *Atmospheric Measurement Techniques* **11**, (2018).

[12] Moss, D., Morandotti, R., Gaeta, A. et al., “New CMOS-compatible platforms based on silicon nitride and Hydex for nonlinear optics,” *Nature Photon* **7**, 597–607 (2013).

[13] Lin J, Yao N, Hao Z, et al., “Broadband quasi-phase-matched harmonic generation in an on-chip monocrystalline lithium niobate microdisk resonator,” *Physical review letters*, **122**, 173903 (2019).

[14] Herr, T., Brasch, V., Jost, J. et al., “Temporal solitons in optical microresonators,” *Nature Photon* **8**, 145–152 (2014).

[15] Del’Haye, P., Schliesser, A., Arcizet, O. et al., “Optical frequency comb generation from a monolithic microresonator,” *Nature* **450**, 1214–1217 (2007).

[16] Xue, X., Xuan, Y., Liu, Y. et al., “Mode-locked dark pulse Kerr combs in normal-dispersion microresonators,” *Nature Photon* **9**, 594–600 (2015).

[17] Yang He, Qi-Fan Yang, Jingwei Ling, Rui Luo, Hanxiao Liang, Mingxiao Li, Boqiang Shen, Heming Wang, Kerry Vahala, and Qiang Lin, "Self-starting bi-chromatic LiNbO3 soliton microcomb," *Optica* **6**, 1138-1144 (2019).

[18] Haizhong Weng, Jia Liu, Adnan Ali Afridi, Jing Li, Jiangnan Dai, Xiang Ma, Yi Zhang, Qiaoyin Lu, John F. Donegan, and Weihua Guo, "Directly accessing octave-spanning dissipative Kerr soliton frequency combs in an AlN microresonator," *Photon. Res.* **9**, 1351-1357 (2021).

[19] Vladimir S. Ilchenko, Anatoliy A. Savchenkov, Andrey B. Matsko, and Lute Maleki, "Dispersion compensation in whispering-gallery modes," *J. Opt. Soc. Am. A* **20**, 157-162 (2003).

[20] Kerry J. Vahala, "Optical microcavities," *Nature* **424**, 839–846 (2003).

[21] Chembo Y K, Yu N., "Modal expansion approach to optical-frequency-comb generation with monolithic whispering-gallery-mode resonators," *Physical Review A* **82**, 033801 (2010).

[22] Godey C, Balakireva I V, Coillet A, et al., "Stability analysis of the spatiotemporal Lugiato-Lefever model for Kerr optical frequency combs in the anomalous and normal dispersion regimes," *Physical Review A* **89**, 063814 (2014).

[23] Kippenberg T J, Gaeta A L, Lipson M, et al., "Dissipative Kerr solitons in optical microresonators," *Science* **361**, eaan8083 (2018).

[24] Chao Xiang, Warren Jin, John E. Bowers, “Silicon nitride passive and active photonic integrated circuits: trends .and prospects,” *Photon. Res.* **10**, A82-A95 (2022).

[25] Bartels A, Heinecke D, Diddams S A., “10-GHz self-referenced optical frequency comb,” *Science* **326**, 681-681 (2009).

[26] Spencer, D.T., Drake, T., Briles, T.C. et al., “An optical-frequency synthesizer using integrated photonics,” *Nature* **557**, 81–85 (2018).

[27] Marin-Palomo, P., Kemal, J., Karpov, M. et al., “Microresonator-based solitons for massively parallel coherent optical communications,” *Nature* **546**, 274–279 (2017).

[28] Kuse N, Fermann M E., “Frequency-modulated comb LIDAR,” *Apl Photonics* **4**, 106105 (2019).

[29] Obrzud, E., Rainer, M., Harutyunyan, A. et al., “A microphotonic astrocomb,” *Nature Photon* **13**, 31–35 (2019).

[30] Suh, MG., Yi, X., Lai, YH. et al., “Searching for exoplanets using a microresonator astrocomb,” *Nature Photon* **13**, 25–30 (2019).

[31] Suh M G, Yang Q F, Yang K Y, et al., “Microresonator soliton dual-comb spectroscopy,” *Science* **354**, 600-603 (2016).

[32] Trocha P, Karpov M, Ganin D, et al., “Ultrafast optical ranging using microresonator soliton frequency combs,” *Science* **359**, 887-891(2018).

[33] Suh M G, Vahala K J., “Soliton microcomb range measurement,” *Science* **359**, 884-887 (2018).

[34] Scott B. Papp, Katja Beha, Pascal Del'Haye, Franklyn Quinlan, Hansuek Lee, Kerry J. Vahala, and Scott A. Diddams, "Microresonator frequency comb optical clock," *Optica* **1**, 10-14 (2014).

[35] Brasch, V., Lucas, E., Jost, J. et al., "Self-referenced photonic chip soliton Kerr frequency comb," *Light Sci Appl* **6**, e16202 (2017).

[36] Zheng Gong, Xianwen Liu, Yuntao Xu, Mingrui Xu, Joshua B. Surya, Juanjuan Lu, Alexander Bruch, Changling Zou, and Hong X. Tang, "Soliton microcomb generation at 2 μm in z-cut lithium niobate microring resonators," *Opt. Lett.* **44**, 3182-3185 (2019).

[37] Karpov M, Guo H, Kordts A, et al., "Raman self-frequency shift of dissipative Kerr solitons in an optical microresonator," *Physical review letters* **116**, 103902 (2016).

[38] Brasch V, Geiselmann M, Herr T, et al, "Photonic chip–based optical frequency comb using soliton Cherenkov radiation," *Science* **351**, 357-360 (2016).

[39] https://www.santec.com/en/products/instruments/tunablelaser/TSL-770/

[40] https://www.toptica.com/products/tunable-diode-lasers/ecdl-dfb-lasers/dl-pro/

[41] Stone J R, Briles T C, Drake T E, et al., "Thermal and nonlinear dissipative-soliton dynamics in Kerr-microresonator frequency combs," *Physical review letters* **121**, 063902 (2018).

[42] Jian Wang, Dijun Chen, Haiwen Cai, Fang Wei, and Ronghui Qu, "Fast optical frequency sweeping using voltage controlled oscillator driven single sideband modulation combined with injection locking," *Opt. Express* **23**, 7038-7043 (2015).

[43] Stern, B., Ji, X., Okawachi, Y. et al., “Battery-operated integrated frequency comb generator,” *Nature* **562**, 401–405 (2018).

[44] Lu Z, Wang W, Zhang W, et al., “Deterministic generation and switching of dissipative Kerr soliton in a thermally controlled micro-resonator,” *Aip Advances* **9**, 025314 (2019).

[45] Steven A. Miller, Yoshitomo Okawachi, Sven Ramalow, et al., “Tunable frequency combs based on dual microring resonators,” *Opt. Express* **23**, 21527-21540 (2015).

[46] Gaeta, A.L., Lipson, M. & Kippenberg, T.J., “Photonic-chip-based frequency combs,” *Nature Photon* **13**, 158–169 (2019).

[47] Austin G. Griffith, Ryan K. W. Lau, Jaime Cardenas, et al., “Silicon-chip mid-infrared frequency comb generation,” *Nat Commun* **6**, 6299 (2015).

[48] Xiaowei Guan, Hao Hu, Leif K. Oxenløwe, and Lars H. Frandsen, “Compact titanium dioxide waveguides with high nonlinearity at telecommunication wavelengths,” *Opt. Express* **26**, 1055-1063 (2018).

[49] Wei C. Jiang, Kangmei Li, Xin Gai, Daniel A. Nolan, and Paulo Dainese, “Ultra-low-power four-wave mixing wavelength conversion in high-Q chalcogenide microring resonators,” *Opt. Lett.* **46**, 2912-2915 (2021).

[50] Bin Zhang, Pingyang Zeng, Zelin Yang, Di Xia, Jiaxin Zhao, Yaodong Sun, Yufei Huang, Jingcui Song, Jingshun Pan, Huanjie Cheng, Dukyong Choi, and Zhaohui Li, “On-chip chalcogenide microresonators with low-threshold parametric oscillation,” *Photon. Res.* **9**, 1272-1279 (2021).

[51] Wu R, Wang M, Xu J, et al., “Long low-loss-litium niobate on insulator waveguides with sub-nanometer surface roughness,” *Nanomaterials* **8**, 910 (2018).

[52] Martin H. P. Pfeiffer, Junqiu Liu, Arslan S. Raja, Tiago Morais, Bahareh Ghadiani, and Tobias J. Kippenberg, “Ultra-smooth silicon nitride waveguides based on the Damascene reflow process: fabrication and loss origins,” *Optica* **5**, 884-892 (2018).

[53] Mian Zhang, Cheng Wang, Rebecca Cheng, Amirhassan Shams-Ansari, and Marko Lončar, “Monolithic ultra-high-Q lithium niobate microring resonator,” *Optica* **4**, 1536-1537 (2017).

[54] Chang, L., Jiang, X., Hua, S. et al., “Parity–time symmetry and variable optical isolation in active–passive-coupled microresonators,” *Nature Photon* **8**, 524–529 (2014).

[55] Peng, B., Özdemir, Ş., Lei, F. et al., “Parity–time-symmetric whispering-gallery microcavities,” *Nature Phys* **10**, 394–398 (2014).

[56] Özdemir, Ş.K., Rotter, S., Nori, F. et al., “Parity–time symmetry and exceptional points in photonics,” *Nat. Mater.* **18**, 783–798 (2019).

[57] Lin Chang, Songtao Liu and John E. Bowers, “Integrated optical frequency comb technologies,” *Nature Photon* **16**, 95–108 (2022).

[58] Wang C, Sweeney W R, Stone A D, et al., “Coherent perfect absorption at an exceptional point,” *Science* **373**, 1261-1265 (2021).

[59] Ying Zhang, Qiang Liu, Chenyang Mei, Desheng Zeng, Qingzhong Huang, and Xinliang Zhang, “Proposal and demonstration of a controllable Q factor in directly

coupled microring resonators for optical buffering applications," *Photon. Res.* **9**, 2006-2015 (2021).

[60] Lee, J., Kim, Y.S., "Reliability and stability analysis and crack estimation of semiconductor gas sensors heater," *In Proceedings of the 2021 International Conference on Electronics, Information and Communication (Iceic)*, Jeju, Korea, 31 January–3 February 2021.

[61] Colle, R., Zimmerman, B.E., "A dual-compensated cryogenic microcalorimeter for radioactivity standardizations," *Appl. Radiat. Isot.* **56**, 223–230 (2002).

[62] Wang, W.C., Wu, Y.H., Chang, Z.H., et al., "Self-powered intelligent water meter for electrostatic scale preventing, rust protection, and flow sensor in a solar heater system," *Acs Appl. Mater. Inter.* **11**, 6396–6403 (2019).

[63] Romer, M., Bergers, J., Gabriel, F., et al., "Temperature control for automated tape laying with infrared heaters based on reinforcement learning," *Machines* **10**, 164 (2022).

[64] Fu, X., Yang, H., Li, Z., et al., "Cation-induced assembly of conductive MXene fibers for wearable heater, wireless communication, and stem cell differentiation," *ACS Biomater. Sci. Eng.*, (2021).

[65] Solzbacher, F., Imawan, C., Steffes, H., et al., "A new SiC/HfB2 based low power gas sensor," *Sensor Actuat. B-Chem.* **77**, 111–115 (2001).

[66] M. E. Castagna, R. Modica, S. Cascino, et al. "A high stability and uniformity W micro hot plate," *Sensors and Actuators A* **279**, 617–623 (2018).

[67] Dezhao Li, Tangtao Ruan, Chuangang Chen, et al., “Design and Thermal Analysis of Flexible Microheaters,” *Micromachines* **13**, 1037 (2022).

[68] Xue X, Xuan Y, Wang P H, et al., “Normal‐dispersion microcombs enabled by controllable mode interactions,” *Laser & Photonics Reviews* **9**, L23-L28 (2015).

[69] Jae K. Jang, Yoshitomo Okawachi, Mengjie Yu, Kevin Luke, Xingchen Ji, Michal Lipson, and Alexander L. Gaeta, “Dynamics of mode-coupling-induced microresonator frequency combs in normal dispersion,” *Opt. Express* **24**, 28794-28803 (2016).

[70] Helgason, Ó.B., Arteaga-Sierra, F.R., Ye, Z. et al., “Dissipative solitons in photonic molecules,” *Nat. Photonics* **15**, 305–310 (2021).

[71] Fujii S, Okabe Y, Suzuki R, et al., “Analysis of mode coupling assisted Kerr comb generation in normal dispersion system,” *IEEE Photonics Journal* **10**, 1-11 (2018).

[72] Steven A. Miller, Yoshitomo Okawachi, Sven Ramelow, Kevin Luke, Avik Dutt, Alessandro Farsi, Alexander L. Gaeta, and Michal Lipson, “Tunable frequency combs based on dual microring resonators,” *Opt. Express* **23**, 21527-21540 (2015).

[73] Bok Young Kim, Yoshitomo Okawachi, Jae K. Jang, Mengjie Yu, Xingchen Ji, Yun Zhao, Chaitanya Joshi, Michal Lipson, and Alexander L. Gaeta, “Turn-key, high-efficiency Kerr comb source,” *Opt. Lett.* **44**, 4475-4478 (2019).

[74] Xue, X., Zheng, X. & Zhou, B., “Super-efficient temporal solitons in mutually coupled optical cavities,” *Nat. Photonics* **13**, 616–622 (2019).

[75] G. P. Agrawal, “Nonlinear fiber optics,” *Academic Press*, Fifth edition, pp. 129-139 (2013).

[76] A. A. Savchenkov, A. B. Matsko, W. Liang, et al., “Kerr frequency comb generation in overmoded resonators,” *Opt. Express* **20**, 27290-27298 (2012).

[77] Kippenberg T J, Spillane S M, Vahala K J., “Kerr-nonlinearity optical parametric oscillation in an ultrahigh-Q toroid microcavity,” *Physical review letters* **93**, 083904 (2004).

[78] Herr, T., Hartinger, K., Riemensberger, J. et al., “Universal formation dynamics and noise of Kerr-frequency combs in microresonators,” *Nature Photon* **6**, 480–487 (2012).

[79] Hansson T, Modotto D, Wabnitz S., “On the numerical simulation of Kerr frequency combs using coupled mode equations,” *Optics Communications* **312**, 134-136 (2014).

[80] Ikeda K., “Multiple-valued stationary state and its instability of the transmitted light by a ring cavity system,” *Optics communications* **30**, 257-261(1979).

[81] Napoléon Gutierrez, Arnaud Fernandez, Olivier Llopis, Stéphane Calvez, and Stéphane Balac, “Numerical study on Kerr frequency comb generation in Si3N4 microresonators with frequency-dependent access coupler properties,” *J. Opt. Soc. Am. B* **36**, 2896-2906 (2019).

[82] G. P. Agrawal, “Nonlinear fiber optics,” *Academic Press*, Fifth edition, pp. 34-47 (2013).

[83] Tobias Hansson and Stefan Wabnitz, “Frequency comb generation beyond the Lugiato–Lefever equation: multi-stability and super cavity solitons,” *J. Opt. Soc. Am. B* **32**, 1259-1266 (2015).

[84] Haelterman M, Trillo S, Wabnitz S., “Dissipative modulation instability in a nonlinear dispersive ring cavity,” *Optics communications* **91**, 401-407 (1992).

[85] G. P. Agrawal, “Nonlinear fiber optics,” *Academic Press*, Fifth edition, pp. 88-90 (2013).

[86] Guo, H., Karpov, M., Lucas, E. et al., “Universal dynamics and deterministic switching of dissipative Kerr solitons in optical microresonators,” *Nature Phys* **13**, 94–102 (2017).

[87] Xu Yi, Qi-Fan Yang, Ki Youl Yang, and Kerry Vahala, “Active capture and stabilization of temporal solitons in microresonators,” *Opt. Lett.* **41**, 2037-2040 (2016).

[88] V. E. Lobanov, G. V. Lihachev, N. G. Pavlov, A. V. Cherenkov, T. J. Kippenberg, and M. L. Gorodetsky, “Harmonization of chaos into a soliton in Kerr frequency combs,” *Opt. Express* **24**, 27382-27394 (2016).

[89] Zhe Kang, Feng Li, Jinhui Yuan, K. Nakkeeran, J. Nathan Kutz, Qiang Wu, Chongxiu Yu, and P. K. A. Wai, “Deterministic generation of single soliton Kerr frequency comb in microresonators by a single shot pulsed trigger,” *Opt. Express* **26**, 18563-18577 (2018).

[90] Helgason Ó B, Girardi M, Ye Z, et al., “Power-efficient soliton microcombs,” *arXiv preprint*, arXiv:2202.09410 (2022).

[91] Englebert, N., De Lucia, F., Parra-Rivas, P. et al., “Parametrically driven Kerr cavity solitons,” *Nature Photon* **15**, 857–861 (2021).

[92] Yang Liu, Zheru Qiu, Xinru Ji, et al., “A photonic integrated circuit-based erbium-doped amplifier,” *Science* **376**, 1309-1313 (2022).

[93] G. P. Agrawal, “Nonlinear fiber optics,” *Academic Press*, Fifth edition, pp. 7-9 (2013).